AD-A116 774 AIR FORCE INST OF TECH WRIGHT-PATTERSON AFB OH F/G 13/9
LABYRINTH SEAL EFFECTS ON ROTOR BEARING SYSTEM STABILITY.(U)
MAY 82 A J PAVELKO

UNCLASSIFIED AFIT/NR/82-10T NL

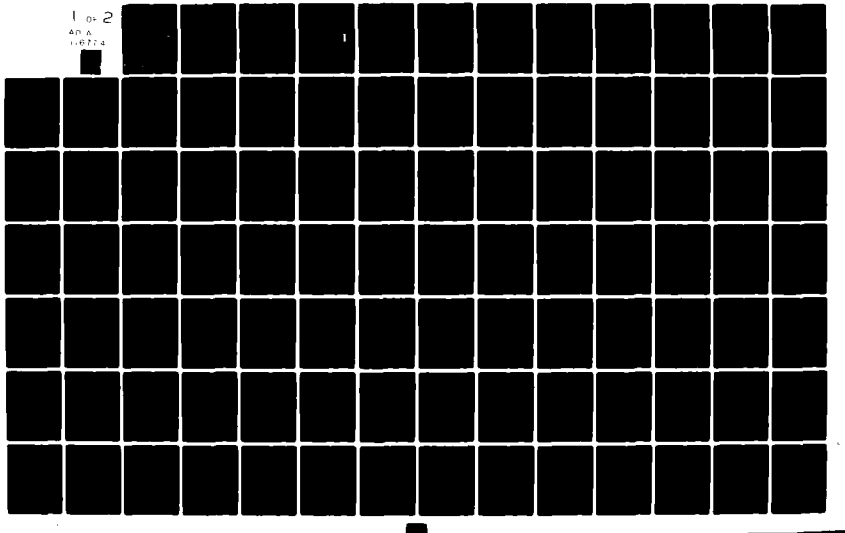

UNCLASS

SECURITY CLASSIFICATION OF THIS PAGE (When Data Entered)

REPORT DOCUMENTATION PAGE

READ INSTRUCTIONS BEFORE COMPLETING FORM

1. REPORT NUMBER: AFIT/NR/82-10T ✓
2. GOVT ACCESSION NO.: AD-A116774
3. RECIPIENT'S CATALOG NUMBER:

4. TITLE (and Subtitle): Labyrinth Seal Effects On Rotor Bearing System Stability
5. TYPE OF REPORT & PERIOD COVERED: THESIS/DISSERTATION
6. PERFORMING ORG. REPORT NUMBER:

7. AUTHOR(s): Anthony John Pavelko
8. CONTRACT OR GRANT NUMBER(s):

9. PERFORMING ORGANIZATION NAME AND ADDRESS: AFIT STUDENT AT: University of Texas at Austin
10. PROGRAM ELEMENT, PROJECT, TASK AREA & WORK UNIT NUMBERS:

11. CONTROLLING OFFICE NAME AND ADDRESS: AFIT/NR WPAFB OH 45433
12. REPORT DATE: May 1982
13. NUMBER OF PAGES: 170

14. MONITORING AGENCY NAME & ADDRESS (if different from Controlling Office):
15. SECURITY CLASS. (of this report): UNCLASS
15a. DECLASSIFICATION/DOWNGRADING SCHEDULE:

16. DISTRIBUTION STATEMENT (of this Report)

APPROVED FOR PUBLIC RELEASE; DISTRIBUTION UNLIMITED

17. DISTRIBUTION STATEMENT (of the abstract entered in Block 20, if different from Report)

18. SUPPLEMENTARY NOTES

APPROVED FOR PUBLIC RELEASE: IAW AFR 190-17

22 JUN 1982

LYNN E. WOLAVER
Dean for Research and Professional Development
AFIT, Wright-Patterson AFB OH

19. KEY WORDS (Continue on reverse side if necessary and identify by block number)

20. ABSTRACT (Continue on reverse side if necessary and identify by block number)

ATTACHED

82 07 07 059

DD FORM 1 JAN 73 1473 EDITION OF 1 NOV 65 IS OBSOLETE

UNCLASS

SECURITY CLASSIFICATION OF THIS PAGE (When Data Entered)

ABSTRACT

This thesis presents a stability analysis of rotor bearing system operation affected by a single labyrinth seal. Labyrinth seals, primarily intended for leakage control in turbines, have been observed to affect rotor stability in high pressure steam turbines. A small experimental rotor bearing system, existing in the Mechanical Engineering Department, and a compatible labyrinth seal are the subjects of this analysis. Linear analytical models of these rotor bearing and labyrinth seal systems, both isolated and coupled, are developed. Labyrinth seal geometry and pressure variations generate various affects on rotor bearing system stability. These affects can help develop labyrinth seal design criteria directed toward high pressure turbine stability enhancement.

AFIT/NR/82-10T

AFIT RESEARCH ASSESSMENT

The purpose of this questionnaire is to ascertain the value and/or contribution of research accomplished by students or faculty of the Air Force Institute of Technology (ATC). It would be greatly appreciated if you would complete the following questionnaire and return it to:

AFIT/NR
Wright-Patterson AFB OH 45433

RESEARCH TITLE: Labyrinth Seal Effects On Rotor Bearing System Stability

AUTHOR: Anthony John Pavelko

RESEARCH ASSESSMENT QUESTIONS:

1. Did this research contribute to a current Air Force project?

( ) a. YES ( ) b. NO

2. Do you believe this research topic is significant enough that it would have been researched (or contracted) by your organization or another agency if AFIT had not?

( ) a. YES ( ) b. NO

3. The benefits of AFIT research can often be expressed by the equivalent value that your agency achieved/received by virtue of AFIT performing the research. Can you estimate what this research would have cost if it had been accomplished under contract or if it had been done in-house in terms of manpower and/or dollars?

( ) a. MAN-YEARS _____ ( ) b. $_____

4. Often it is not possible to attach equivalent dollar values to research, although the results of the research may, in fact, be important. Whether or not you were able to establish an equivalent value for this research (3. above), what is your estimate of its significance?

( ) a. HIGHLY *SIGNIFICANT* ( ) b. SIGNIFICANT ( ) c. SLIGHTLY *SIGNIFICANT* ( ) d. OF NO *SIGNIFICANCE*

5. AFIT welcomes any further comments you may have on the above questions, or any additional details concerning the current application, future potential, or other value of this research. Please use the bottom part of this questionnaire for your statement(s).

NAME GRADE POSITION

ORGANIZATION LOCATION

STATEMENT(s):

FOLD DOWN ON OUTSIDE - SEAL WITH TAPE

AFIT/ NR
WRIGHT-PATTERSON AFB OH 45433

OFFICIAL BUSINESS
PENALTY FOR PRIVATE USE. $300

NO POSTAGE
NECESSARY
IF MAILED
IN THE
UNITED STATES

BUSINESS REPLY MAIL
FIRST CLASS PERMIT NO. 73236 WASHINGTON D.C.

POSTAGE WILL BE PAID BY ADDRESSEE

AFIT/ DAA
Wright-Patterson AFB OH 45433

FOLD IN

S 7-16

LABYRINTH SEAL EFFECTS ON ROTOR BEARING SYSTEM STABILITY

BY

ANTHONY JOHN PAVELKO

B.S. Mechanical Engineering

THESIS

Presented to the Faculty of the Graduate School of

The University of Texas at Austin

in Partial Fulfillment

of the Requirements

for the Degree of

MASTER OF SCIENCE IN ENGINEERING

THE UNIVERSITY OF TEXAS AT AUSTIN

May, 1982

LABYRINTH SEAL EFFECTS ON ROTOR BEARING SYSTEM STABILITY

APPROVED:

_____

_____

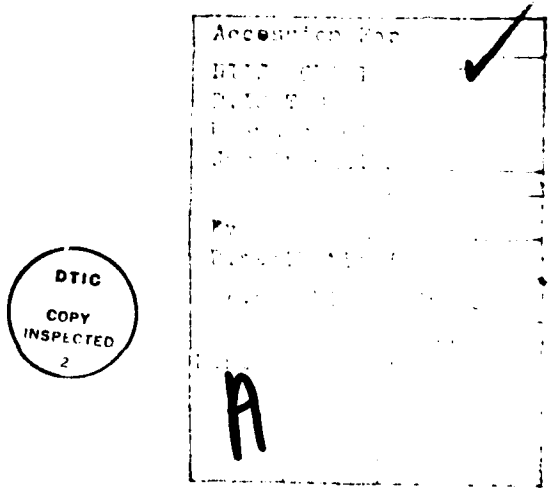

TABLE OF CONTENTS

Page

NOMENCLATURE

a Seal strip dimension (in)

A Area (in^2), Matrix descriptor, Variable, Seal position identifier

b Damping coefficient (lfb sec/in), Seal strip dimension (in)

B Damping coefficient (lbf sec/in), Variable, Seal position identifier

c Bearing to journal radial clearance (in)

C Seal position identifier, Variable

$\mathcal{F}$ Function

e Eccentricity (in), Natural logarithm base = 2.718

E Modulus of elasticity (lbf/in^2)

f Friction factor (dimensionless), Function

F Force (lbf)

h Minimum bearing to journal or seal base to disc radial clearance (in)

H Related to h

I Moment of inertia (lbf in sec^2)

k Stiffness factor (lbf/in), Specific heat ratio (dimensionless)

K Stiffness coefficient (lbf/in), Constant coefficient

ℓ Seal chamber length (in), Journal length (in)

L_{spt} Rotor-bearing system overall length (in)

m Mass (lbf sec^2/in)

M Mass coefficient (lbf sec^2/in), Mach number (dimensionless)

n Exponent in seal friction relations, Integer

O Fixed reference point

P Pressure (lbf/in^2), Momentum (lbf sec)

q Generalized coordinate

r Disc radius (in), Journal radius (in)

R Gas constant ($in^2/sec^{2o}R$)

Re Reynolds number (dimensionless)

s Seal circumferential distance independent variable (in)

t Time (sec)

T Temperature (^oR), Kinetic energy (lbf in)

u Seal circumferential fluid velocity (in/sec)

U Disc or journal surface velocity (in/sec)

v Eigenvector element (dimensionless), Velocity (in/sec)

V Potential energy (lbf in)

W Weight (lbf)

x Variable, Coordinate

y Variable, Coordinate

Y Related to y

z Variable, Coordinate

Greek

Δ Finite increment

γ Seal angular position variable (radians)

δ Variation

ε Eccentricity ratio (dimensionless) = e/c

θ Bearing angular position variable (radians)

λ Eigenvalue (dimensionless)

μ Dynamic viscosity (lbf sec/in^2)

$\tilde{\pi}$ Generalized force (lbf)

ν Kinematic viscosity = $\mu RT/P$ (in^2/sec)

π Constant ≈ 3.14

ρ Density (lbf sec/in^5)

τ Frictional shear stress (lbf/in^2)

ϕ Journal attitude angle (radian)

ω Angular velocity (rad/sec)

Subscripts

letters	Identification
numbers	Identification
A	Seal location, Axial
B	Seal location, Bearing
C	Seal location, Chamber
d	Disc
e	Eccentricity direction
f	Related to friction
h	High clearance area, Related to bearing or seal minimum clearance
i	Inside, Particular value
j	General value
J	Journal
L	Low clearance area, Left
n	Nominal value
o	Outside, Initial value
P	Related to seal chamber pressure
R	Right
s	Seal, Steady
S	Stiffness, Seal circumferential distance

T	Total, Differentiating subscript
u	Related to seal circumferential fluid velocity
W	Whirl, Discharge coefficient
x	Coordinate frame direction
y	Coordinate frame direction
z	Coordinate frame direction

Greek

ϕ	Related to journal attitude angle

Other

___	Vector or matrix

Superscripts

$\dot{}$	$\frac{d}{dt}$
$\ddot{}$	$\frac{d^2}{dt^2}$
$'$	Other value, $\frac{d}{d\tau}$ (τ = tU/r)
*	Coenergy
number/variable	Exponentiation

Chapter 1 INTRODUCTION

Steam Turbine (Figure 1.1) instability in the form of precession or whirl ($\dot{\phi}$) of a rotor about a fixed reference position (Figure 1.2 - Turborotor, circumferential cross section) has received extensive study throughout this century. Such instability is characterized by cross coupled orthogonal forces acting on a turborotor to promote rotor precession (Figure 1.2) [1]. Such instability is generally classified as either forced or self excited.

Forced rotor whirl is caused by mass unbalance. It is characterized by: (1) a whirl frequency that equals rotor rotational frequency, (2) whirl amplitudes that peak within a narrow speed band (Figure 1.3 - Forced vibration attributes in Rotating Machinery), and (3) an absense of oscillatory rotor fiber stress [2] . This form of instability is usually corrected through the use of balance weights. When balance weight application does not restore turborotor stability, self excited vibrations exist.

Self excited vibrations generally are caused by flow or friction energy that generates rotor whirl [3] . Such vibrations are characterized by: (1) a whirl frequency that is nearly constant and independent of rotor rotational speed and is at or near a rotor natural frequency, (2) whirl amplitudes that suddenly increase as a particular rotor rotational speed value is achieved and continue to increase with increasing rotor speed, (3) alternating stresses in rotor fibers, caused by nonsynchronous whirl, that make self excited whirl more destructive than forced whirl [2].

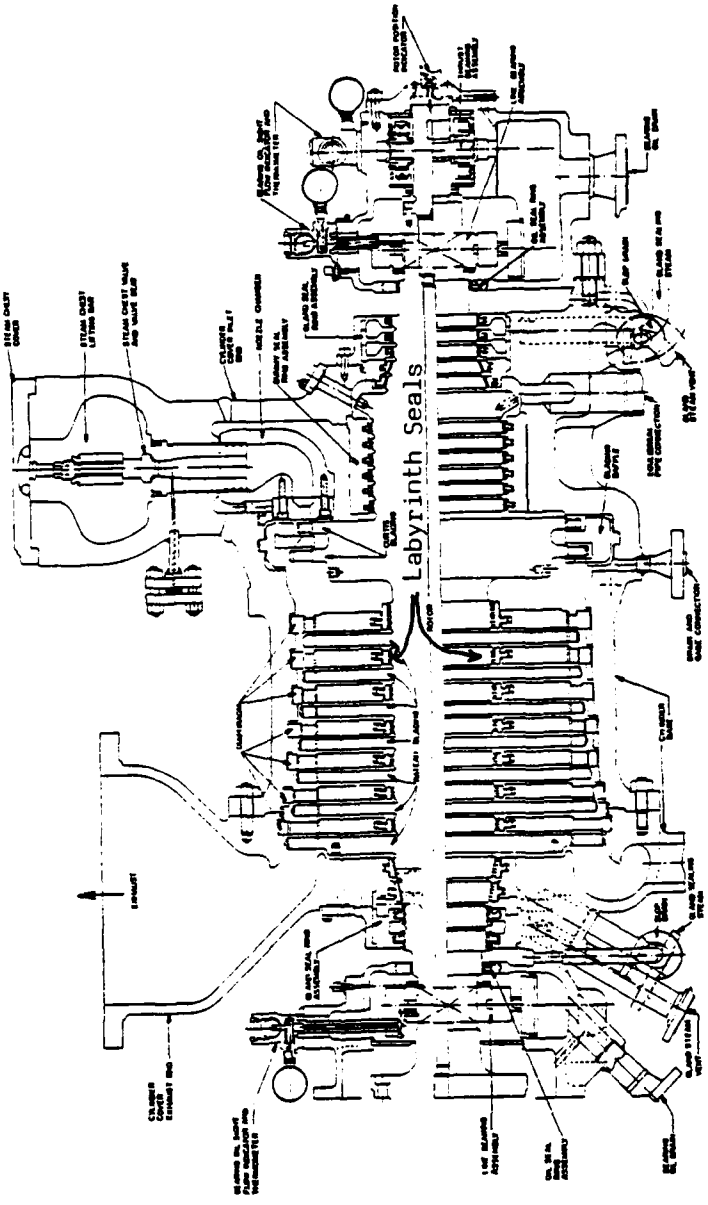

Figure 1.1 - Typical High Pressure Steam Turbine [17]

O - Static Rotor Position

O′- Steady Running Rotor Position

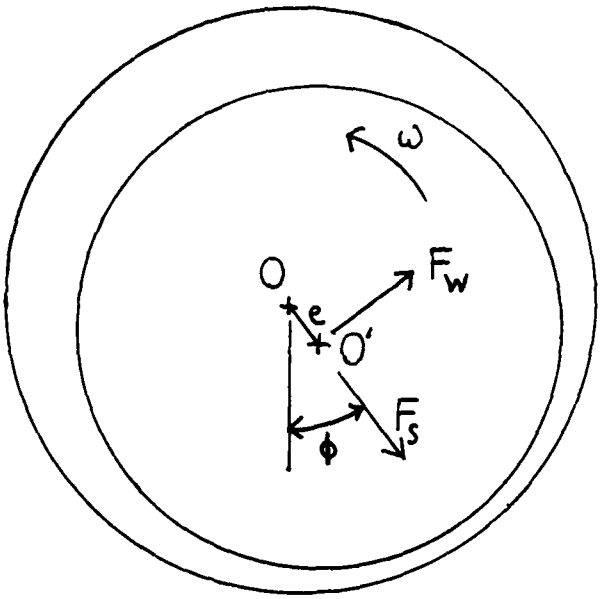

Figure 1.2 - Cross coupled Orthogonal Forces Acting on a Turborotor Simplified Circumferential Cross-sectional View

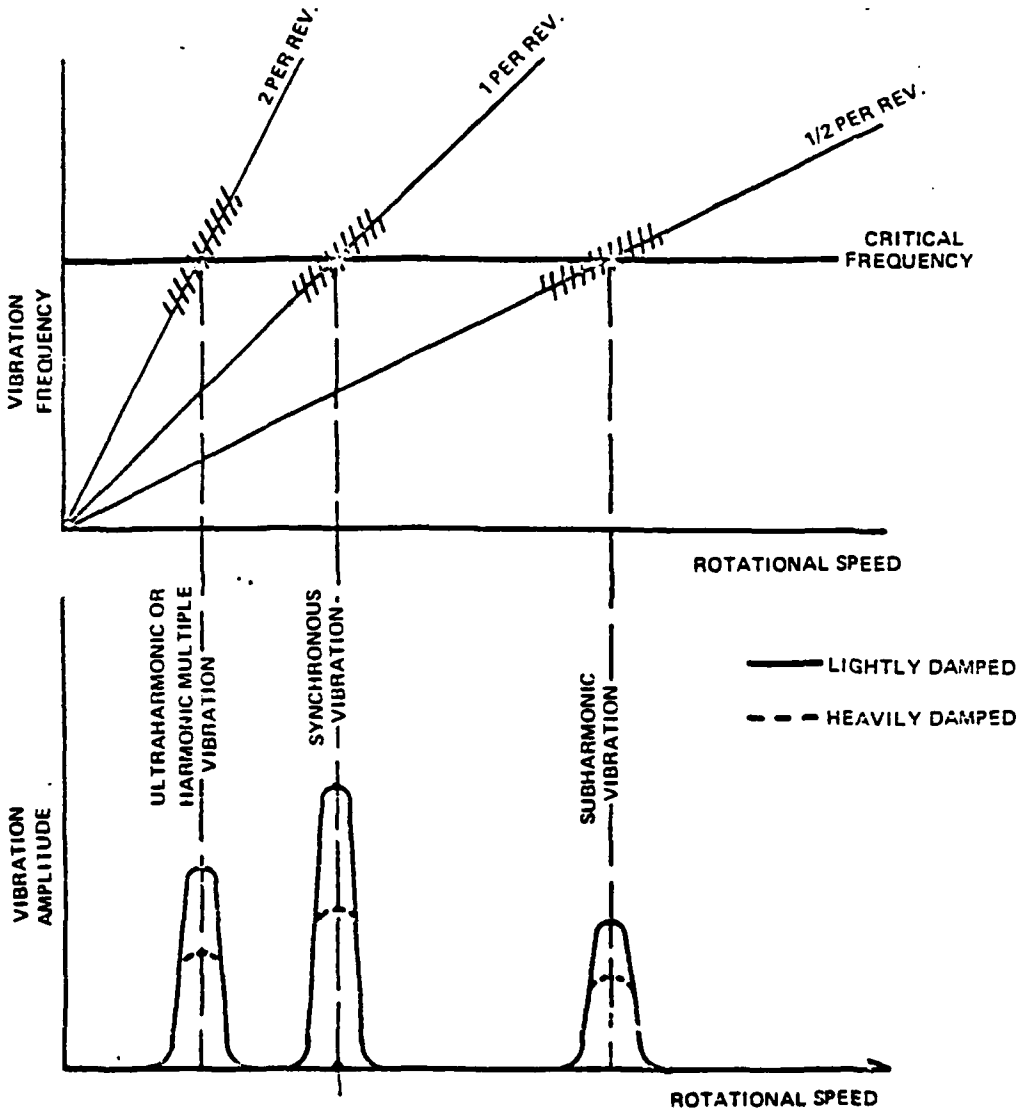

Fig. 1.3 - ATTRIBUTES OF FORCED VIBRATION OR RESONANCE IN ROTATING MACHINERY [2]

Because this instability form is as complicated as it is destructive it requires additional attention.

Instability phenomena such as Oil Whip and steam excited whirl are common forms of self excited rotor whirl. Oil Whip is journal bearing induced rotor whirl that occurs when a pressurized bearing film thickens and begins to trail the position of minimum journal to bearing clearance. (Figure 1.4 - Oil Whip)[4].

This trailing high pressure fluid region imposes a force, Fw, on the journal's centroid, normal to rotor eccentricity, e (OO' in Figure 1.4), and in the direction of rotor rotation. Rotor whirl at a frequency of ½ that of rotor rotational speed (ω) results. This whirl is further

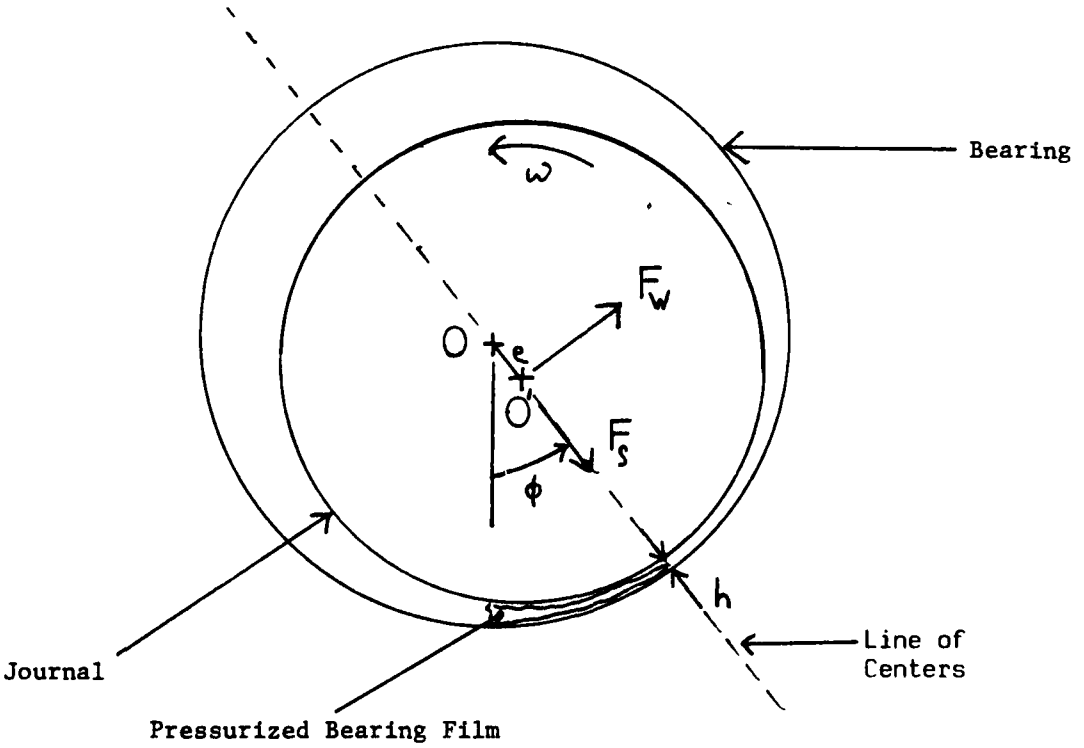

h = minimum journal to bearing clearance

Figure 1.4 - Oil Whip Transverse cross-sectional view

defined as "forward" whirl since precession ($\dot{\phi}$) occurs in the same direction as rotor rotation. Oil Whip occurs when rotor rotational frequency is increased beyond a system particular value known as the "Stability Threshold" [4]. Although improvements in bearing design have increased this threshold value in many rotor bearing systems, steam turbines must still contend with other sources of self excited whirl.

Self excited whirl energy transformed from steam flow has increasingly affected steam turbine stability with the advent of increasing upstream turbine pressures. Whirl forces (Figure 1.2), necessary to cause "Steam Whirl", are produced by unbalanced torques [3]. This torque unbalance results from higher turbine blade energy losses at high shroud to blade row clearance areas. Caused by an initial rotor deflection, steam leakage at these large clearance areas will exceed leakage at opposite smaller clearance areas (Figure 1.5). Consequently, the turbine blades nearest these high clearance annular sections will receive less fluid energy than will opposite small clearance annular section blading. The resulting unbalanced torques produce a force that acts on the rotor's centroidal axis and is orthogonal to rotor eccentricity (e).

Nonsynchrous forward whirl at the fundamental natural frequency of the rotor results. This whirl form is load dependent because degree of torque unbalance increases with increasing upstream pressure. Since Steam Whirl is a relatively new phenomenon present correction methods are limited to bearing modification and/or rotor stiffening [3]. These techniques, such as the use of tilting pad bearings, often introduce new problems. For example, tilting pad bearings provide a reduced defense against mass unbalance instability with respect to standard cylindrical

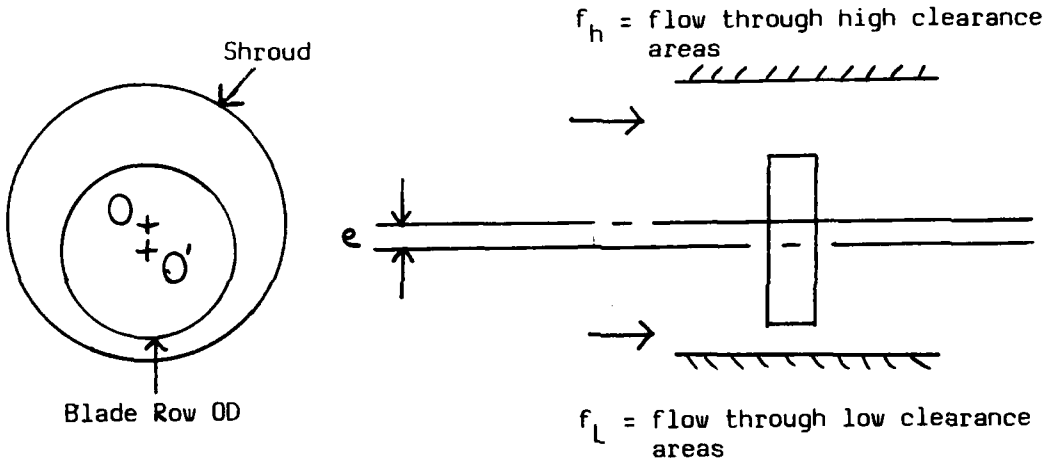

Figure 1.5 - Steam Leakage Between Turbine Shroud and Blade Row

journal bearings [5]. Therefore, alternate stabilization methods, with minimal effects, are needed to enhance whirl protection for high pressure steam turbines.

One source of such whirl protection has existed since the inception of the steam turbine. It is derived from cross coupled orthogonal forces generated by steam flow through labyrinth seals. Labyrinth seals were originally intended to reduce steam leakage between rotor and stator turbine elements by providing flow resistance [6]. Alford [7] suggested that these seals were a source of instability when rotor deflection caused seal flow area at a longitudinal cross section to be converging (Figure 1.6b). Correspondingly, he also believed that divergent seal flow area enhanced rotor stability (Figure 1.6c).

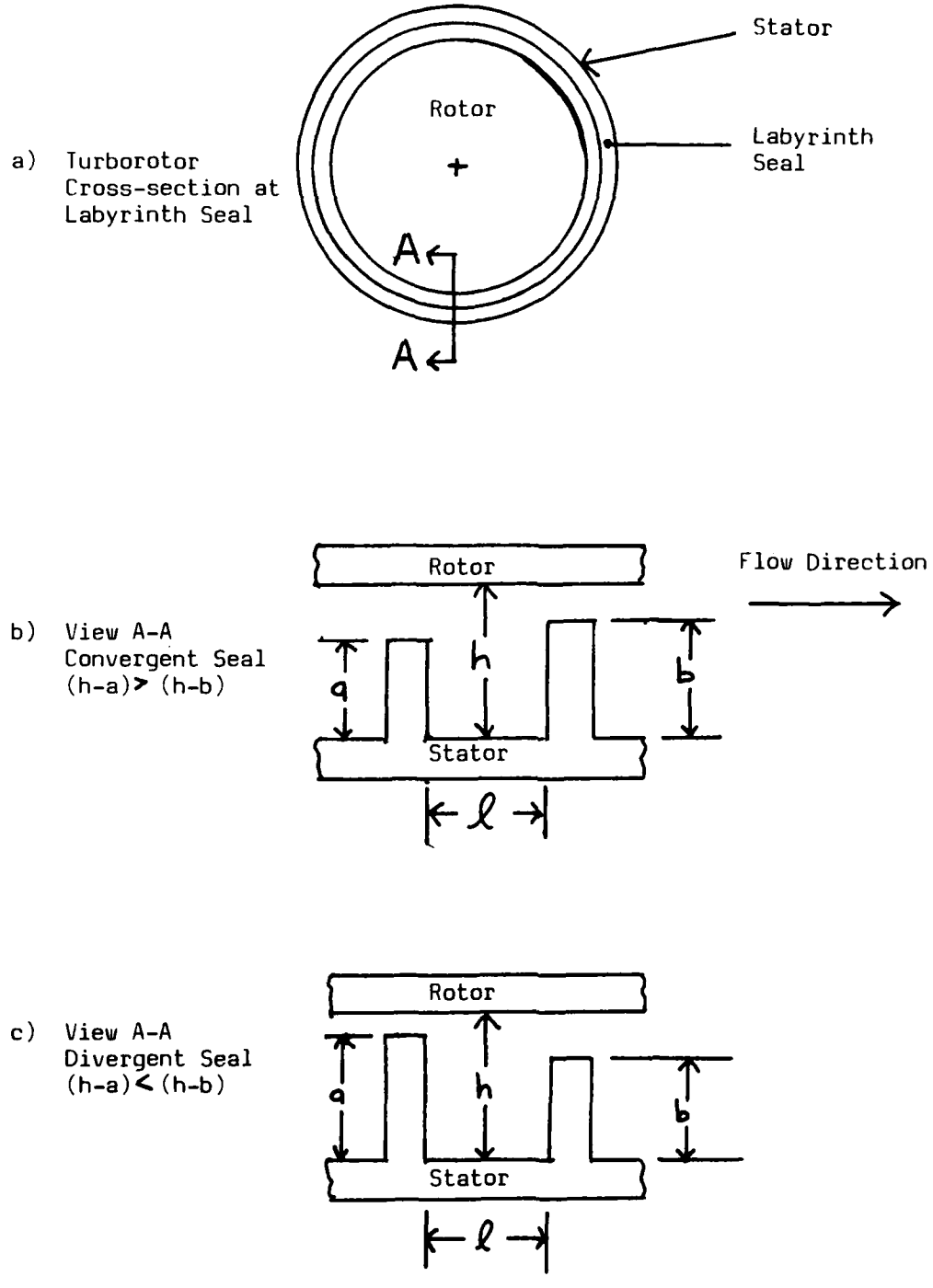

Figure 1.6 - Labyrinth Seal Geometries

Unfortunately, his analyses neglected circumferential flow through the seal cavity. Spurk and Keiper [8] made a claim directly opposite to Alford's -- that divergent seal geometry promoted instability. Unfortunately, their analysis was also incomplete. They neglected rotor rotation. Because of such disagreement, as well as potential for stability enhancement, labyrinth seal forces require more thorough study.

Shatoff [5] provides an explanation supporting Alford while still suggesting that divergent and convergent seal geometries can be either stabilizing or destabilizing depending upon other operating conditions. Figure 1.7a depicts convergent seal geometry. Here, F_e and F_ϕ are components of the resultant force produc ed by the seal (F_{Ls}). Since the whirl component of F_{Ls} (F_ϕ) exceeds the bearing damping force, forward whirl at the rotor's fundamental natural frequency results. Alternately, divergent seal geometry (Figure 1.7b) induces backward whirl at an otherwise stable rotor speed (ω).*

This suggests that "negative" bearing damping (reversed br$\dot{\phi}$ vector direction with respect to Figure 1.7a), associated with rotor speed increase beyond the threshold of Oil Whip can be offset (Figure 1.7c). Therefore, by increasing the Oil Whip stability threshold, divergent seal geometry enhances rotor bearing system stability. Similarly, since Steam Whirl is a forward whirl phenomenon that enhances oil whip instability, it too might be counteracted by backward whirl inducing divergent seal geometry. Although seemingly plausible, experimental verification is needed to prove such a theory. Wright's [9] development and operation of a seal and disc test apparatus partially

* As defined by Oil Whip

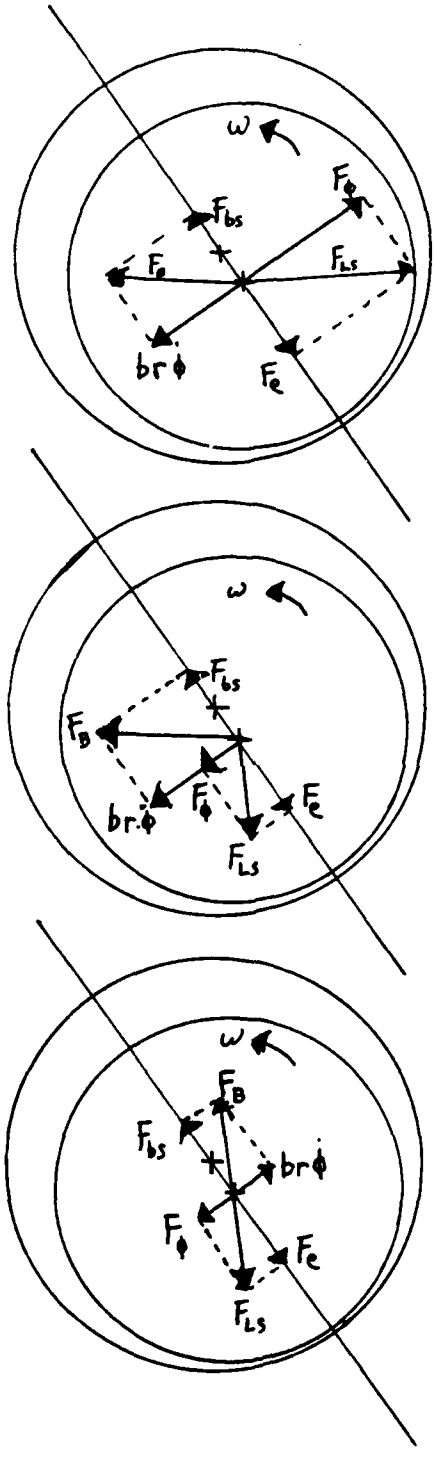

a) Convergent Seal

b) Divergent Seal

c) Divergent Seal Beyond Oil Whip Threshold

F_B = Resultant Bearing Fluid Force

$F_{bs} = k_s e + k_b e$
= Shaft and Bearing Elastic Forces

F_e = Static (elastic) Seal Force

F_ϕ = Dynamic (damping) Seal Force

$br\dot{\phi}$ = Bearing Damping Force

Figure 1.7 - Labyrinth Seal Forces

satisfies this requirement.

Wright's model was not representative of actual high pressure steam turbines. Its 8-inch diameter disc and .05 inch nominal seal strip to disc clearance were much smaller than their high pressure steam turbine counterparts. Additionally, he did not attempt to accurately scale rotor surface speed and friction factors. However, his experimental efforts did provide a basis for follow-on experimentation with actual high pressure turbine seals.

Wright's work also provides verification of Alford's theory that divergent seal geometry is stabilizing. Therefore, his results are probably, at least, qualitatively reliable and warrant some discussion.

With divergent seal geometry, Wright produced strong, self excited backward whirl -- an effect possibly capable of counteracting the forward whirl of Steam Whirl and Oil Whip. Although his model was not ideally suited for accurate convergent seal geometry experimentation, his results did indicate reduced forward whirl stability for convergent geometry relative to divergent and straight (a=b in Figure 1.6) geometries. Such consistency and apparent plausibility encouraged him to consider using his results as a basis for alternate turbine seal design. He believed that if seal geometry affected rotor stability, then design of labyrinth seals to enhance stability was possible.

Such design information must provide formulas for seal parameters and materials and be applicable for the high pressures and speeds of today's high pressure turbines. Analytical modeling is required to provide such mathematical relations. The first step in such modeling is analytical verification of Wright's results, particularly, that of stabilizing divergent seal geometry. Additionally, information

explaining the effect that other seal parameters have on rotor stability is needed. For example, increasing seal diameter is expected to enhance stability because increasing rotor and seal surface area should increase fluid friction -- an energy dissipating and, therefore, stabilizing phenomenon. Similarly, increasing seal strip separation (ℓ in Figure 1.6) should also be stabilizing.

If the individual effects of such parameters can be isolated, then design criteria will have a basis for development. Such information can allow derivation of formulas relating seal parameters and rotor stability.

The purpose of this thesis was to provide such information. Analytical verification of stability threshold increase due to divergent seal geometry was its principle aim. Since stability was defined in

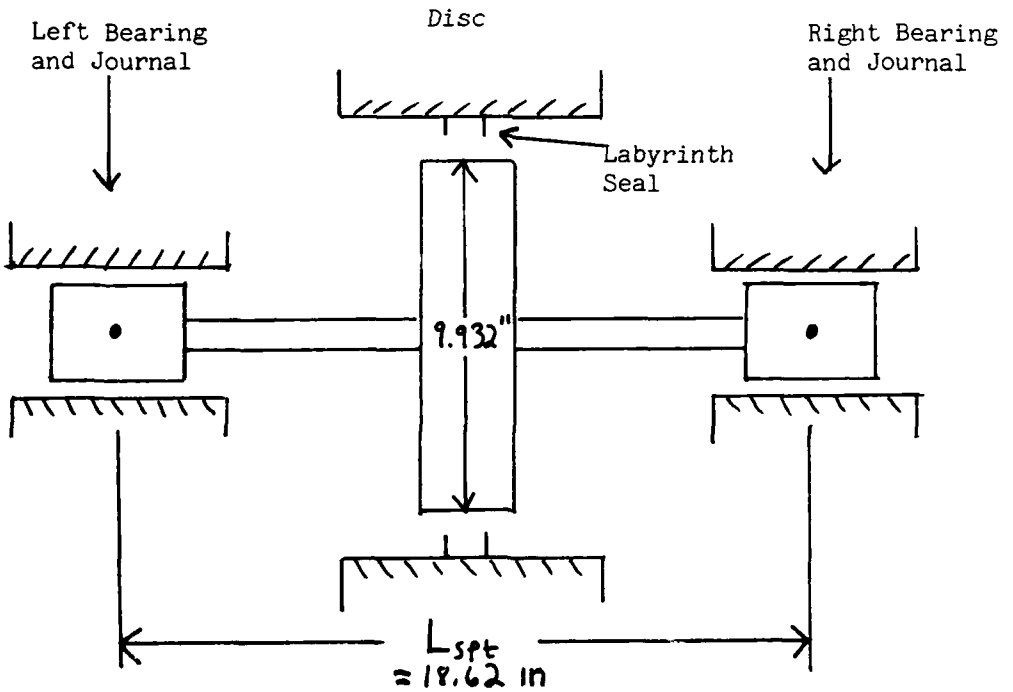

Figure 1.8 - Myrick Rotorbearing System Model with Single Labyrinth Seal [4]

terms of frequency the analytical model developed in this thesis produced root locus output. This model used a rotor bearing system similar to one described by Myrick, adding a single labyrinth seal (Figure 1.8). It was also similar to Wright's experimental apparatus. It simulated divergent, convergent, and straight seal geometries as well as variations in seal dimensions, pressure, and rotor speed. Stabilizing or destabilizing trends were available after each parameter was separately incremented.

This thesis presentation will first describe its model physically. Components will be identified and located relative to each other. Operating conditions such as pressure and temperature will be presented.

Derivation of the analytical model will follow system description. This chapter will present assumptions, derive equations of motion, and prepare these equations for computer programming. The schemes needed for such programming, as well as a listing of model parameter exercises, will also be presented. General information needed to understand these computer programs will be made available.

Test results will present and explain output generated by these computer programs. Eigenvalues will be graphed on root locus plots. Trends will be identified and explained.

Finally, conclusions based upon test results will be presented. This final chapter will, ultimately, satisfy the aim of this thesis. It will state its success or failure.

Chapter 2 SYSTEM DESCRIPTION

2.A Rotor Bearing System

The rotor bearing system described by Myrick served as the basis of this study (Figure 1.8). It consisted of 3 masses (2 journals and a disc) separated by 2 flexible shafts. Myrick's purpose was the study of rotor bearing system whirl using realistic incompressible film hydrodynamic journal bearings. Since analytical description of such bearings was complex, lengthy, and required considerable computer simulation time, Myrick's bearing model was modified to assure an infinitessimally short bearing, i.e., a bearing with fluid flow in the circumferential direction only (Figure 2.1) described by the following reduced version of the Reynold's equation:

$$\frac{\partial}{\partial z}\left(h^3 \frac{\partial P}{\partial z}\right) = \frac{6\mu U}{r}\frac{\partial h}{\partial \theta} + 12\mu U \frac{\partial h}{\partial t} \qquad (2.1)$$

Here, θ was an independent variable representing circumferential angular distance. Its datum, per Figure 2.1, coincided with the line of centers at the position of maximum journal to bearing clearance. Minimum journal to bearing clearance was represented by h. Dynamic viscosity was represented by μ, journal surface speed by U, and bearing fluid pressure by P. Axial distance was represented by z.

This short bearing simplification is supported by Myrick's

conclusion that hydrodynamic moments in finite length journal bearings

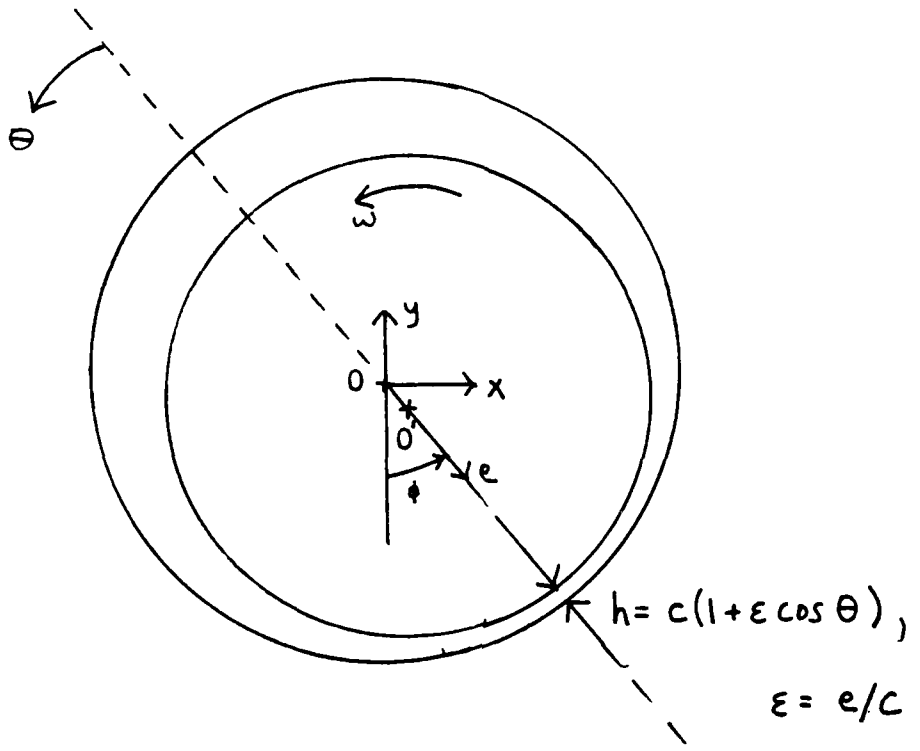

Figure 2.1 - Short Bearing Circumferential Cross-section

are small compared with shaft bending moments. Additional approximizations consistent with this short bearing assumption are: [10]

(1) Bearing and journal curvatures are small compared with film thickness.

(2) The pressure and journal to bearing clearance (h) gradients in the axial direction are much less than those in the vertical direction (y in Figure 2.1). i.e.,

$$\frac{\partial P}{\partial z} << \frac{\partial P}{\partial y} \text{ and } \frac{\partial h}{\partial z} << \frac{\partial h}{\partial y}$$ (Short Bearing)

(3) $h = c+e\cos\theta$ = minimum journal to bearing clearance where c equals radial clearance between a concentric journal and bearing.

(4) The bearing fluid is incompressible and has constant viscosity.

(5) Bearings are rigid and stationary.

The two flexible shafts were assumed to be massless. They had circular cross sections, homogeneous compositions, and no damping properties (completely elastic). These assumptions were consistent with finite element modeling necessary for computer simulation. Shaft stiffness in bending was described by the relation:

$$k_s = \frac{48\,EI}{L_{spt}^3} \qquad (2.2)$$

The centrally located disc and both journals were assumed to behave as point masses. i.e., tilting and/or deformation was neglected. Furthermore, axial displacement was also neglected. Because eccentricity ratios ($\varepsilon = e/c$) in this analysis did not exceed .5, Myrick's assumption of constant rotor speed (ω) applied for this model.* This implied an absense of shaft twist since constant rotational speed for all masses required identical rotational speed for all masses. Therefore, elastic shaft deformation occured in bending only and mass displacement occured only in a plane transverse to its axial steady state rotor position.

* Myrick's upper limit for constant rotor speed was $\varepsilon = .7$

2.B Labyrinth Seal System

The model labyrinth seal (Figure 2.2) was concentrically located about the central disc for any and all rotor bearing system steady running conditions (constant speed). Air was used as the working fluid through and within the seal to facilitate possible experimental duplication of this analysis. Downstream pressure, P_B, was constant and identical for most simulations. It represented exhaust into an ambient environment. In accordance with Kearton [11] and Kostyuk [12], fluid temperature was considered constant and axial fluid kinetic energy was considered to be completely destroyed within the seal chamber.

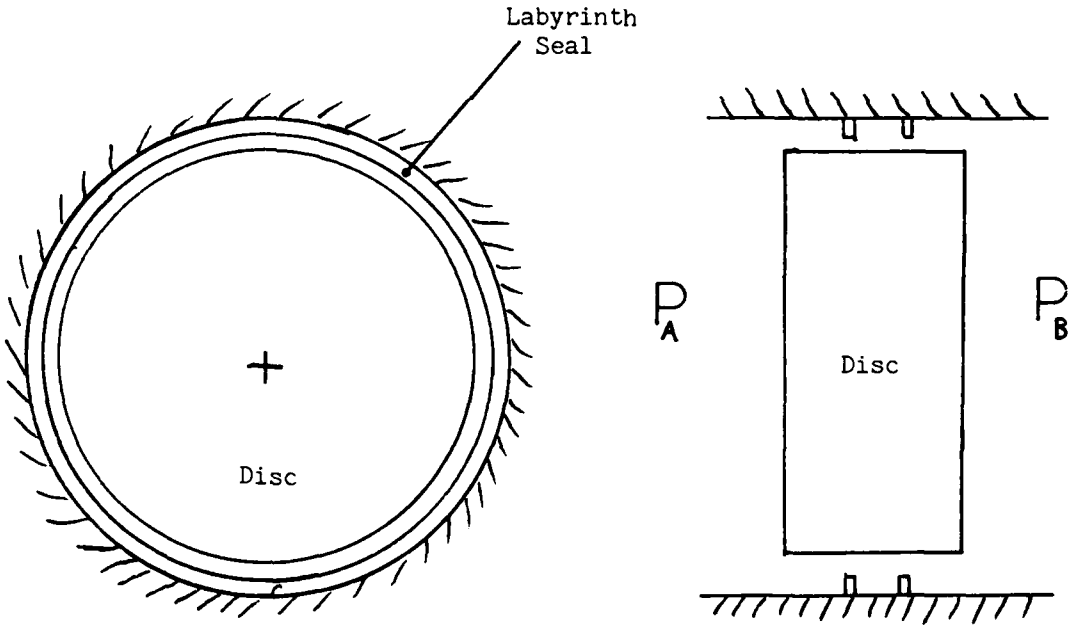

Figure 2.2 - Model Labyrinth Seal

Chapter 3 ANALYTICAL MODELING

3.A Overview

Analytical modeling of this system was actually accomplished in three phases. Each phase consisted of equation derivation and computer simulation for a particular analytical model. Equation derivation for all models occured first followed by explanations of simulation procedures.

Phase 1 developed the nonlinear rotor bearing system model. Equations of motion were derived for the rotor bearing and labyrinth seal systems separately. Using a finite difference time integration scheme, rotor bearing system operation was compared with Myrick's observation of stability threshold.

In phase 2, these rotor bearing system equations were linearized, reduced to first order form, and assembled in matrix form [1]:

$$\begin{bmatrix} 0 & \underline{I} \\ -\underline{M}^{-1}\underline{K} & -\underline{M}^{-1}\underline{B} \end{bmatrix} \begin{Bmatrix} q \end{Bmatrix} = \lambda \begin{Bmatrix} q \end{Bmatrix} \tag{3.1}$$

This formulation allowed the eigenvalues, λ , to be determined using the QR algorithm.* Corresponding eigenvectors were then obtained by subjecting the matrix in equation 3.2 to Gaussian Elimination.

* QRHMOD - available on METAPE and DYNSYS Mechanical Engineering Department computer files.

$$\left[\underline{M}\lambda^2 + \underline{B}\lambda + \underline{K}\right]\left\{\underline{v}\right\} = 0 \qquad (3.2)$$

Eigenvalues allowed root locus system representation while eigenvectors described relative state variable magnitudes in each discrete mode of system behavior. When results from these formulations matched those of Shapiro and Colsher [1] rotor bearing system modeling verification was confirmed since they similarly modeled Myrick's system*. With this assurance, a labyrinth seal model was incorporated into this rotor bearing system model during the third phase.

Labyrinth seal nonlinear modeling was more difficult than that for the rotor bearing system since both time and circumferential seal distance were bases for state variable integration. It required the use of a finite element labyrinth seal model, needed to effect seal circumferential distance integration. The expense of such an effort, in computer simulation time, was unjustified. Contrary to experience with the rotor bearing system nonlinear modeling, comparison with a nonexistent and proven seal model was impossible. Comparison of nonlinear and linear seal models' results had little value since both models derive from the same equations. Therefore, nonlinear labyrinth seal modeling did not occur beyond derivation of system equations as required for linear modeling.

Linear labyrinth seal modeling took a form somewhat different

* Calculation details are not available. Figures 4.4b and 4.5b contain these results.

from that for the rotor bearing system. Since linearization of equations of motion could not eliminate partial derivative terms, assumed solution forms were substituted for each state variable. The result was four first order, time dependent differential equations with solution form coefficients as dependent variables. The resulting matrix was subjected to the QR algorithm and Gaussian Elimination both separately and coupled to the rotor bearing system's linear model matrix. As a result, eigenvalues and eigenvectors from coupled and isolated systems were compared for a complete stability analysis.

3.B Rotor Bearing System Modeling

3.B.1 Nonlinear Equation Derivation

Initial analytical modeling of Myrick's rotor bearing system required adequate description of bearing film forces on each journal. Beaman [13] has accomplished such an analysis.

Starting from the reduced Reynold's equation (equation 2.1), an expression describing bearing pressure per unit axial distance was obtained:

$$P = -\frac{\mu}{2}\left[\frac{U}{rh^3}\frac{\partial h}{\partial \theta} + \frac{2}{h^3}\frac{\partial h}{\partial t}\right] l^3 \qquad (3.3)$$

where r = journal radius

Forces normal to and in the eccentricity direction (e - Figure 3.1) were derived by integrating bearing film pressure around the journal circumference:

$$F_e = \int_0^{\pi} P\cos\theta \, r \, d\theta \qquad (3.4a)$$

$$F_\phi = \int_0^{\pi} P\sin\theta \, r \, d\theta \qquad (3.4b)$$

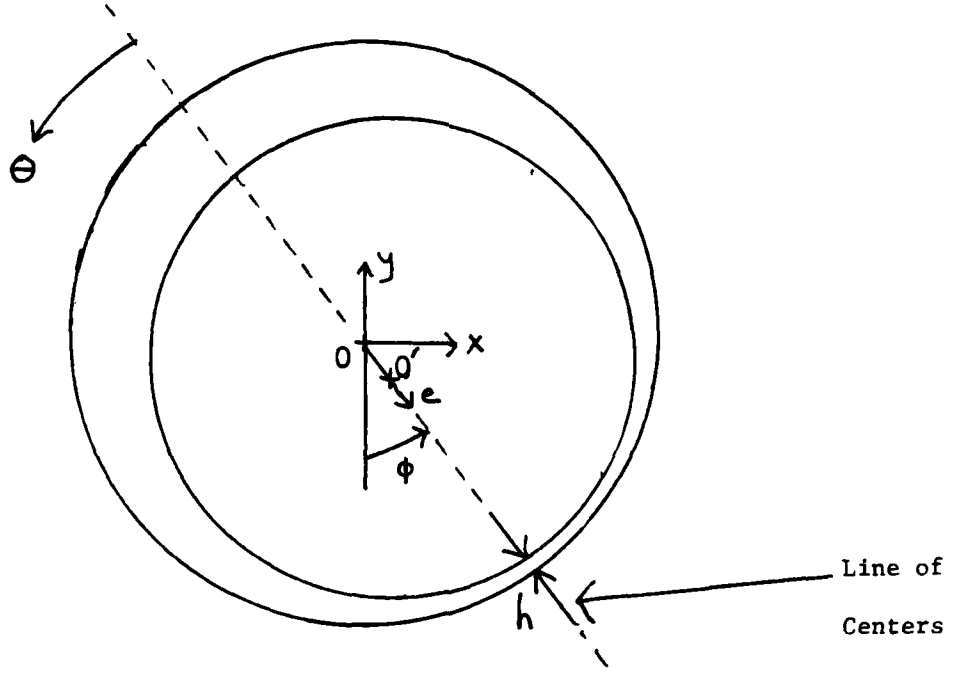

Figure 3.1 - Bearing Description, Circumferential Cross Section

These forces are generated by the bearing film and act on each journal's centroid. After integration, equations 3.4 become:

$$F_e = -\frac{\mu \ell^3 U}{2c^2}\left[\frac{(1-2\phi')2\varepsilon^2}{(1-\varepsilon^2)^2} + \frac{\pi\varepsilon'(1+2\varepsilon^2)}{(1-\varepsilon^2)^{5/2}}\right] \tag{3.5a}$$

$$F_\phi = -\frac{\mu \ell^3 U}{2c^2}\left[\frac{(2\phi'-1)\pi\varepsilon}{2(1-\varepsilon^2)^{3/2}} - \frac{4\varepsilon'\varepsilon}{(1-\varepsilon^2)^2}\right] \tag{3.5b}$$

(note: ε' and ϕ' involve differentiation with respect to $\tau = \frac{tU}{r}$)
Conversion to a standard x-y coordinate system (Figure 3.1) is easily accomplished using the following relations:

$$F_X = (F_e)\sin\phi + (F_\phi)\cos\phi \tag{3.6a}$$

$$F_Y = -(F_e)\cos\phi + (F_\phi)\sin\phi \tag{3.6b}$$

Equations 3.6 apply to both left and right bearings. They can be considered to be generalized forces acting on each journal's centroid (Figure 3.2) [14] .

Figure 3.2 depicts Myrick's model with nonlinear short bearing forces and linear x and y direction springs connecting each journal to the central disc. From this figure and Chapter 2 assumptions, two generalized coordinates for each mass were assigned (Figure 3.3).

Since all constraints imposed upon this system were holonomic, Lagrange's equations were used to derive its equations of motion [14] . Starting with the central disc, a kinetic coenergy expression was derived.

$$T_d^* = \tfrac{1}{2} m_d (\dot{x}_1^2 + \dot{x}_2^2) + \tfrac{1}{2} I_{Ad} \omega^2 \tag{3.7}$$

Disc potential energy was stated as:

$$V_d = \tfrac{1}{2} k_x \left[(x_1 - x_3)^2 + (x_1 - x_5)^2\right] + \tfrac{1}{2} k_y \left[(x_2 - x_4)^2 + (x_2 - x_6)^2\right] \tag{3.8}$$

Combining these expressions, the disc Lagrangian was expressed:

$$\mathcal{L}_d = T_d^* - V_d = \tfrac{1}{2} m_d (\dot{x}_1^2 + \dot{x}_2^2) + \tfrac{1}{2} I_{Ad} \omega^2 - \tfrac{1}{2} k_x \left[(x_1 - x_3)^2 + (x_1 - x_5)^2\right] - \tfrac{1}{2} k_y \left[(x_2 - x_4)^2 + (x_2 - x_6)^2\right] \tag{3.9}$$

Lagrange's equations (equation 3.10) for the disc were then formulated, realizing that all forces acting on the disc were conservative ($\tilde{\approx} = 0$) and that rotor angular velocity, ω, was constant and, therefore, not a generalized coordinate.

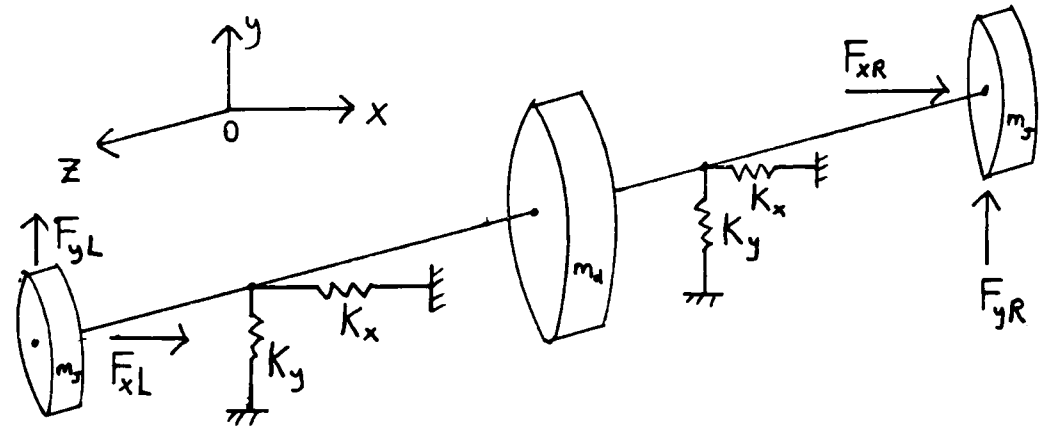

Left Journal | Disc | Right Journal

Figure 3.2 - Analytical Rotor Bearing System Model

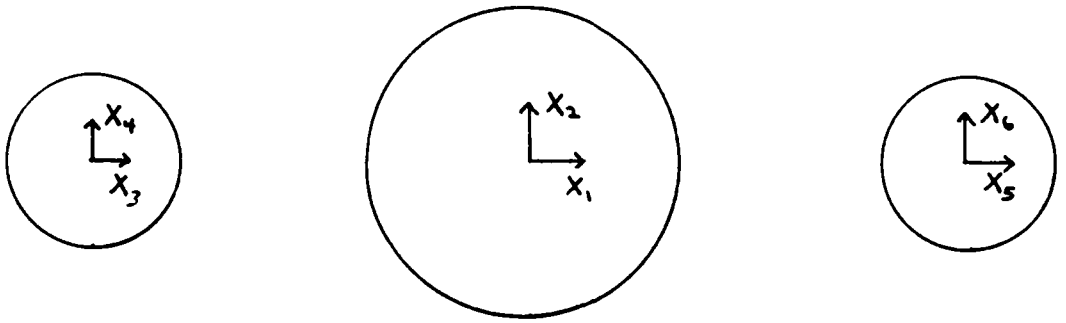

Left Journal | Disc | Right Journal

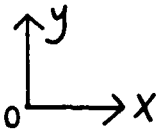

Figure 3.3 - Generalized Coordinate Assignment

$$\frac{d}{dt}\left(\frac{\partial \mathcal{L}}{\partial \dot{x}_j}\right) - \frac{\partial \mathcal{L}}{\partial x_j} = \approx_j \tag{3.10}$$

For coordinate X_1 (Figure 3.3 - G.C. assignment):

$$\ddot{X}_1 = -\frac{k_x}{m_d}(x_1 - x_3) - \frac{k_x}{m_d}(x_1 - x_5) \tag{3.11}$$

Similarly, for coordinate X_2:

$$\ddot{x}_2 = -\frac{k_y}{m_d}(x_2 - x_4) - \frac{k_y}{m_d}(x_2 - x_6) \tag{3.12}$$

Equations of motion for each journal were similarly derived. However, because bearing film forces include nonconservative damping they were represented as Generalized Forces, i.e.,

$$\approx_x = F_x \tag{3.13a}$$

$$\approx_y = F_y \tag{3.13b}$$

Proceeding for the left journal as in the derivation of disc equations:

$$T_{JL}^* = \tfrac{1}{2} m_J (\dot{x}_3^2 + \dot{x}_4^2) + \tfrac{1}{2} I_{Ad} \omega^2 \tag{3.14}$$

$$V_{JL} = \tfrac{1}{2} k_x (x_3 - x_1)^2 + \tfrac{1}{2} k_y (x_4 - x_2)^2 \tag{3.15}$$

$$\mathcal{L}_{JL} = \tfrac{1}{2}\left[m_J(\dot{x}_3^2 + \dot{x}_4^2) + I_{AJ}\omega^2 - k_x(x_3 - x_1)^2 - k_y(x_4 - x_2)^2\right] \tag{3.16}$$

Employing Lagrange's Equations (equation 3.10) and incorporating equations 3.13.

$$\ddot{x}_3 = -\frac{k_x}{m_J}(x_3 - x_1) + \frac{F_{xL}}{m_J} \tag{3.17}$$

$$\ddot{x}_4 = -\frac{k_y}{m_J}(x_4 - x_2) + \frac{F_{yL}}{m_J} \tag{3.18}$$

Similarly, for the right journal:

$$T^*_{JR} = \tfrac{1}{2}(\dot{x}_5^2 + \dot{x}_6^2) + \tfrac{1}{2} I_{AJ} \omega^2 \tag{3.19}$$

$$V_{JR} = \tfrac{1}{2} k_x (x_5 - x_1)^2 + \tfrac{1}{2} k_y (x_6 - x_2)^2 \tag{3.20}$$

$$\ddot{x}_5 = -\frac{k_x}{m_J}(x_5 - x_1) + \frac{F_{xR}}{m_J} \tag{3.21}$$

$$\ddot{x}_6 = -\frac{k_y}{m_J}(x_6 - x_2) + \frac{F_{yR}}{m_J} \tag{3.22}$$

Equations 3.11, 12, 17, 18, 21, and 22 were integrated with respect to time using a Runge Kutta finite difference technique. To do this, it was convenient to reduce these 2nd order differential equations to 1st order form. Defining the following additional variables allowed such reduction:

$$X_7 = \dot{X}_1 \tag{3.23a}$$

$$X_8 = \dot{X}_2 \tag{3.23b}$$

$$X_9 = \dot{X}_3 \tag{3.23c}$$

$$X_{10} = \dot{X}_4 \tag{3.23d}$$

$$X_{11} = \dot{X}_5 \tag{3.23e}$$

$$X_{12} = \dot{X}_6 \tag{3.23f}$$

Since these variables were not independent of x_1 through x_6 but still specified system behavior, they were labeled as state variables [14]. Rotor bearing system equations of motion were then restated:

$$\dot{X}_7 = -\frac{k_x}{m_d}(x_1 - x_3) - \frac{k_x}{m_d}(x_1 - x_5) \tag{3.24a}$$

$$\dot{X}_8 = -\frac{k_y}{m_d}(x_2 - x_4) - \frac{k_y}{m_d}(x_2 - x_6) \tag{3.24b}$$

$$\dot{x}_9 = -\frac{k_x}{m_J}(x_3 - x_1) + \frac{F_{xL}}{m_J} \tag{3.24c}$$

$$\dot{x}_{10} = -\frac{k_y}{m_J}(x_4 - x_2) + \frac{F_{yL}}{m_J} \tag{3.24d}$$

$$\dot{x}_{11} = -\frac{k_x}{m_J}(x_5 - x_1) + \frac{F_{xR}}{m_J} \tag{3.24e}$$

$$\dot{x}_{12} = -\frac{k_y}{m_J}(x_6 - x_2) + \frac{F_{yR}}{m_J} \tag{3.24f}$$

3.B.2 Linearization

Since equations 3.24c through f have nonlinear components they were not suited for a frequency domain solution, as required for root locus output. Therefore, these bearing film force terms had to be linearized.

Beaman [13] had linearized equations 3.5 to achieve the following form:

$$\begin{Bmatrix} \mathcal{F}_e \\ \mathcal{F}_\phi \end{Bmatrix} = \begin{bmatrix} K_{ee} & K_{e\phi} \\ K_{\phi e} & K_{\phi\phi} \end{bmatrix} \begin{Bmatrix} \delta e \\ \delta\phi \end{Bmatrix} + \begin{bmatrix} B_{ee} & B_{e\phi} \\ B_{\phi e} & B_{\phi\phi} \end{bmatrix} \begin{Bmatrix} \delta e' \\ \delta\phi' \end{Bmatrix} \tag{3.25}$$

where $\delta e'$ and $\delta\phi'$ indicated differentiation with respect to $\tau = tU/r$ and:*

* Stiffness and damping coefficients appear in Appendix B.

$$\tilde{F}_e = \frac{F_e c^2}{\mu \ell^3 \omega r} \tag{3.26a}$$

$$\tilde{F}_\phi = \frac{F_\phi c^2}{\mu \ell^3 \omega r} \tag{3.26b}$$

Equation 3.25 was converted to the Figure 3.1 coordinate system using the following transformation:

$$X = e \sin\phi \tag{3.27a}$$

$$y = -e \cos\phi \tag{3.27b}$$

The following transformed solution resulted:

$$\begin{Bmatrix} \tilde{F}_x \\ \tilde{F}_y \end{Bmatrix} = \begin{bmatrix} K_{xx} & K_{xy} \\ K_{yx} & K_{yy} \end{bmatrix} \begin{Bmatrix} \delta X \\ \delta y \end{Bmatrix} + \begin{bmatrix} B_{xx} & B_{xy} \\ B_{yx} & B_{yy} \end{bmatrix} \begin{Bmatrix} \delta \dot{x} \\ \delta \dot{y} \end{Bmatrix} \tag{3.28}$$

where, after equations 3.26 were incorporated:*

$$\tilde{F}_x = \frac{F_x c^2}{\mu \omega r} \tag{3.29a}$$

* Stiffness and damping coefficients appear in Appendix B.

$$\tilde{F}_y = \frac{F_y c^2}{\mu \omega r} \tag{3.29b}$$

Bearing force terms in equations 3.24c through f were then expressed in linear form using the equation 3.28 revised bearing coefficients.

$$F_{xL} = \left[\frac{\mu \omega r}{c^2}\left(k_{xx}\delta x + k_{xy}\delta y + B_{xx}\delta \dot{x} + B_{xy}\delta \dot{y}\right)\right]_L \tag{3.30a}$$

$$F_{xR} = \left[\frac{\mu \omega r}{c^2}\left(k_{xx}\delta x + k_{xy}\delta y + B_{xx}\delta \dot{x} + B_{xy}\delta \dot{y}\right)\right]_R \tag{3.30b}$$

$$F_{yL} = \left[\frac{\mu \omega r}{c^2}\left(k_{yx}\delta x + k_{yy}\delta y + B_{yx}\delta \dot{x} + B_{yy}\delta \dot{y}\right)\right]_L \tag{3.30c}$$

$$F_{yR} = \left[\frac{\mu \omega r}{c^2}\left(k_{yx}\delta x + k_{yy}\delta y + B_{yx}\delta \dot{x} + B_{yy}\delta \dot{y}\right)\right]_R \tag{3.30d}$$

With these substitutions, equations 3.23 and 3.24 became linear rotor bearing system equations of motion. They were then arranged per equations 3.1 and 3.2.

The square matrix in equation 3.1 is an algebraic manipulation of the more fundamental linear homogeneous matrix equation of motion:[18]

$$M\ddot{\underline{a}} + B\dot{\underline{a}} + K\underline{a} = 0 \tag{3.31a}$$

Where, $\underline{a}$ represents a generalized coordinate column vector and $\underline{q}$, in equation 3.1, represents a state variable column vector (not all variables are independent):

$$\underline{q} = \begin{Bmatrix} \underline{X} \\ \dot{\underline{X}} \end{Bmatrix} \tag{3.31b}$$

Equation 3.31a is reduced to 1st order form by doubling the number of variables as in equation 3.23. Equation 3.1 is further rearranged to facilitate solution:

$$\left[\lambda \underline{I} - \underline{A}\right]\{\underline{X}\} = 0 \tag{3.32a}$$

where:

$$\underline{A} = \begin{bmatrix} 0 & \underline{I} \\ -\underline{M}^{-1}\underline{K} & -\underline{M}^{-1}\underline{B} \end{bmatrix} \tag{3.32b}$$

and, [19]

$$\dot{\underline{X}} = \underline{A}\,\underline{X} \tag{3.32c}$$

Equation 3.32a was solved for λ, the system eigenvalues.

These eigenvalues were then used in the following formulation to determine the system eigenvectors ($\underline{v}$) corresponding to each eigenvalue:

$$\left[\lambda_i \underline{I} - \underline{A}\right] \left\{v_i\right\} = 0 \tag{3.33}$$

$\underline{A}$ was then developed from equations 3.23, 3.24, and 3.32b:

$$\underline{A} = \begin{bmatrix} & & & & & & 1 & & & \\ & & & & & & & 1 & & \\ & & & & & & & & 1 & \\ & & & & & & & & & 1 \\ & & & & & & & & & & 1 \\ & & & & & & & & & & & 1 \\ -\frac{2K_x}{m_d} & & \frac{K_x}{m_d} & & \frac{K_x}{m_d} & & & & & & & \\ & -\frac{2K_y}{m_d} & & \frac{K_y}{m_d} & & \frac{K_y}{m_d} & & & & & & \\ \frac{K_x}{m_d} & & -\frac{(K_{xx}+K_x)}{m_J} & -\frac{K_{xy}}{m_J} & & & & & -\frac{B_{xx}}{m_J} & -\frac{B_{xy}}{m_J} & & \\ & \frac{K_y}{m_J} & -\frac{K_{yx}}{m_J} & -\frac{(K_{yy}+K_y)}{m_J} & & & & & -\frac{B_{yx}}{m_J} & -\frac{B_{yy}}{m_J} & & \\ -\frac{K_x}{m_J} & & & & -\frac{(K_{xx}+K_x)}{m_J} & -\frac{K_{xy}}{m_J} & & & & & -\frac{B_{xx}}{m_J} & -\frac{B_{xy}}{m_J} \\ & \frac{K_y}{m_J} & & & -\frac{K_{yx}}{m_J} & -\frac{(K_{yy}+K_y)}{m_J} & & & & & -\frac{B_{yx}}{m_J} & -\frac{B_{yy}}{m_J} \end{bmatrix}$$

(assume blank spaces contain zeros) (3.34)

3.C Labyrinth Seal Modeling

3.C.1 Derivation of Equations of Motion

Figure 3.4 depicts the model labyrinth seal surrounding the central rotor bearing system disc. In this analysis the following additional assumptions were required:

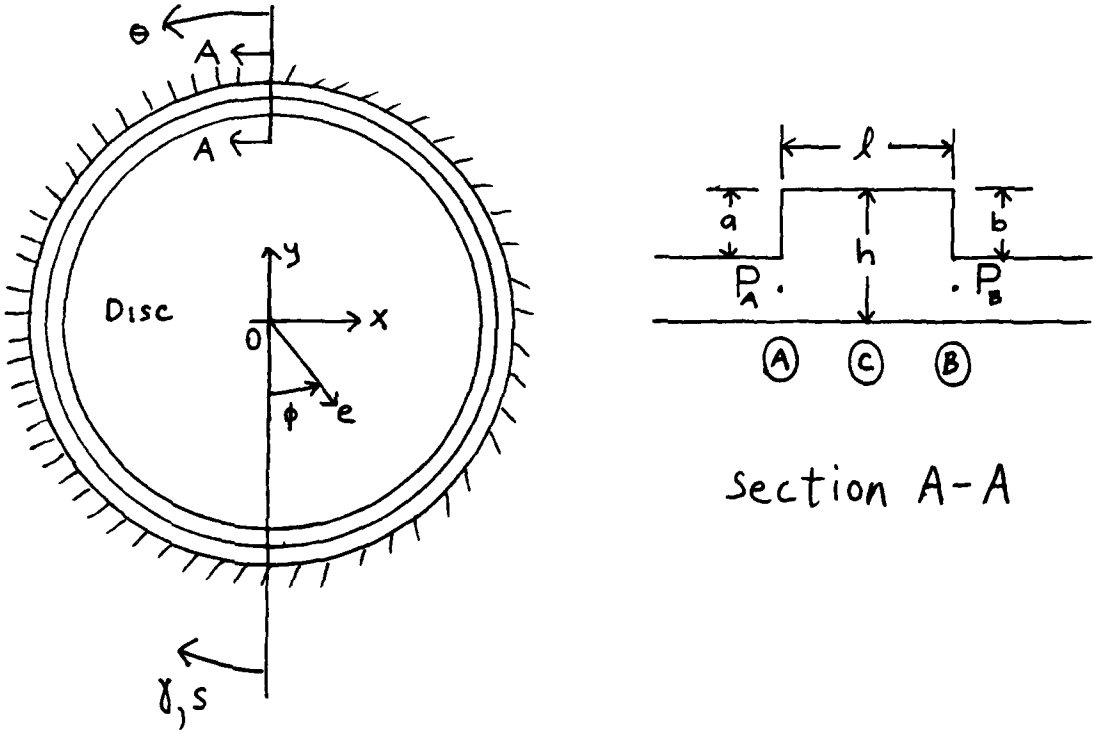

(Note: h now represents minimum seal base to disc radial clearance)

Figure 3.4 - Single Labyrinth Seal Model

1) Working fluid (air) behaves as an ideal gas: [12]

$$P = \rho R T \tag{3.35}$$

(ρ = Fluid Density, R = Gas Constant)

2) The disc is concentric within the rigid and stationary seal during steady running.

3) Fluid axial kinetic energy is completely destroyed within the seal chamber. [15]

4) This flow process is adiabatic [15].

5) Fluid temperature (T) is constant throughout the seal [6].

6) Circumferential fluid velocity during steady running is ½ that of disc surface speed and is in the direction of disc rotation: (Figure 3.5).

$$u_n = \frac{rw}{2} \tag{3.36}$$

7) Friction factors for shear forces on circumferential disc and seal surfaces are per Kostyuk [12].

$$f_i = K_{fi} \left[\frac{(rw-u)h}{2\nu} \right]^{-\frac{1}{n_i}} \tag{3.37a}$$

$$f_o = K_{fo} \left[\frac{uh}{2\nu} \right]^{-\frac{1}{n_o}} \tag{3.37b}$$

where,

$K_f = .04176$, $n = 4.38$ } $10^3 < Re < 10^5$

$K_f = .01423$, $n = 7.4$ } $10^5 < Re < 10^8$

8) Flows through seal strips A and B (Figure 3.4) are each modeled as that of an isentropic nozzle affected by a discharge coefficient [12]

9) Fluid dynamic viscosity is assumed constant.

10) Axial flow is always positive, i.e., $P_A > P_B$ (constant pressures), $P_A > P_C$, and $P_C > P_B$

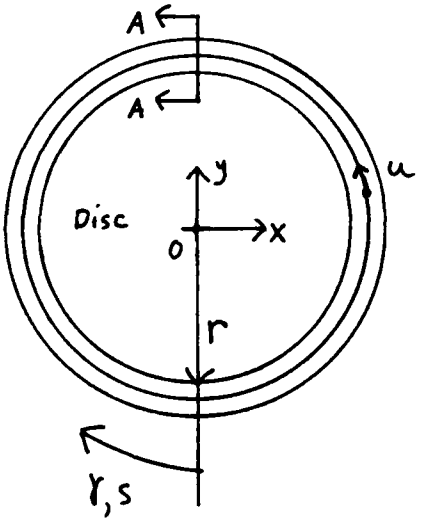

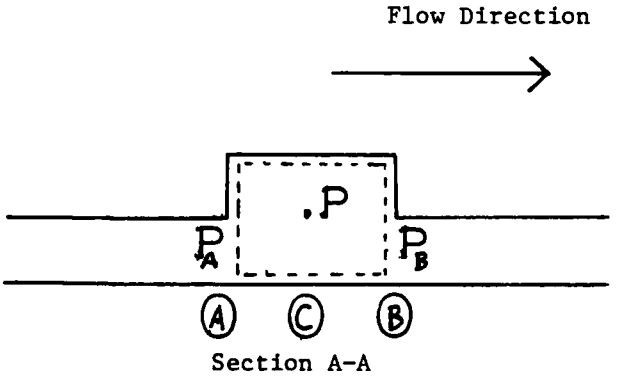

Section A-A

γ = seal angular distance (independent variable)

s = seal circumferential distance $\simeq r\gamma$

Figure 3.5 - Labyrinth Seal Control Volume

As in any compressible fluid mechanics analysis, the concepts of continuity, momentum, state, and previous assumptions were applied to the control volume of Figure 3.5. Because of the adiabatic flow assumption an energy balance was not necessary. One differential equation for each generalized coordinate resulted. In this case, two equations were expected corresponding to the generalized coordinates of chamber pressure (P) and circumferential fluid velocity (u). Minimum disc to seal base clearance (h), although variable, was not independent since it was directly related to disc behavior.

Equation 3.38 expressed the mass flow balance or continuity of the system:

$$\frac{\partial}{\partial t}(\rho h \ell) + \frac{\partial}{\partial s}(\rho h \ell u) = \dot{m}_A - \dot{m}_B \qquad (3.38)$$

[1-Cont]

Considering shear forces on circumferential and radial interior (within chamber) seal surfaces only, a momentum balance was performed:

$$(Ph\ell)_s - (Ph\ell)_{s+ds} - \tau_i \ell\, ds + \tau_o (\ell + 2h)\, ds$$

$$= \frac{\partial}{\partial t}(\rho u h \ell\, ds) - (\rho u^2 h \ell)_s + (\rho u^2 h \ell)_{s+ds} \qquad (3.39a)$$

[2-Mom]

where friction stresses were represented by:

$$\tau_i = \tfrac{1}{2} f_i \rho (r\omega - u)^2 \qquad (3.39b)$$

$$\tau_0 = \tfrac{1}{2} f_0 \rho u^2 \qquad (3.39c)$$

Differentiating equation 3.38 and substituting equation 3.35 yielded:

$$\frac{\ell h}{RT}\frac{\partial P}{\partial t} = (\dot{m}_A - \dot{m}_B) - \frac{\ell P}{RT}\frac{\partial h}{\partial t} - \frac{\ell}{RT}\left[P\left(h\frac{\partial u}{\partial s} + u\frac{\partial h}{\partial s}\right) + hu\frac{\partial P}{\partial s}\right] \qquad (3.40)$$

[1-Cont]

Equation 3.39a was also differentiated. After substituting equations 3.39b and c it became equation 3.41:

$$\frac{\ell P h}{RT}\frac{\partial u}{\partial t} = -\ell\left[P\frac{\partial h}{\partial s} + h\frac{\partial P}{\partial s}\right] + \frac{f_i P \ell}{2RT}(rw-u)^2 - \frac{f_0 P u^2}{2RT}(\ell+2h) - \frac{\ell}{RT}\left[P\left(u\frac{\partial h}{\partial t} + u^2\frac{\partial h}{\partial s} + 2uh\frac{\partial u}{\partial s}\right) + uh\frac{\partial P}{\partial t} + u^2 h\frac{\partial P}{\partial s}\right] \qquad (3.41)$$

[2-Mom]

Equation 3.40 required the following mass flow rate substitutions [16]:

$$\dot{m}_A = (h-a)\,2\pi r\sqrt{\frac{k}{RT}}\,P_A\,C_{WA}\left[\frac{M_A}{\left(1+\left(\frac{k-1}{2}\right)M_A^2\right)^{(k+1)/2(k-1)}}\right] \quad (3.42)$$

$$\dot{m}_B = (h-b)\,2\pi r\sqrt{\frac{k}{RT}}\,P_B\,C_{WB}\left[M_B\sqrt{1+\left(\frac{k-1}{2}\right)M_B^2}\right] \quad (3.43)$$

Where C_{WA} and C_{WB} represented empirical discharge coefficients for seal strips A and B respectively:

$$C_{WA} = f(P/P_A) + \text{constant} \quad (3.44a)$$

$$C_{WB} = f(P/P_B) + \text{constant} \quad (3.44b)$$

Mach numbers M_A and M_B were functions of chamber pressure, P. (see equations B.23 and B.24)

3.C.2 Linearization

Since a linear solution of equations 3.40 and 3.41 was desired, these equations were linearized and arranged in a form compatible with equation 3.32C. To begin linearization, the small motion substitutions of equations 3.45 were made:

$P = P_n + \delta P$ = Chamber pressure (3.45a)

$h = h_n + \delta h$ = Seal Base to Disc Clearance (3.45b)

$u = u_n + \delta u$ = Circumferential fluid velocity (3.45c)

$f_i = f_{in} + \delta f_i$ = Friction Factor at Disc surface (3.45d)

$f_o = f_{on} + \delta f_o$ = Friction Factor at Seal Base (3.45e)

$\dot{m}_A = \dot{m}_{An} + \delta \dot{m}_A$ = Mass Flow Rate at Seal Strip A (3.45f)

$\dot{m}_B = \dot{m}_{Bn} + \delta \dot{m}_B$ = Mass Flow Rate at Seal Strip B (3.45g)

$M_A = M_{An} + \delta M_A$ = Mach number at Seal Strip A (3.45h)

$M_B = M_{Bn} + \delta M_B$ = Mach number at Seal Strip B (3.45i)

$C_{WA} = C_{WAn} + \delta C_{WA}$ = Discharge Coefficient at A (3.45j)

$C_{WB} = C_{WBn} + \delta C_{WB}$ = Discharge Coefficient at B (3.45k)

Mass flow rates in equation 3.40 were linearized. Therefore, M_A and M_B required definition. Since these were axial flow rates only, they were not functions of circumferential velocity, u. The following general relations applied and were substituted into equations 3.45f and g:

$$\delta \dot{m}_A = \left[K_{PmA}\right]\delta P + \left[K_{hmA}\right]\delta h \tag{3.46a}$$

$$\delta \dot{m}_B = \left[K_{PmB}\right]\delta P + \left[K_{hmB}\right]\delta h \tag{3.46b}$$

The "K" coefficients in equations 3.46 were derived from linearization of equations 3.42 and 3.43 with the following substitutions:

$$f(M_A) = \frac{M_A}{\left(1 + \left(\frac{K-1}{2}\right)M_A^2\right)^{(K+1)/2(K-1)}} \tag{3.47a}$$

$$\mathcal{F}(M_B) = M_B\sqrt{1 + \left(\frac{K-1}{2}\right)M_B^2} \tag{3.47b}$$

$$K_A = \sqrt{\frac{k}{RT}}\ P_A \tag{3.47c}$$

$$K_B = \sqrt{\frac{k}{RT}}\ P_B \tag{3.47d}$$

$$C_{WA} = -.3179464\left(\frac{P}{P_A}\right) + .91723729 \tag{3.47e}$$

$$C_{WB} = -.3179464\left(\frac{P_B}{P}\right) + .91723729 \tag{3.47f}$$

$$A_{An} = (h - a)\, 2\pi r \tag{3.47g}$$

$$A_{Bn} = (h - b)\, 2\pi r \tag{3.47h}$$

Equations 3.47e and f represented linearized approximations of J.A. Perry's graphical discharge coefficient relation for sharp edged orifice meters.* Incorporating equations 3.47 into equations 3.46 yielded equations 3.48.

$$\delta \dot{m}_A = K_A \left\{ A_{An} \left[C_{WAn}\, \delta\left(f(M_A)\right) + f(M_A)_n\, \delta C_{WA} \right] + C_{WAn}\, f(M_A)_n\, \delta A_A \right\} \tag{3.48a}$$

$$\delta \dot{m}_B = K_B \left\{ A_{Bn} \left[C_{WBn}\, \delta\left(\tilde{f}(M_B)\right) + \tilde{f}(M_B)_n\, \delta C_{WB} \right] + C_{WBn}\, \tilde{f}(M_B)_n\, \delta A_B \right\} \tag{3.48b}$$

Previously undefined terms in equations 3.48 required definition:**

$$\delta A_A = 2\pi r\, \delta h \quad ; \quad A_{An} = (h_n - a)\, 2\pi r \tag{3.49a}$$

* This graph appears on page 100 of [20] .

** "K" coefficient expressions appear in Appendix B.

$$\delta A_B = 2\pi r h \quad ; \quad A_{Bn} = (h_n - b)2\pi r \tag{3.49b}$$

$$C_{WAn} = -.3179464\left(\frac{P_n}{P_A}\right) + .91723729 \tag{3.49c}$$

$$C_{WBn} = -.3179464\left(\frac{P_B}{P_n}\right) + .91723729 \tag{3.49d}$$

$$\delta C_{WA} = K_{\delta CWA}\, \delta P \tag{3.49e}$$

$$\delta C_{WB} = K_{\delta CWB}\, \delta P \tag{3.49f}$$

$$\delta(f(M_A)) = K_{\delta fMA}\, \delta M_A \tag{3.49g}$$

$$\delta(\tilde{f}(M_B)) = K_{\delta \tilde{f}MB}\, \delta M_B \tag{3.49h}$$

$$\delta M_A = K_{\delta MA}\, \delta P \tag{3.49i}$$

$$\delta M_B = K_{\delta MB}\, \delta P \tag{3.49j}$$

$$f(M_A)_n = f(M_{An}) \tag{3.49k}$$

$$\tilde{f}(M_B)_n = \tilde{f}(M_{Bn}) \tag{3.49l}$$

Therefore;

$$\delta(f(M_A)) = K_{\delta fMA} K_{\delta MA} \delta P = K_{\delta fMAT} \delta P \tag{3.49m}$$

$$\delta(\tilde{f}(M_B)) = K_{\delta \tilde{f}MB} K_{\delta MB} \delta P = K_{\delta \tilde{f}MBT} \delta P \tag{3.49n}$$

Coefficients in equations 3.46 were then described in terms of equations 3.47, 3.48, and 3.49:

$$K_{pmA} = \frac{K_A}{2\pi r}\left[A_{An}\left(C_{WAn} K_{\delta fMAT} + f(M_A)_n K_{\delta CWA}\right)\right] \tag{3.50a}$$

$$K_{pmB} = \frac{K_B}{2\pi r}\left[A_{Bn}\left(C_{WBn} K_{\delta \tilde{f}MBT} + \tilde{f}(M_B)_n K_{\delta CWB}\right)\right] \tag{3.50b}$$

$$K_{hmA} = K_A C_{WAn} f(M_A)_n \tag{3.50c}$$

$$K_{hmB} = K_B \, C_{WAn} \, \tilde{\mathcal{F}}(M_B)_n \tag{3.50d}$$

Realizing that, during steady motion, nominal axial flow rates at A and B (Figure 3.5) were equal ($\dot{m}_{An} = \dot{m}_{Bn}$), equations 3.40 and 3.41 were expressed in terms of the small motion substitutions of equations 3.45:

$$\left[\ell h_n\right]\frac{\partial \delta P}{\partial t} = \left[(K_{pmA} - K_{pmB})RT\right]\delta P + \left[(K_{hmA} - K_{hmB})RT\right]\delta h + \left[-\ell P_n\right]\frac{\partial \delta h}{\partial t} + \left[-\ell P_n u_n\right]\frac{\partial \delta h}{\partial s} + \left[-\ell P_n h_n\right]\frac{\partial \delta u}{\partial s} + \left[-\ell h_n u_n\right]\frac{\partial \delta P}{\partial s} \tag{3.51}$$

[1-Cont]

$$\left[\frac{f_{in}}{2RT}\left((r\omega)^2 - 2u_n r\omega + u_n^2\right)\ell - \frac{f_{on}u_n^2}{2RT}(\ell+2h_n) + K_{sfip} + K_{sfop}\right]\delta P + \left[-\frac{f_{on}P_n u_n^2}{RT} + K_{sfih} + K_{sfoh}\right]\delta h + \left[\frac{f_{in}P_n}{RT}(r\omega - u_n)\ell - \frac{f_{on}P_n u_n(\ell+2h_n)}{RT} + K_{sfiu} + K_{sfou}\right]\delta u + \left[\frac{-\ell}{RT}u_n h_n\right]\frac{\partial \delta P}{\partial t} + \left[-\frac{\ell u_n^2 h_n}{RT} - \ell h_n\right]\frac{\partial \delta P}{\partial s} + \left[\frac{-\ell}{RT}P_n u_n\right]\frac{\partial \delta h}{\partial t} + \left[-\ell P_n - \frac{\ell P_n u_n^2}{RT}\right]\frac{\partial \delta h}{\partial s} + \left[\frac{-\ell P_n h_n}{RT}\right]\frac{\partial \delta u}{\partial t} + \left[-\frac{2\ell P_n u_n h_n}{RT}\right]\frac{\partial \delta u}{\partial s} = 0 \tag{3.52}$$

[2-Mom]

The friction related coefficients in equation 3.52 exist because friction factors f_i, f_o are functions of state variables - p, u, and h.*

$$K_{\delta f_{xx}} = f(P, u, h) \tag{3.53}$$

Equations 3.51 and 3.52 were then expressed more compactly:

$$-[K_{1PT}]\frac{\partial \delta P}{\partial t} + [K_{1P}]\delta P + [K_{1h}]\delta h + [K_{1ht}]\frac{\partial \delta h}{\partial t} + [K_{1hs}]\frac{\partial \delta h}{\partial s}$$

$$+[K_{1us}]\frac{\partial \delta u}{\partial s} + [K_{1Ps}]\frac{\partial \delta P}{\partial s} = 0 \tag{3.54}$$

[1-Cont]

$$[K_{2P}]\delta P + [K_{2h}]\delta h + [K_{2u}]\delta u + [K_{2Pt}]\frac{\partial \delta P}{\partial t}$$

$$+[K_{2Ps}]\frac{\partial \delta P}{\partial s} + [K_{2ht}]\frac{\partial \delta h}{\partial t} + [K_{2hs}]\frac{\partial \delta h}{\partial s} + [K_{2ut}]\frac{\partial \delta u}{\partial t}$$

$$+[K_{2us}]\frac{\partial \delta u}{\partial s} = 0 \tag{3.55}$$

[2-Mom]

* Appendix B

These linearized continuity and momentum equations were not compatible with the linearized rotor bearing system model (equation 3.32c) because partial derivations with respect to both time and circumferential distance existed. The linear rotor bearing system model was based upon time as the only independent variable. Consequently, these linearized seal equations could not be coupled within the A matrix of equation 3.34. Therefore, it was necessary to reconfigure equations 3.54 and 3.55 such that partial derivatives no longer appeared and time became the only independent variable. One approach involved substitution of the following assumed solution forms into equations 3.54 and 3.55:

$$\delta P = (A_p \cos\gamma + B_p \sin\gamma)\, e^{\lambda t} \tag{3.56a}$$

$$\delta u = (A_u \cos\gamma + B_u \sin\gamma)\, e^{\lambda t} \tag{3.56b}$$

$$\delta h = H_h e^{\lambda t} \tag{3.56c}$$

Refering to Figure 3.4 (Seal Model) and remembering that, during steady running, the disc is concentric within the seal, equation 3.56c was rewritten:

$$\delta h = -\delta y \cos\gamma e^{\lambda t} \; ; \text{ for } e_n = 0 \text{ and } \phi_n = 0$$

$$\delta h = \delta e \cos\gamma e^{\lambda t} \tag{3.57}$$

$$\delta h = -H \cos\gamma e^{\lambda t}$$

Therefore, H represents disc displacement in the y direction (Figure 3.4), i.e.,

$$\delta y = Y e^{\lambda t} \tag{3.58a}$$

and, from equation 3.56c:

$$H_h = -H \cos\gamma \tag{3.58b}$$

therefore,

$$\delta h = -Y \cos\gamma \, e^{\lambda t} \tag{3.58c}$$

or,

$$H = Y \quad \text{and} \quad \dot{H} = \dot{Y} \tag{3.58d}$$

Substituting equations 3.56 into equations 3.54 and 3.55 yields time dependent differential equations without partial derivatives;

$$\dot{A}_p = \left(\frac{K_{1P}}{K_{1Pt}}\right)A_P + \left(\frac{K_{1Ps}}{r K_{1Pt}}\right)B_P + \left(\frac{K_{1us}}{r K_{1Pt}}\right)B_u + \left(\frac{-K_{1h}}{K_{1Pt}}\right)H + \left(\frac{-K_{1hs}}{K_{1Pt}}\right)\dot{H} \tag{3.59a}$$

$$\dot{B}_p = \left(\frac{-K_{1Ps}}{r K_{1Pt}}\right)A_P + \left(\frac{K_{1P}}{K_{1Pt}}\right)B_P + \left(\frac{-K_{1us}}{r K_{1Pt}}\right)A_u + \left(\frac{K_{1hs}}{r K_{1Pt}}\right)H \tag{3.59b}$$

$$\dot{A}_u = \left(\frac{-K_{2P}}{K_{2ut}} - \frac{K_{2Pt}K_{1P}}{K_{1Pt}K_{2ut}}\right)A_P + \left(\frac{-K_{2Pt}K_{1Ps}}{r K_{1Pt}K_{2ut}} - \frac{K_{2Ps}}{r K_{2ut}}\right)B_P + \left(\frac{-K_{2u}}{K_{2ut}}\right)A_u + \left(\frac{-K_{2Pt}K_{1us}}{r K_{1Pt}K_{2ut}} - \frac{K_{2us}}{r K_{2ut}}\right)B_u + \left(\frac{K_{2Pt}K_{1h}}{K_{1Pt}K_{2ut}} + \frac{K_{2h}}{K_{2ut}}\right)H + \left(\frac{K_{2Pt}K_{1ht}}{K_{1Pt}K_{2ut}} + \frac{K_{2ht}}{K_{2ut}}\right)\dot{H} \tag{3.59c}$$

$$\dot{B}_u = \left(\frac{K_{2Pt}K_{1Ps}}{r K_{1Pt}K_{2ut}} + \frac{K_{2Ps}}{r K_{2ut}}\right)A_P + \left(\frac{-K_{2P}}{K_{2ut}} - \frac{K_{2Pt}K_{1P}}{K_{2Pt}K_{2ut}}\right)B_P + \left(\frac{K_{2Pt}K_{1us}}{r K_{1Pt}K_{2ut}} + \frac{K_{2us}}{r K_{2ut}}\right)A_u + \left(-\frac{K_{2u}}{K_{2ut}}\right)B_u + \left(\frac{-K_{2Pt}K_{1hs}}{r K_{1Pt}K_{2ut}} - \frac{K_{2hs}}{r K_{2ut}}\right)H \tag{3.59d}$$

Linearized seal equations were then present in a form similar to equation 3.32c:

$$\begin{Bmatrix} \dot{A}_P \\ \dot{B}_P \\ \dot{A}_u \\ \dot{B}_u \end{Bmatrix} = \begin{bmatrix} K_{aAP} & K_{aBP} & 0 & K_{aBu} \\ K_{bAP} & K_{bBP} & K_{bAu} & 0 \\ K_{cAP} & K_{cBP} & K_{cAu} & K_{cBu} \\ K_{dAP} & K_{dBP} & K_{dAu} & K_{dBu} \end{bmatrix} \begin{Bmatrix} A_P \\ B_P \\ A_u \\ B_u \end{Bmatrix}$$

$$+ \begin{Bmatrix} K_{aH} \\ K_{bH} \\ K_{cH} \\ K_{dH} \end{Bmatrix} H + \begin{Bmatrix} K_{aHd} \\ 0 \\ K_{cHd} \\ 0 \end{Bmatrix} \dot{H}$$

(3.60)

Because H=Y represented disc displacement in the y direction it also corresponded to X_2. Consequently, $\dot{H} = X_8$. Equation 3.60, therefore, included the effect that the disc has upon the seal. To complete coupling between seal and rotor bearing systems, seal force exerted on the disc was also specified.

Since linearization involved infinitessimal variations of state variables, seal force acting on the disc was so represented. (See Figure 3.4 - Seal Model)

$$\delta F_x = \int_0^{2\pi} P \sin\gamma \; \ell_r \, d\gamma \qquad (3.61a)$$

$$\delta F_y = \int_0^{2\pi} P \cos\gamma \, \ell \, r \, d\gamma \tag{3.61b}$$

To accommodate these integrations, equation 3.56a can be expressed as in equation 3.62:

$$P = \bar{A}_p(t) \cos\gamma + \bar{B}_p(t) \sin\gamma \tag{3.62}$$

Substitution into equations 3.61 yields:

$$\delta F_x = \bar{B}_p \, \pi \, r \ell \tag{3.63a}$$

$$\delta F_y = \bar{A}_p \, \pi \, r \ell \tag{3.63b}$$

Since the datum for independent variable time in equation 3.32c was arbitrary, $t_o = 0$ was chosen. Consequently, $e^{\lambda t_o} = 1$ and:

$$\bar{A}_p(t_o) = A_p \tag{3.64a}$$

$$\bar{B}_p(t_o) = B_p \tag{3.64b}$$

Therefore, seal to rotor bearing system coupling was accomplished. Equation 3.65 depicted the A matrix of equation 3.34 expanded to 16 x 16 to include equations 3.60 and 3.63:

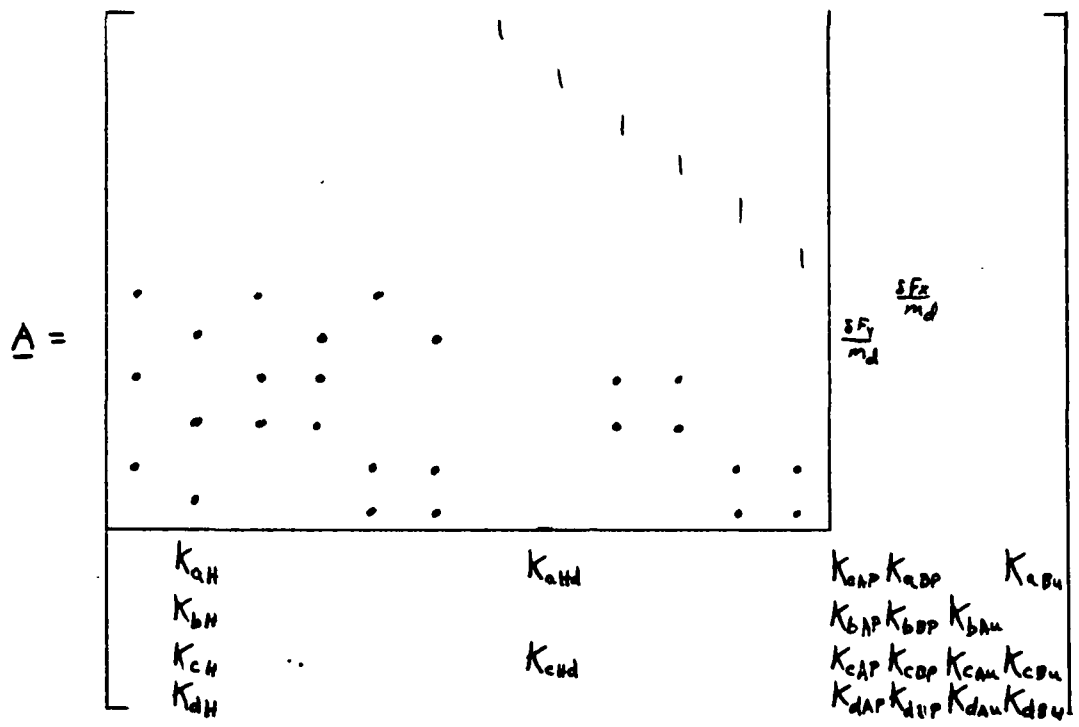

(Blank spaces contain zeros: upper left hand corner is the A matrix of equation 3.34)

(3.65)

Equation 3.65 was then used to generate eigenvalues and eigenvectors for the rotor bearing and labyrinth seal systems, both isolated and coupled.

3.D Simulation Procedure

This section will explain the programming schemes* needed to

* Listed in Appendix A.

exercise the nonlinear rotor bearing system (equations 3.23 and 3.24) and the A matricies of equations 3.34 and 3.65. Programming of the nonlinear rotor bearing system model will be discussed first. Programming of both rotor bearing and labyrinth seal systems linear models will be explained next to be followed by a description of parameter variations.

The parameter variations section of this chapter will focus primarily upon labyrinth seal physical variables. Myrick's rotor bearing system will experience minor changes only, to minimize impact on possible follow on experimental verification. Such testing will provide data for analysis in Chapter 4.

3.D. 1 Isolated Rotor Bearing System Testing

3.D.1.A Nonlinear Model Programming (RW5)

As previously mentioned, nonlinear rotor bearing system modeling was intended as a modeling accuracy check. Its basis was a 4th order Runge Kutta finite difference integration of equations 3.23 and 3.24. Although ε and ϕ in Figure 3.1 (Bearing description) were directly related to bearing generalized coordinates X_3 through X_6, they were also separately integrated to simplify bearing force calculations (equations 3.5). The coordinate assignments of equations 3.23 and 3.24 did not change. Additional bearing state variable assignments were per equations 3.66:

$$X_{13} = \varepsilon_L = \frac{(X_3^2 + X_4^2)}{C} \qquad \text{= Left Journal Eccentricity ratio} \qquad (3.66a)$$

where c = Journal to bearing radial clearance

$$X_{14} = \phi_L = \tan\left(\frac{X_3}{-X_4}\right)$$ = Left Journal Attitude Angle (3.66b)

$$X_{15} = \varepsilon_R = \frac{(X_5^2 + X_6^2)}{C}$$ = Right Journal Eccentricity ratio (3.66c)

$$X_{16} = \phi_R = \tan\left(\frac{X_5}{-X_6}\right)$$ = Right Journal Attitude Angle (3.66d)

First derivative expressions for these new state variables were also required:

$$F_{13} = \frac{(X_3 X_9 + X_4 X_{10})}{X_{13} C^2} = \dot{\varepsilon}_L$$ (3.66e)

$$F_{14} = -\frac{(X_4 X_9 - X_3 X_{10})}{(X_{13} C)^2} = \dot{\phi}_L$$ (3.66f)

$$F_{15} = \frac{(X_5 X_{11} + X_6 X_{12})}{X_{15} c^2} = \dot{\varepsilon}_R \qquad (3.66g)$$

$$F_{16} = -\frac{(X_6 X_{11} - X_5 X_{12})}{(X_{15} c)^2} = \dot{\phi}_R \qquad (3.66h)$$

Since journal surface speed ($U = r\omega$) in equations 3.5 required specification of angular velocity an expression from Cameron [10] was used:

$$\omega = \frac{4 W c^2 (1-\varepsilon^2)^2}{\pi \mu \ell \varepsilon r \left\{ \left(\frac{16}{\pi^2} - 1\right) \varepsilon^2 + 1 \right\}^{1/2}} \qquad (3.67)$$

(W = ½ total rotor bearing system weight)

(ℓ = Journal length, r = Journal Radius)

Equation 3.67 was compatible with bearing assumptions made in Chapter 2 and applied to all rotor bearing system mass elements.* Cameron had also derived an expression for journal attitude angle, ϕ :

$$\phi = \tan^{-1}\left\{\frac{\pi}{4}\left(\frac{(1-\varepsilon^2)^{1/2}}{\varepsilon}\right)\right\} \qquad (3.68)$$

* Constant speed assumed in Chapter 2.

Since both left and right journals (Figure 3.2 - Rotor Bearing System Model) were physically identical and since their angular velocities were also equal, ϵ and ϕ were expected to be identical for both journals, i.e., symmetry should prescribe identical behavior for both journals. For verification, however, angular velocity was defined for each journal.

As in any time dependent simulation, initial conditions were prescribed. These were defined in terms of an assumed journal eccentricity ratio, ϵ , and attitude angle, ϕ -- the same values at both bearings. Disc initial circumferential position was assumed equal to that of both journals. Since equations 3.67 and 3.68 were defined for steady running only*, the initial value for ϕ did not satisy equation 3.68. Otherwise, mass displacement and, therefore, potential system instability could not be observed. Instead, steady running conditions were defined separately and differently with respect to these initial conditions.

Steady running conditions were defined in terms of an assumed eccentricity ratio and corresponding journal angular velocity (equation 3.67) and attitude angle (equation 3.68). Steady journal positions, therefore, were based upon: (1) static deflection due to rotor weight and (2) angular displacement (ϕ) due to journal interaction with bearing fluid. Steady running disc position was assumed equal to that of both journals. Steady bearing film forces added in the line of centers direction (Figure 3.1). The vector sum of these forces equaled rotor bearing system weight. Steady running conditions, in effect, established a temporary coordinate reference frame (Figure 3.6). With

* Rotor operation without displacement of mass element centroids.

steady conditions defined, computer simulation could begin by applying different initial conditions.

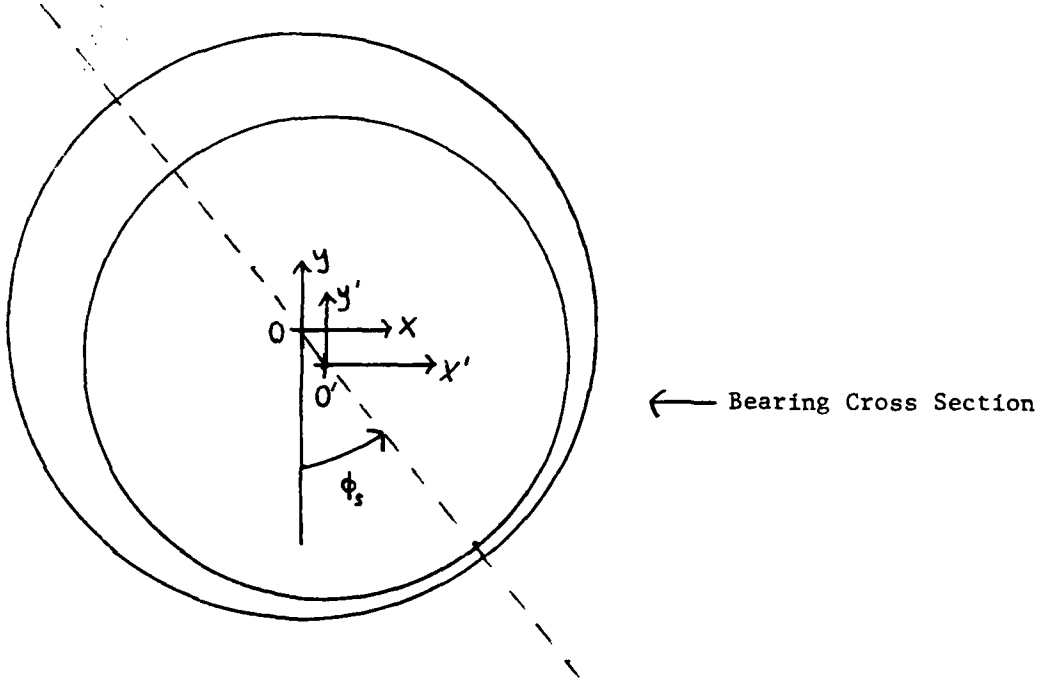

Figure 3.6 - Fixed Inertial and Steady Running (x', y') Coordinate Reference Frames

Simulation commenced with 4th order Runge Kutta finite difference integration of equations 3.23 and 3.24. State variable increments were calculated for an assumed time step (Δt) and added to previous values to yield state variable values at time, $t = t_0 + n\Delta t$. Bearing force equations 3.5 appeared twice, embodied with equations 3.66 -- once for each journal. These equations were first calculated using

ε and ϕ state variables converted to a $\tau = t\omega$ integration basis:

$$\varepsilon' = \left(\frac{\Delta\varepsilon}{\Delta t}\right)\left(\frac{1}{\omega}\right) \tag{3.69a}$$

$$\phi' = \left(\frac{\Delta\phi}{\Delta t}\right)\left(\frac{1}{\omega}\right) \tag{3.69b}$$

ε' and ϕ' were later multiplied by ω to allow finite difference time integration -- a Runge Kutta requirement! Bearing force equations 3.6 appeared next, again, once for each journal. Steady bearing film forces were subtracted from each bearing force (equations 3.6) -- necessary when force increments due to transient loading were being calculated. Rotor bearing system state variable equations 3.23 and 3.24, therefore, contained state variable and bearing force values relative to a particular steady running position (Figure 3.6).

Model accuracy tests were performed by setting steady running conditions that were just above and below (2 simulations) the stability threshold predicted by Shapiro and Colsher [1] . This was accomplished by prescribing steady running eccentricity ratios such that ω in equation 3.67 was less than 93 rev/sec for one simulation and greater than 93 rev/sec for the other. Different initial conditions were applied and time dependent state variable values were monitored using a simple plot routine.*

* MINIPLT--See Mechanical Engineering Dept. Computer Files.

To be compatible with Shapiro and Colsher, testing below the stability threshold should yield slightly damped state variable response. Testing above the stability threshold should yield ever increasing (exploding) state variable values with time.

3.D.1.B Linear Model Programming (RWE4)

As mentioned earlier, linear modeling was intended to produce eigenvalues and eigenvectors. Subjecting the A matrix of equation 3.34 to the QRHMOD routine accomplished this task. QRHMOD was available by calling METAPE or DYNSYS which appeared on Mechanical Engineering Department computer file tapes.

To prepare equation 3.34 for QRHMOD, several preliminary calculations were performed. Beaman's [13] linearized bearing coefficients (equations 3.25) were calculated and converted to x-y reference frame form (equations 3.28). Since linear analysis deals only with infinitessimal state variable variations from a steady running position, equations 3.67 and 3.68 were used to describe rotor speed (ω) and attitude angle (ϕ) respectively, for an assumed eccentricity ratio (ε). As before, ε values for both left and right journals were assumed identical. This routine was used for further comparison with Shapiro and Colsher's results and to obtain performance data for the isolated rotor bearing system.

Since labyrinth seal effects were the focus of this thesis and since changing the physical parameters of Myrick's rotor bearing system nullified comparison of results, performance data, here, were restricted

to rotor speed variation. This was best accomplished by iterating eccentricity ratio from about ϵ = .5 (ω= 45.8 rad/sec) to about ϵ = .005 (ω = 8745 rad/sec).

3.D.2 Labyrinth Seal Testing

This section discusses linear labyrinth seal model programming separately and in the context of coupling to the rotor bearing system linear model program (RWE4). Although explanation of isolated seal and disc programming appears to be a logical next step in this discussion, this programming is actually more conveniently accomplished by modifying the coupled system program. Therefore, coupled system programming will be discussed first.

3.D.2.A. Linear Model Programming - Coupled Labyrinth Seal and Rotor Bearing System (RWE4S)

The ultimate intent of linear model programming was to subject the A matrix of equation 3.65 to the QRHMOD routine. Since this A matrix contained the unaltered rotor bearing system A matrix of equation 3.34 in its upper left corner, expression of seal equation 3.60 coefficients and their proper placement within equation 3.65 were accomplished.

To do this, several intermediate tasks were performed. Initially, nominal (steady) chamber pressure (P_n) was established. This was accomplished by first assuming a Mach number at seal strip A (M_{An}) and then solving for P_n using equation 3.70. This pressure (equation 3.70) was then used to calculate the nominal discharge coefficient at

$$P_{n3.70} = \frac{P_A}{\left(1 + \left(\frac{k-1}{2}\right) M_{An}^2\right)^{1/k}} \tag{3.70}$$

seal strip A (C_{WAn} - equation 3.49c) and chamber pressure. A Mach number at seal strip B (M_{Bn}) was calculated using equation B.24 Chamber pressure was recalculated using equation 3.71. $P_{n3.71}$ was compared with

$$P_{n3.71} = \frac{A_{An}\ C_{WAn}\ M_{An}}{A_{Bn}\ C_{WBn}\ M_{Bn}} \left\{ \frac{\left(1 + \left(\frac{k-1}{2}\right) M_{Bn}^2\right)}{\left(1 + \left(\frac{k-1}{2}\right) M_{An}^2\right)} \right\}^{\frac{k+1}{2(k-1)}} \tag{3.71}$$

$P_{n3.70}$. If they differed by more than .0005x$P_{n3.70}$, then M_{An} was incremented accordingly and the process was repeated until both P_n values satisfied equation 3.72.* Since seal strips had been assumed to act only

$$P_{n3.70}(1-.0005) \leq P_{n3.71} \leq P_{n3.70}(1+.0005) \tag{3.72}$$

as converging nozzles both Mach numbers could not exceed 1.0. Mach numbers were also made greater than zero to avoid trivial solutions, i.e.:

$$0 < M \leq 1 \tag{3.73}$$

Once P_n was established, the axial flow coefficients in

*.0005 factor chosen to provide 3 digit accuracy

equations 3.50 could be calculated. Nominal circumferential seal fluid velocity (u_n) was determined from equation 3.36. Since steady running disc position had been assumed to be concentric within the seal, nominal disc to seal base clearance (h_n) was constant for all simulations. All that remained was to describe the coefficients in equation 3.60 and arrange them together with rotor bearing system coefficients per equation 3.65.

3.D.2.B. Linear Model Programming-Isolated Seal and Disc (RWE4P)

With the coupled system A matrix of equation 3.65 completely programmed, modifications for isolated seal and disc tests were then described. All that was necessary was to replace the coupled system A matrix with the seal PC matrix, consisting of the 4x4 lower right corner of equation 3.65. In order to properly reset this matrix between simulations, it was filled with zeros. The calculation routines within QRHMOD made this necessary whenever parameter variations required repeated use of QRHMOD.

3.D.3. Parameter Variations

In order to fully understand labyrinth seal and rotor bearing system interaction, certain seal and disc parameters were varied separately. Corresponding linear model programs, both isolated and coupled (RWE4P and RWE4S), were used. Generally, straight seal geometry (a=b) applied.

Disc Speed (ω) variation was accomplished by iterating eccentricity ratio (ε) as in RWE4. Variation of seal chamber axial length (ℓ) was more restrictive, however, since too narrow a seal chamber

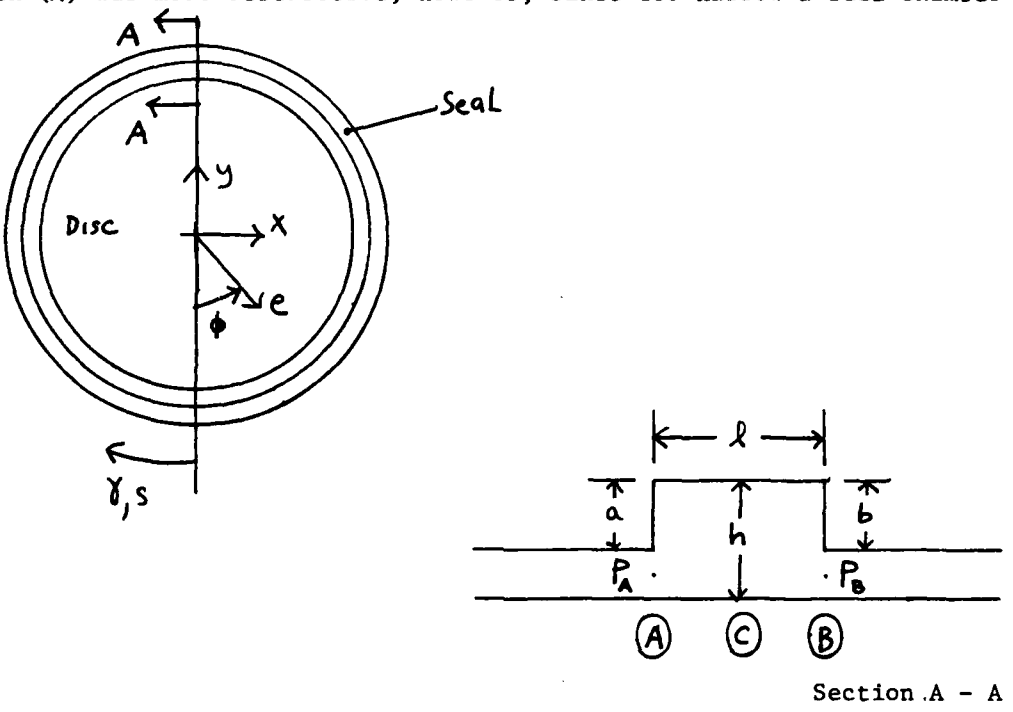

Figure 3.7 - Isolated Labyrinth Seal Surrounding Rotor Bearing System Disc

would violate the Chapter 2 assumption requiring complete axial kinetic energy destruction within the seal chamber. To determine this transition point, ℓ was incremented upward starting at ℓ=.001 in. It did not exceed axial disc length prescribed by Myrick (1.423 in.).

Disc radius was also incremented. Seal diameter was assumed to

increase accordingly such that h, a, and b remained constant. Since Shapiro and Colsher's analysis of Myrick's system also assumed point masses at bearing and disc stations, enlarging the disc did not affect comparison with this thesis' results provided that mass values remained unchanged.

Nominal disc to seal base clearance (h_n) was next to be individually varied. The upper limit for this parameter was expected to be very restrictive because, beyond a certain h value, complete kinetic energy destruction within the seal could not be assured.

Upstream pressure (P_A) variation was next. Both the upper and lower limits for this parameter were expected to be sensitive. The upper limit was prescribed by choked flow at seal strip B. The lower limit was restricted by assumed constant seal exit pressure (P_B). i.e., Should P_A become too small, unrealistic flow reversal would occur. As with ℓ and h_n variations, these limits were determined through analysis of a complete range of upstream pressures.

Finally, a and b seal strip heights were varied together to achieve variable seal convergence ($a > b$) and divergence ($a < b$). For comparability, average axial flow area was maintained. i.e., An increase in the "a" dimension was offset by a decrease in "b" (Figure 3.7). To establish the stabilizing nature of a divergent seal, another speed variation exercise was accomplished for an extreme divergent seal geometry. To maximize stability threshold increase, P_A was set to provide choked flow at seal strip B. Straight, divergent, and convergent seal geometry simulations were also conducted with exit pressure set at one atmosphere (14.7 psi). These simulations indicated whether or not this model is suited for testing at higher ambient pressures -- a useful

feature when developing high pressure turbine seal design criteria.

Chapter 4 RESULTS

4.A Overview

This chapter will present and discuss data produced from Chapter 3 simulations. For every simulation, parameter values will be listed followed by a graphical generalization of the data and observations of system behavior trends.

Nonlinear rotor bearing system (RW5) results discussion will be first and briefest because of its limited value to the purpose of this thesis. Linear rotor bearing system (RWE4) results discussions will follow and are limited to comparison with Shapiro and Colsher's speed variation results. Isolated seal and disc linear modeling (RWE4P) results will be next. Here, system behavior observations will take the form of discussions of trends exhibited by this system while several parameters are individually varied. The coupled rotor bearing and labyrinth seal model (RWE4S) results will be similarly discussed. Some attention will be focused upon seal and rotor bearing systems interaction. Such discussion provides qualitative understanding only. Ultimately, coupled system model speed will be increased with the seal at extreme divergence in an effort to prove stability threshold increase.

Table 4.1

Nonlinear Rotor Bearing System Parameter Values

Constant Parameters

$k_x = k_y = 5348.6$ lbf/in.	= Shaft Stiffness
$m_{JL} = m_{JR} = .0096$ lbf sec^2/in.	= Journal Mass
$m_d = .0875$ lbf sec^2/in.	= Disc Mass
W = 20.625 lbf	= ½ Rotor Bearing System Weight
ℓ = 1.603 in.	= Journal Length
r = 1.081 in.	= Journal Radius
c = .003 in.	= Bearing to Journal Radial Clearance
$\Delta t = 10^{-5}$ sec	= Time Step

Variable Parameters

Simulation 1: ω = 86	rev/sec,	ε_i = .08,	ε_j = .0797
Simulation 2: ω = 98.3	rev/sec,	ε_i = .078,	ε_j = .07
Simulation 3: ω = 92.87	rev/sec,	ε_i = .09	ε_j = .074

4.B Rotor Bearing System

4.B.1. Nonlinear Modeling (RW5) Results

As mentioned in Chapter 3, nonlinear rotor bearing system simulations were intended only as a modeling accuracy check. Such verification was best accomplished by operating this nonlinear model at or near Myrick's stability threshold.

Simulation 1 was conducted below Myrick's stability threshold of 93 rev/sec. Damped half frequency whirl was observed (see Figure

4.1). Angular velocities for both journals were observed to be identical for this and all other simulations.

Simulation 2 was conducted above Myrick's stability threshold. Explosive half frequency whirl was observed. (see Figure 4.2).

Simulation 3 was conducted very close to Myrick's stability threshold. Half frequency whirl was observed. However, neither damped nor explosive whirl could be confirmed (see Figure 4.3). Therefore, mass precession approaching a limit cycle at steady state was assumed. This condition establishes 92.87 rev/sec as at, or very close to, the system stability threshold. Because of inaccuracies inherent in visual graph sighting, a limited number of operating cycles and computer calculations this result was not expected to compare exactly with Myrick's.

Additionally, lengthy simulation time makes more accurate definition of this stability threshold, using iterative simulations, unwarranted. Therefore, simulation 3 provided practical confirmation of Shapiro and Colsher's stability threshold calculation.

4.B.2. Linear Modeling (RWE4) Results

Linear rotor bearing system simulation results are a bit more extensive with respect to nonlinear results. In addition to a stability threshold comparison, model frequency versus rotor speed and some mode shapes must also be compared with the results of Shapiro and Colsher.

These results identify 4 primary modes for Myrick's system. (see Figure 4.5a) Mode 1 is most susceptible to self excited whirl. It is characterized by mass displacement due to both rotor bending and rigid

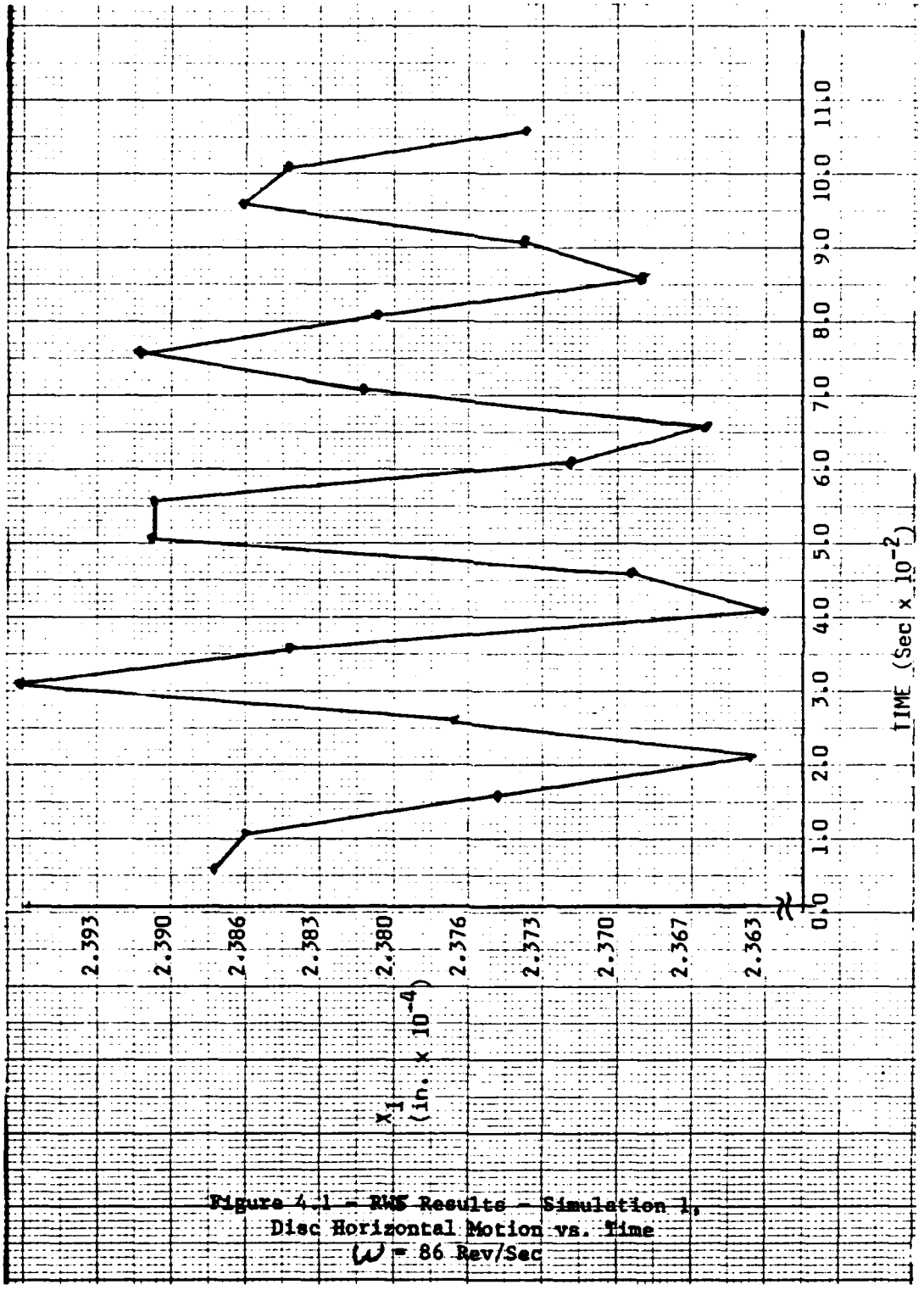

Figure 4.1 - RWS Results - Simulation 1,
Disc Horizontal Motion vs. Time
ω = 86 Rev/Sec

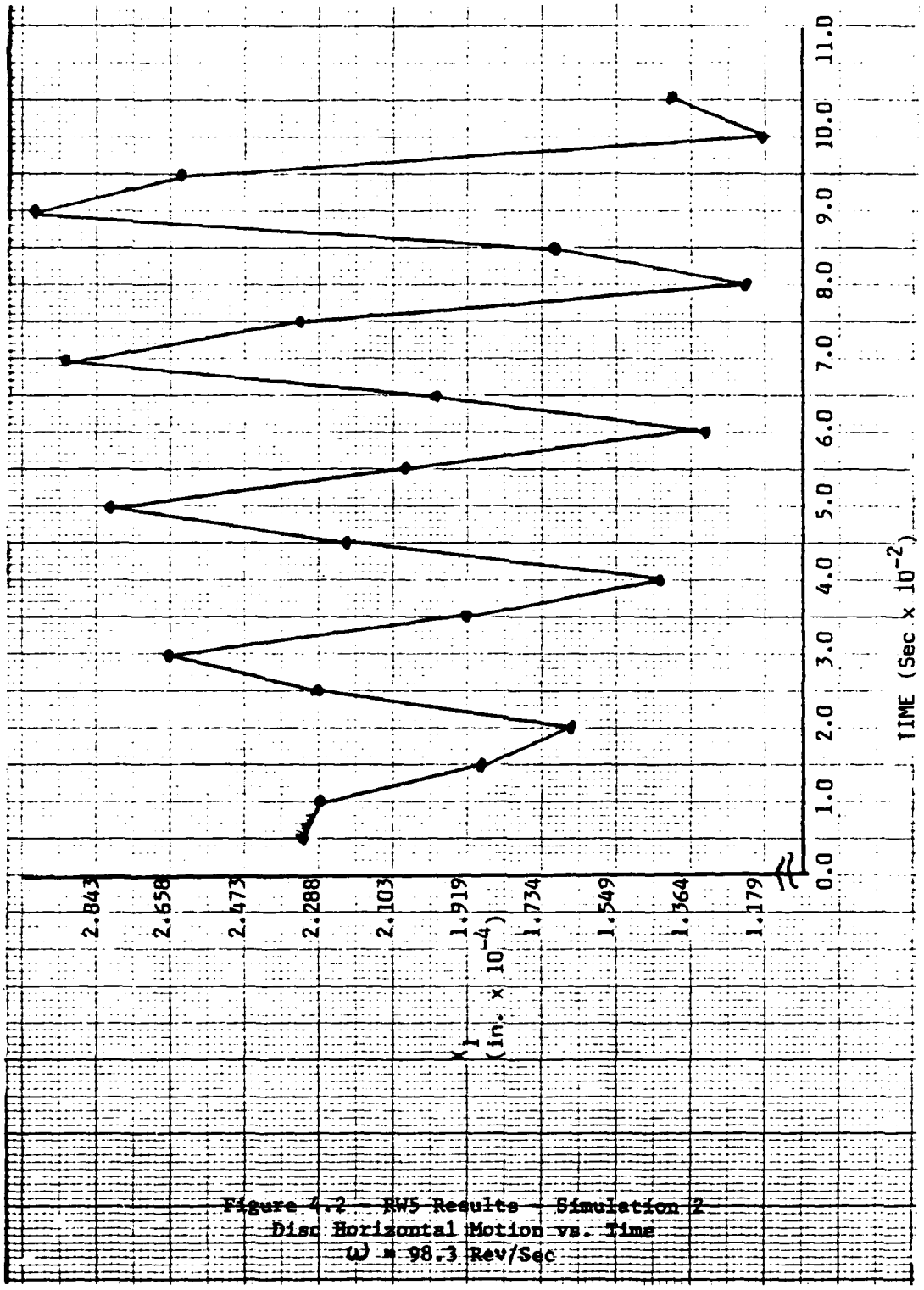

Figure 4.2 — RW5 Results — Simulation 2
Disc Horizontal Motion vs. Time
ω = 98.3 Rev/Sec

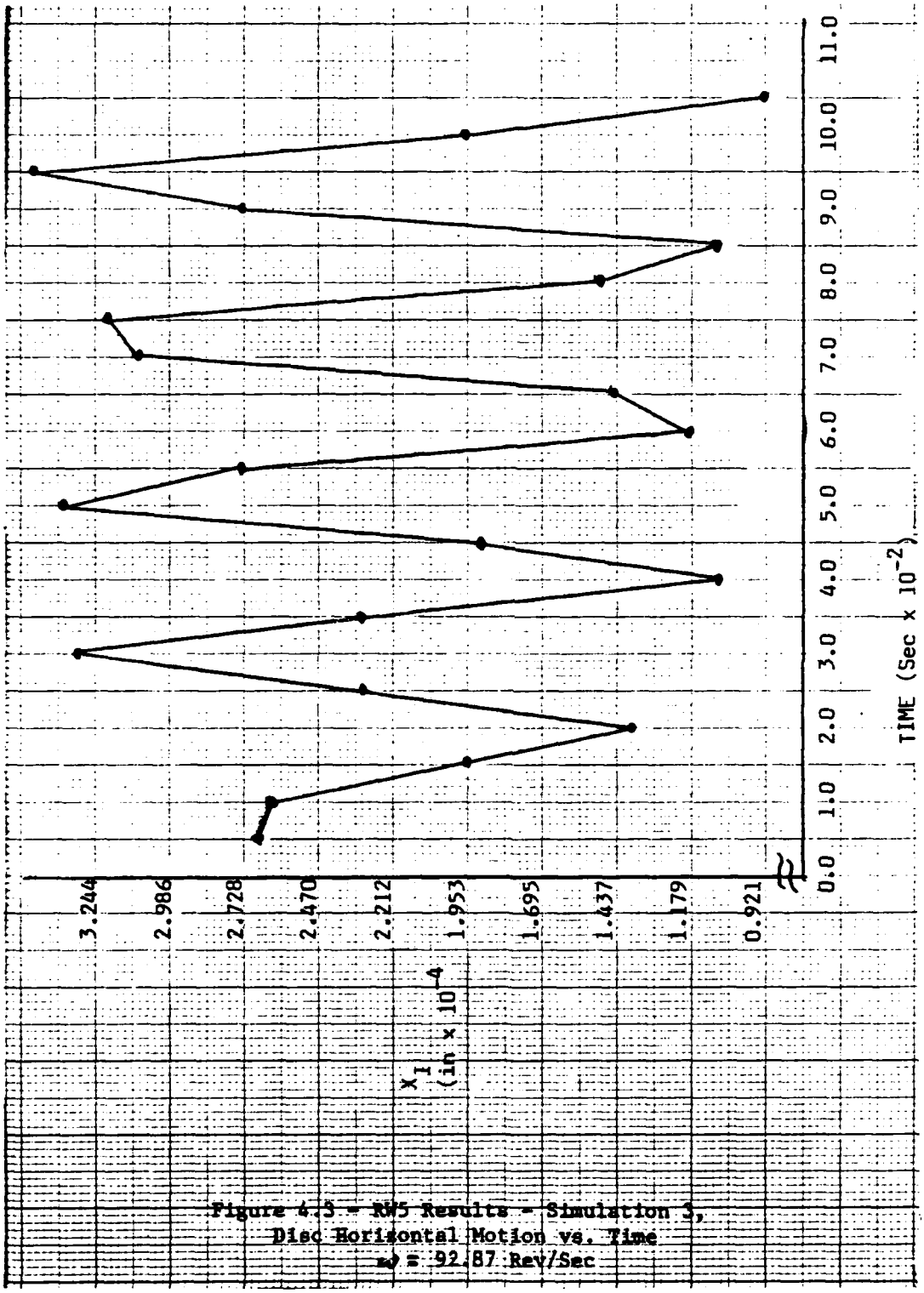

Figure 4.5 - RW5 Results - Simulation 3,
Disc Horizontal Motion vs. Time
ω = 92.87 Rev/Sec

body translation. Mode 2 is least susceptible to any excitation source. It is characterized by rigid body motion because of relatively large journal displacements since it is affected predominantly by bearing coefficient changes. Mode 3 is most susceptible to mass unbalance, but only marginally affected by Oil Whip as suggested by a relatively large disc displacement. Mode 4 is well damped and is characterized by a combination of rotor bending and translation.

Rotor speed variation revealed a stability threshold of 92.58 rev/sec (see Figure 4.4). This was indicated by a near zero eigenvalue real part for Mode 1. It does not differ appreciably from the nonlinear model result of 92.87 rev/sec. Both results are not completely accurate. Linear model accuracy required a Mode 1 eigenvalue real part of exactly zero and nonlinear accuracy required a large number of cycles of operation. However, since they both compare resonably with Shapiro and Colsher, RW5 and RWE4 accuracies are acceptable.

Comparing modal frequency vs rotor speed, RWE4 results and those of Shapiro and Colsher are in general agreement. Figure 4.4a closely duplicates their plot (Figure 4.4b). Per Shapiro and Colsher, a critical speed for Modes 3 and 4 occurs at a rotor speed of 55 rev/sec. RWE4 results indicate a similar critical speed near 55.6 rev/sec. Both graphs show a Mode 1 and 2 intersection at their respective stability thresholds (93 and 92.58 rev/sec). Mode 1 "growth factors" (eigenvalue real parts) are also reasonably similar.

Mode shape comparisons are not as close as were previous comparisons (Figure 4.5). RWE4 rotor speeds cannot be precisely matched to those of Shapiro and Colsher because of the requirement to increment rotor speed by adjusting eccentricity ratio (equation 3.67). However,

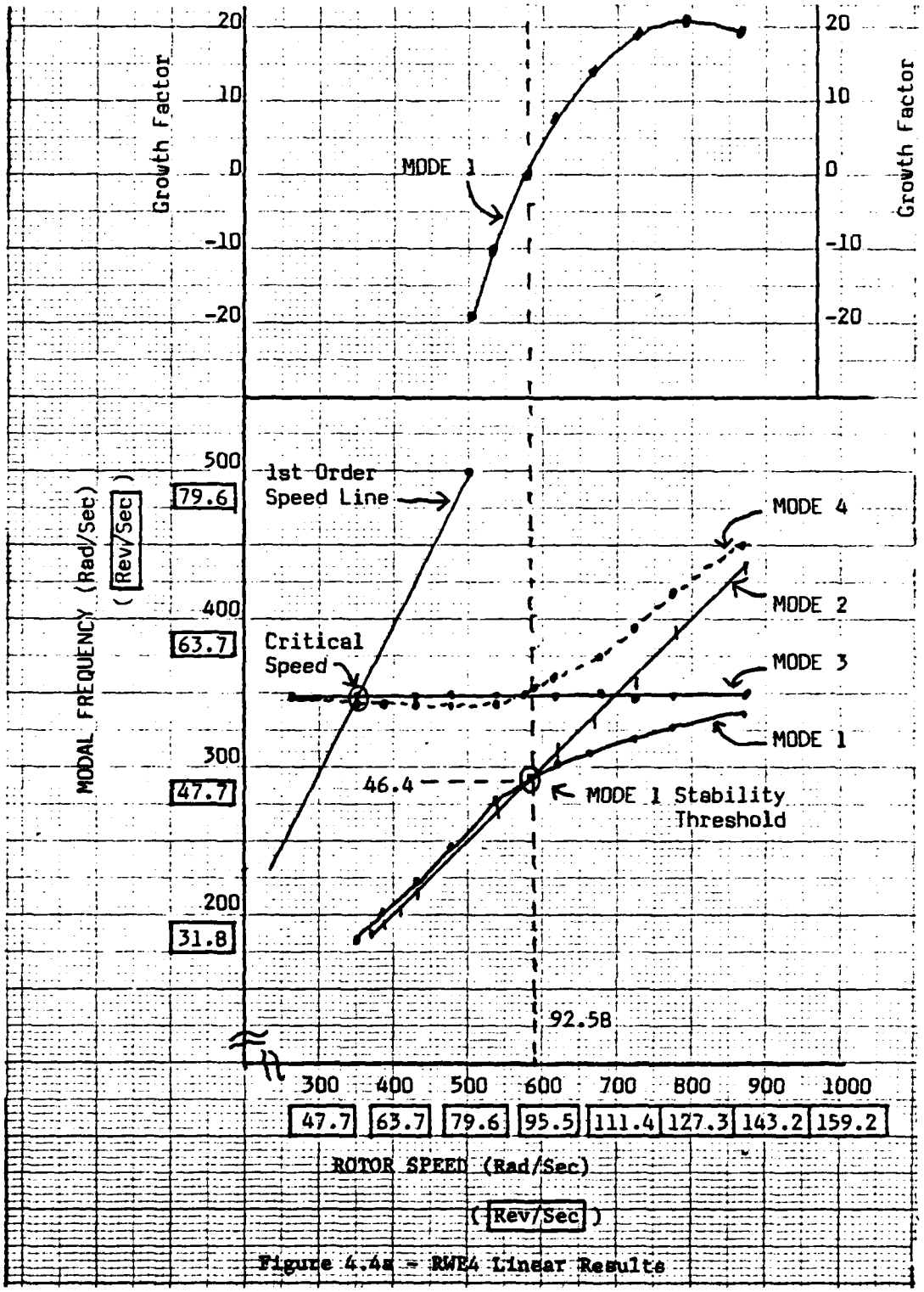

Figure 4.4a - RWE4 Linear Results

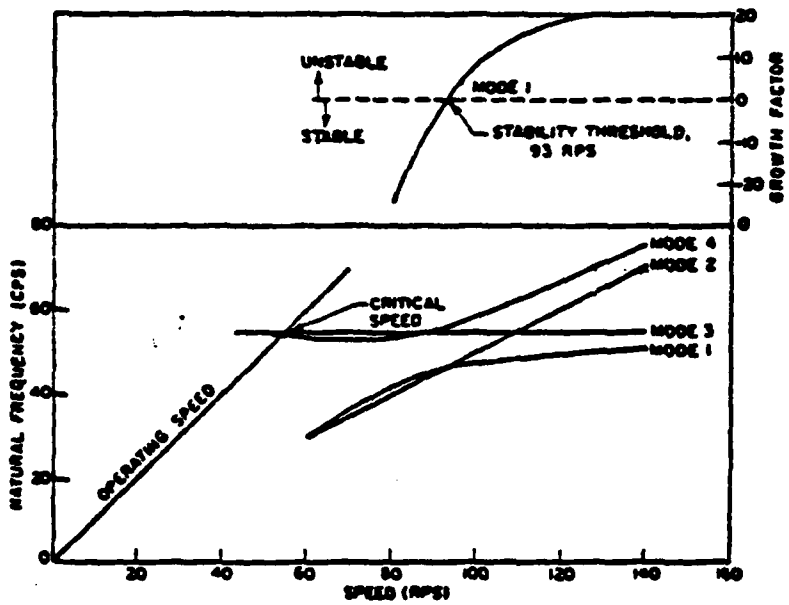

Figure 4.4b - Shapiro & Colsher [1] Linear Results

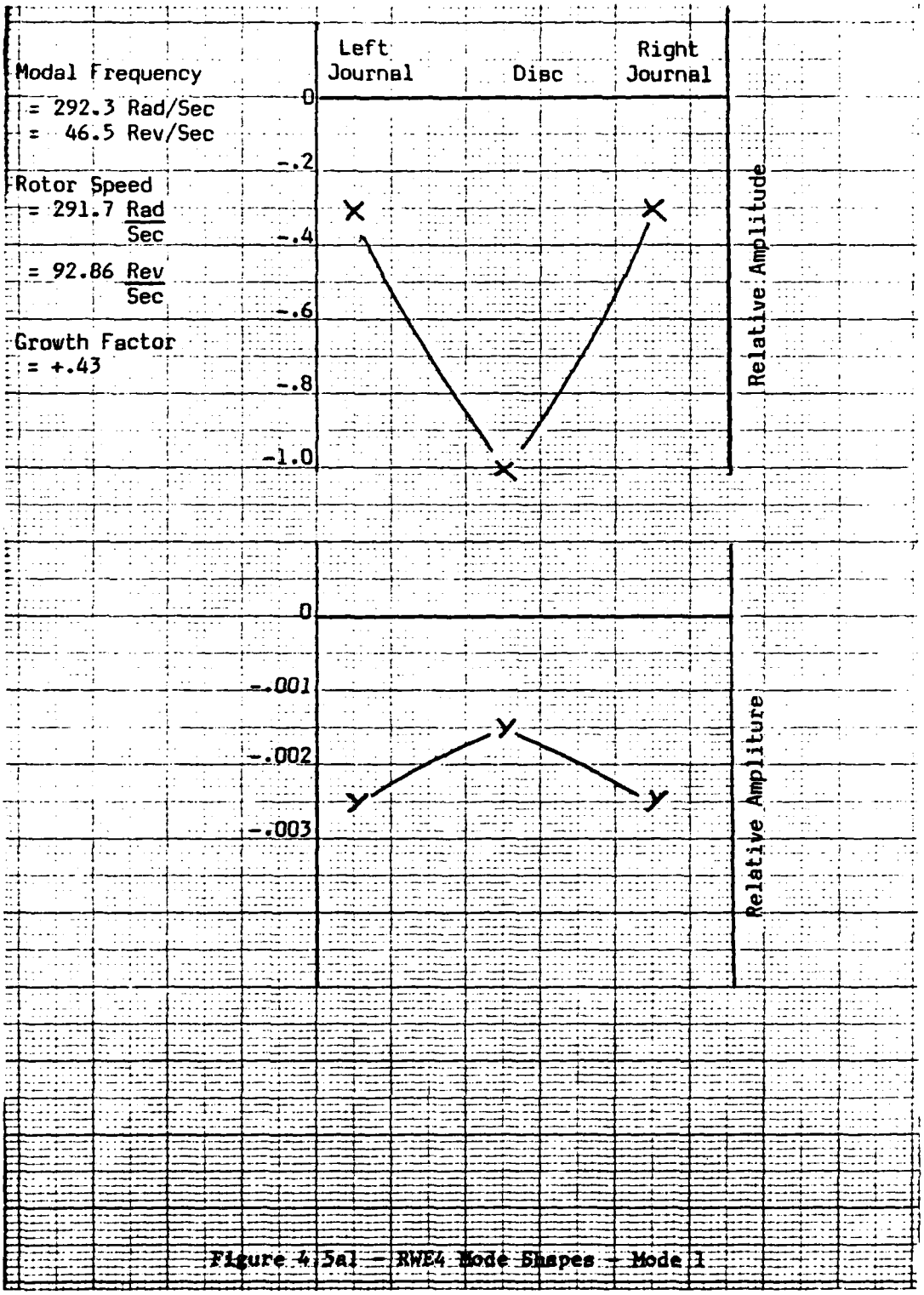

Figure 4.5a1 — RWE4 Mode Shapes — Mode 1

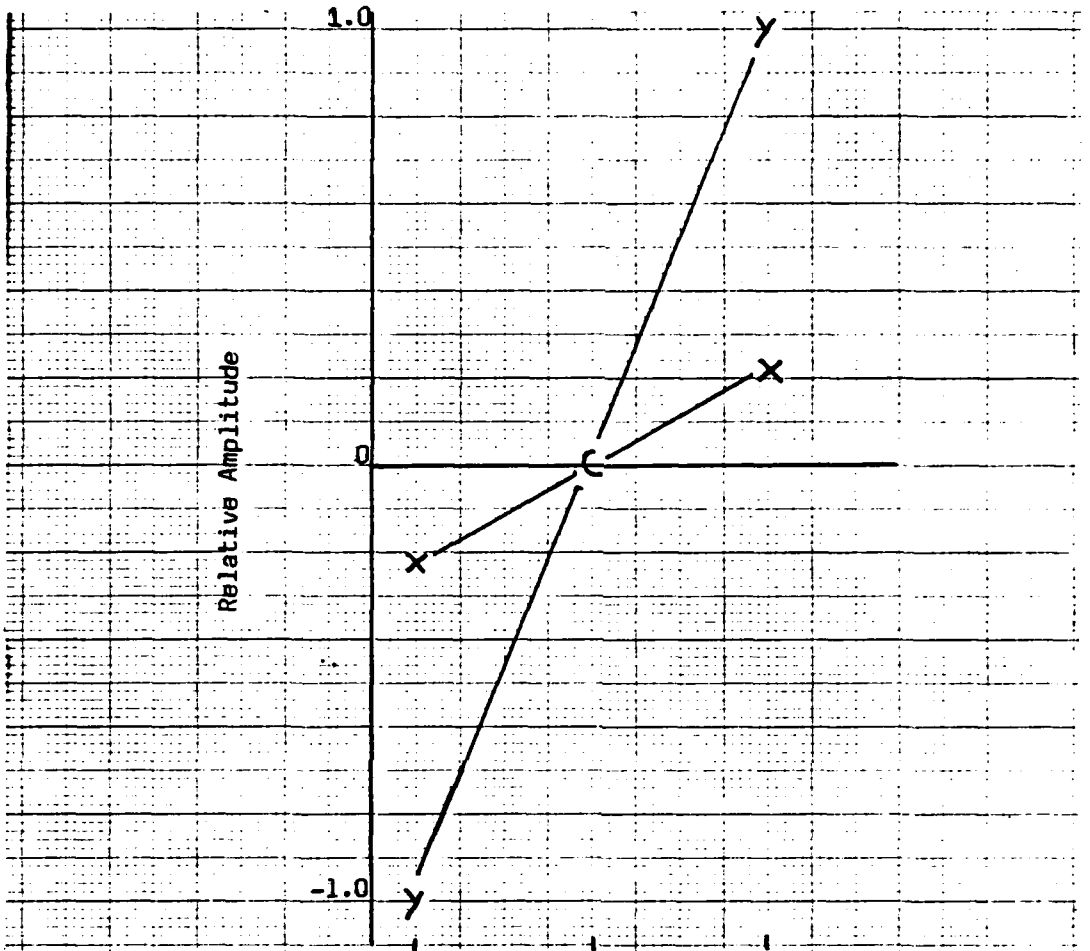

Modal Frequency = 253.7 Rad/Sec
= 40.38 Rev/Sec
Rotor Speed = 503.47 Rad/Sec
= 80.13 Rev/Sec
Growth Factor = -56.18

Figure 4.3a2 - RWE4 Mode Shapes - Mode 2

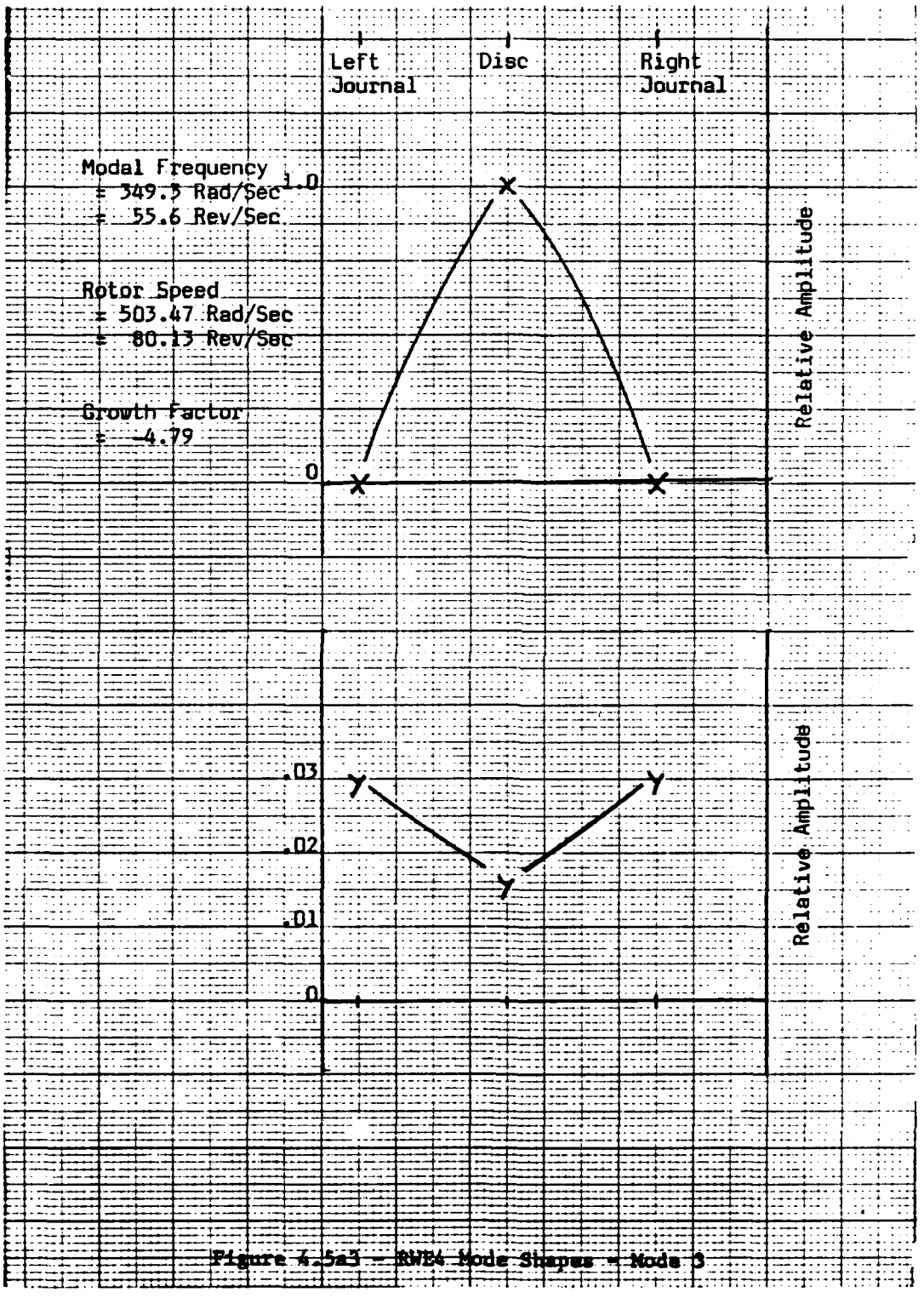

Figure 4.5a3 – RWE4 Mode Shapes – Mode 3

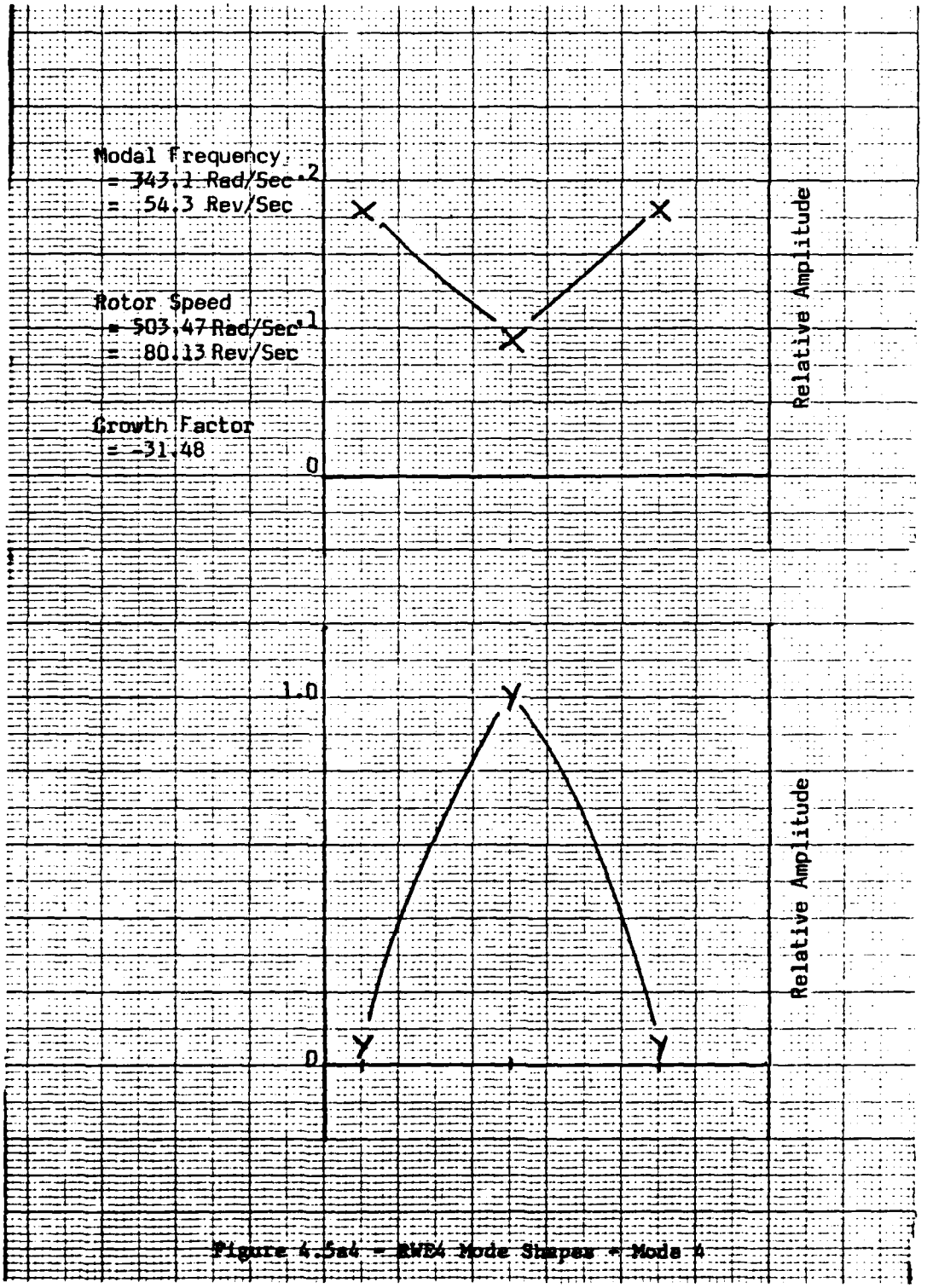

Figure 4.5a4 - RWB4 Mode Shapes - Mode 4

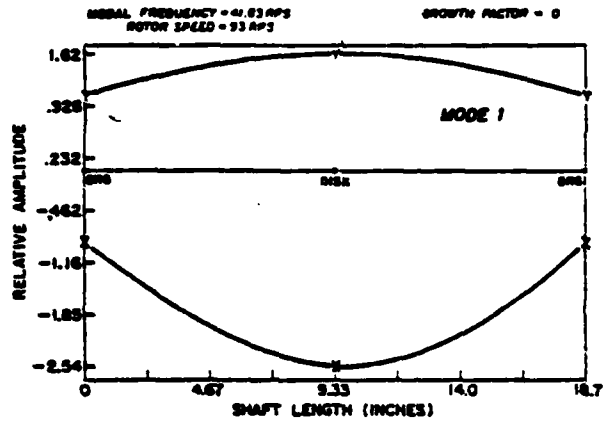

Figure 4.5b1 - Mode 1

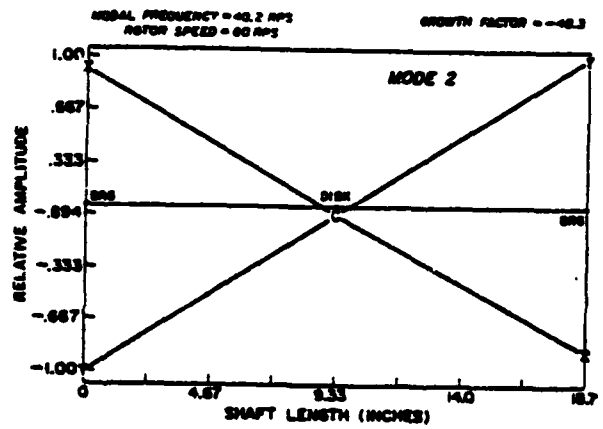

Figure 4.5b2 - Mode 2

Figure 4.5b - Shapiro and Colsher Mode Shapes [1]

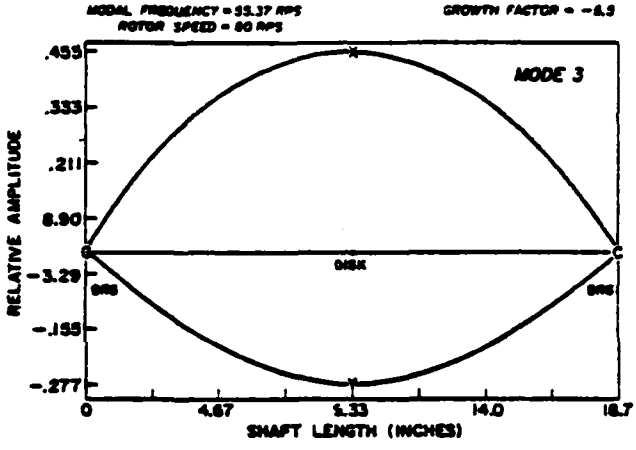

Figure 4.5b3 - Mode 3

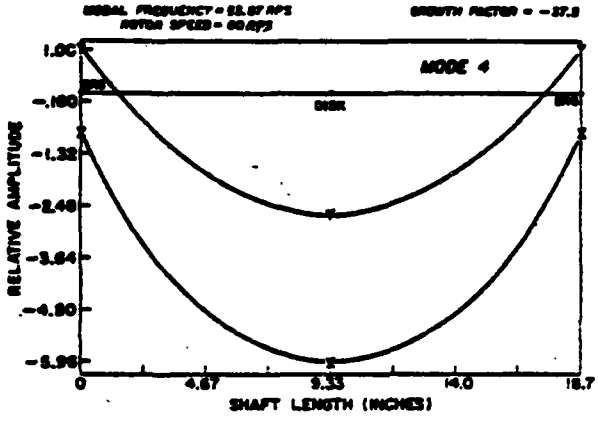

Figure 4.5b4 - Mode 4

Figure 4.5b - Shapiro and Colsher [1] Mode Shapes

general modal characteristics are similar. Modes 1 and 3 compare closest with Shapiro and Colsher. Their shapes and relative displacements are similar. Mode 2 shapes compare in that they both reflect rigid rotor behavior.

Considering the astonishing similarity between modal frequency vs rotor speed plots, these Mode 2 differences might be attributed to phase changes occuring between 80 and 80.13 rev/sec for this mode. Mode 4's shape is most radically different from that of Shapiro and Colsher. But, since modal frequencies and growth factors are similar, these mode shape differences might also be attributed to phase differences caused by non-precise speed duplication. Generally, therefore, this rotor bearing system model practically resembles Myrick's system (Figure 1.8).

4.C. Isolated Seal and Disc (RWE4P) - Results

4.C.1. Overview

This section will discuss results of parameter variations for the isolated and rigidly mounted seal and disc system. This system has only 2 modes because of such rigid seal and disc mounting. Consequently, these modes relate to flow behavior only. To identify each mode, isolating phenomena must be identified.

When fluid friction (K_{2p}, K_{2h}, and K_{2u} coefficients in equation 3.55) against disc and seal surfaces was eliminated, the "Axial" flow eigenvalue was practically unaffected, but, the "Circumferential" flow eigenvalue radically destablized (real part became positive) with little affect on modal frequency. Since friction within the seal affects

Table 4.2

Isolated Seal and Disc Nominal Parameter Values

Parameter	Program Coding		Value
ℓ = Seal Strip Separation	CLC		.1 in.
r = Disc Radius	RD		10.0 in.
P_A = Seal Inlet Pressure	PSI		2.55 psi
		(HP)	15.00 psi
P_B = Seal Exit Pressure	PSE		1.00 psi
		(HP)	14.70 psi
h_n = Nominal Seal Base to Disc Clearance	DC		.200 in.
ω = Disc Angular Velocity	PSDR		579.45 rad/sec
a = Height of Seal Strip A	A		.195 in.
b = Height of Seal Strip B	B		.195 in.

Table 4.3

Constant Seal Parameter Values

Parameter	Program Coding	Value
R = Gas Constant	R	247104 $in^2/sec^{2o}R$
k = Specific Heat Ratio	CK	1.4
T = Seal Fluid Temperature	TI	560^oR
μ = Dynamic Viscosity	DV	2.8×10^{-9} $lbfsec/in^2$

AD-A116 774 AIR FORCE INST OF TECH WRIGHT-PATTERSON AFB OH F/G 13/9
LABYRINTH SEAL EFFECTS ON ROTOR BEARING SYSTEM STABILITY.(U)
MAY 82 A J PAVELKO
UNCLASSIFIED AFIT/NR/82-10T NL

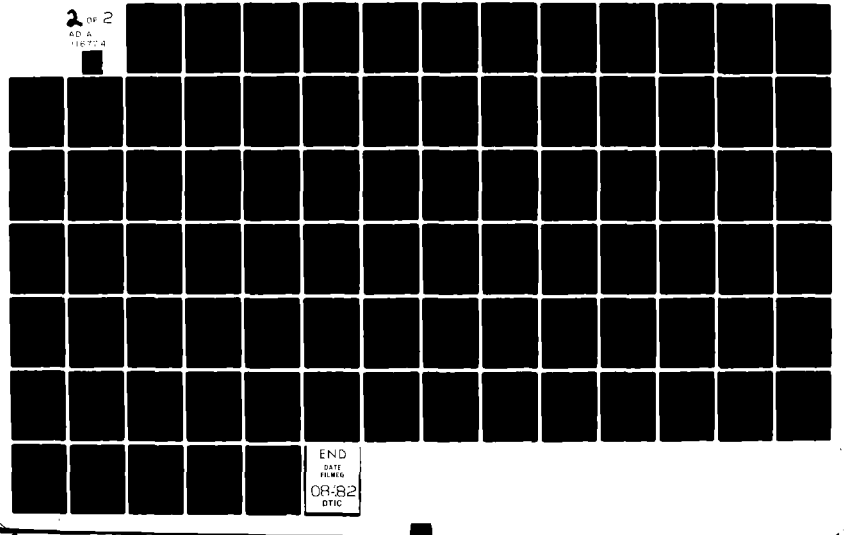

circumferential flow predominantly these modes have been labled "Axial" and "Circumferential" accordingly. The Axial mode is, generally, the more stable of these modes as this section's discussion will illustrate.

The parameter variations examined in this analysis are: (1) seal strip separation in the axial direction (ℓ in Figure 3.7), (2) disc radius (r), (3) upstream pressure (P_A), (4) disc to seal base nominal clearance (h_n), (5) disc rotational speed (ω), and (6) radial projections of seal strips toward the disc (a, b). Each of these parameters were varied individually leaving all others at nominal value (Table 4.2). These nominal values were selected to produce realistic results. The high pressure simulation (HP), by definition, involved different nominal pressures.

Nominal values in Table 4.2 were also chosen to resemble the seal used by Wright. The Myrick rotor bearing system disc radius was increased to provide stable operation with other nominal parameter values. Since disc mass and position were left unchanged rotor bearing system performance was not affected by this change.

Throughout this discussion, the terms "stabilize" and "destabilize" will be used to indicate the direction of change of eigenvalue position on a root locus plot as a parameter is incremented. A "stabilizing" trend is directed toward the left, "destablilizing" toward the right. "Stable" eigenvalues appear to the left of the imaginary axis. "Unstable" eigenvalues exist to the right of this axis.

4.C.2 Seal Strip Separation (ℓ) Variation

Figure 4.6 presents seal strip separation variation results.

For both Axial and Circumferential modes, stability decreases with increasing seal strip separation. This result appears to contradict the expectation* that increasing fluid to interacting surfaces friction with increasing seal surface area would be stabilizing. It should be noted, however, that once coupled to the rotor bearing system, this system will have 6 modes. A proper stability assessment must consider all modal reactions together.

Circumferential modal frequency decreases with increasing ℓ. This could represent declining circumferential fluid velocity as chamber widening makes this seal behave more like a subsonic diffuser by reducing velocity of subsonic circumferential flow. Corresponding Axial modal frequency increase suggests that increasing seal width provides increasing time and distance for acceleration (and deceleration) of axial flow. For any of these simulations, both seal modal frequencies add to equal disc rotational frequency (ω).

Such a consistent event suggests that disc rotational frequency is the "driving" frequency for this isolated seal and disc system. Since both seal and disc are rigidly mounted and seal pressure drop is constant only the Axial and Circumferential "degrees of freedom" are available to distribute disc momentum ($I_{Ad}\omega$). Should either modal frequency exceed the frequency of this sole momentum source, energy creation must have occurred. Obviously, such an event is unrealistic. Its computer predicted occurence for $\ell < .051$ in. suggests, possibly, that the assumption of complete kinetic energy dissipation within the seal chamber is invalid below this seal strip separation value.

* See Chapter 1.

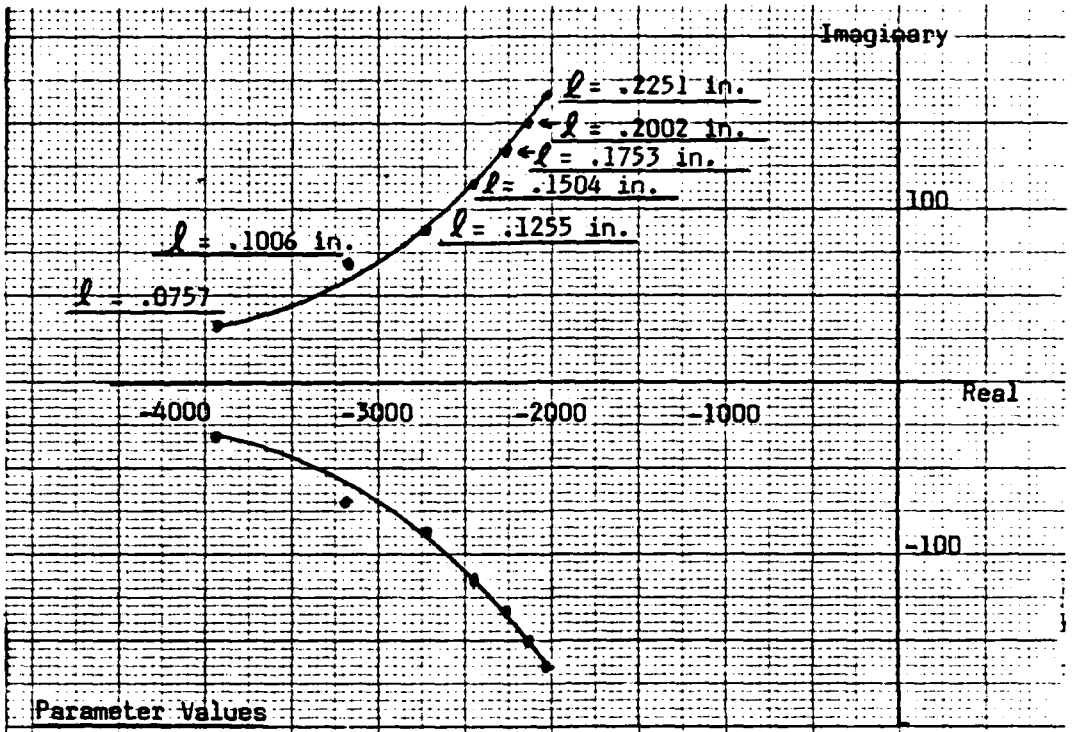

Parameter Values

P_A = 2.55 psi
P_B = 1.00 psi
M_A = .667
M_B = 1.00
a = .195 in } (Straight
b = .195 in } Seal)
h_n = .200 in
r = 10.0 in
ω = 579.45 Rad/Sec
= 92.22 Rev/Sec
$\Delta\ell$ = .0249 in

Lower Realistic Limit:
$\ell \approx .051$ in
where:
λ Axial = -5513 ± .419j

Figure 4.6a – RWE4P Results – Seal Strip Separation Variation, Eigenvalues – Axial Mode

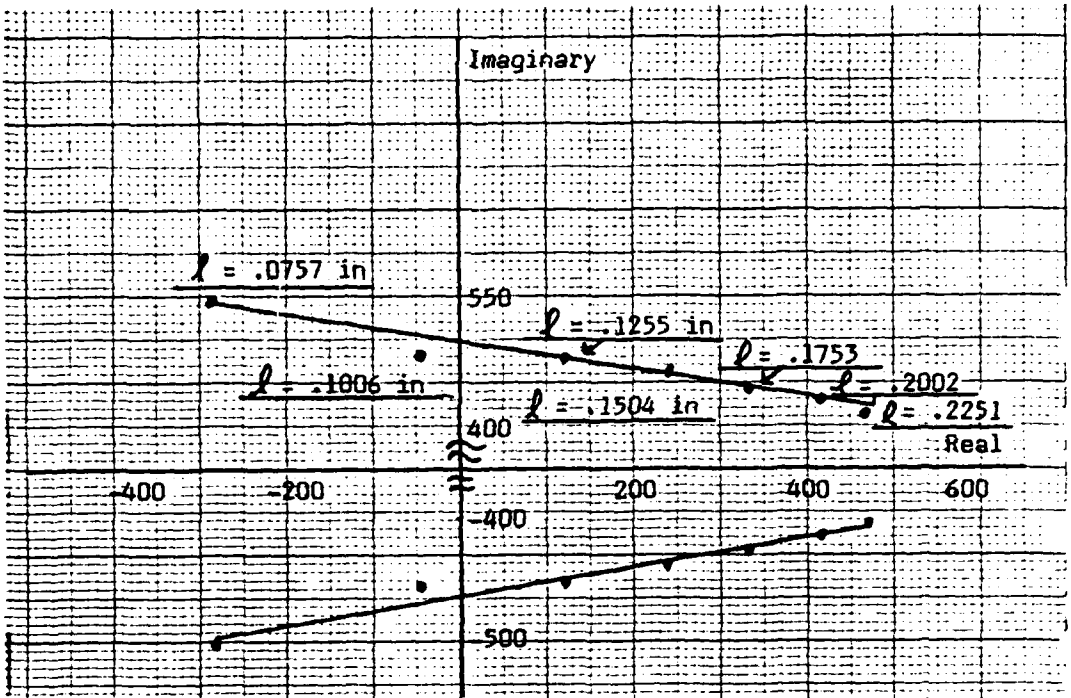

Parameter Values

P_A = 2.55 psi
P_B = 1.00 psi
M_A = .667
M_B = 1.000
a = .195 in
b = .195 in
h_n = .200 in
r = 10.0 in
ω = 579.45 Rad/Sec
= 92.22 Rev/Sec
$\Delta\ell$ = .0249 in

Lower Realistic Limit:

$\ell \simeq .051$ in

where:

$\lambda_{circ} = -684 \pm 579.9j$

Figure 4.6b - KWE4P Results - Seal Strip Separation Variation, Eigenvalues - Circumferential Mode

4.C.3 Disc Radius (r) Variation

Figure 4.7 presents the results of disc radius variation. With increasing disc radius, the Axial mode stabilizes while the Circumferential mode destabilizes. Since Circumferential mode stabilization occurs about the imaginary axis its affect on system stability is more important, i.e., increasing disc radius enhances seal stability.

As predicted earlier (Chapter 1), this stabilization can be attributed to increasing friction between fluid and adjoining surfaces. Because friction increases with both fluid velocity and interacting area -- both characteristics of increasing disc radius -- fluid flow through the seal should be stabilized.

Another expected characteristic of increasing r is increasing Circumferential modal frequency. Increasing circumferential fluid velocity is intuitively associated with increasing disc surface speed. Axial modal frequency must decrease because of increased axial flow area associated with increasing disc (and seal) radius. It is also physically conceivable that a gain in Circumferential modal frequency should offset a reduction in Axial modal frequency since transfer of fluid momentum involves corresponding changes in fluid velocity.*

* Each fluid particle has axial and circumferential velocity components. Therefore, "mass transfer" during such a "momentum transfer" (P = mv) does not occur.

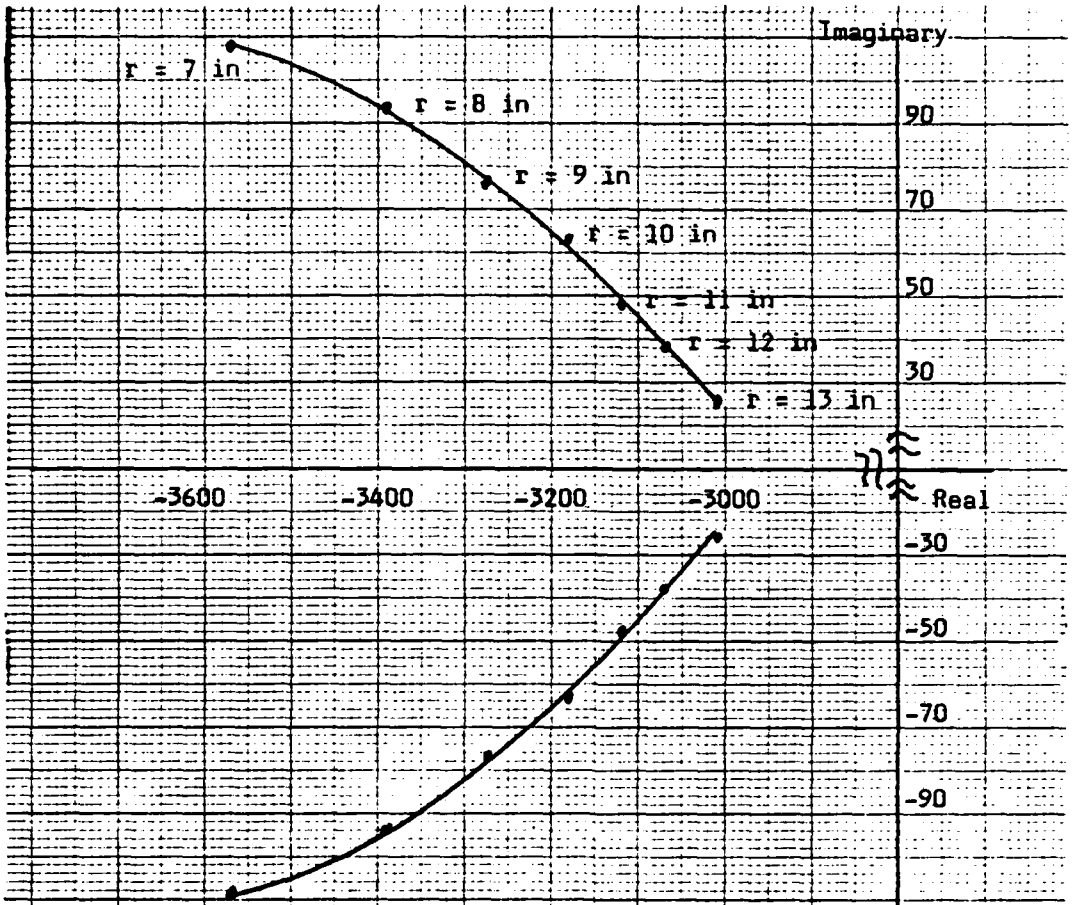

Parameter Values

P_A	= 2.55 psi	ω	= 579.45 Rad/Sec
P_B	= 1.00 psi		= 92.22 Rev/Sec
M_A	= .667	Δr	= 1.0 in
M_B	= 1.000		
a	= .195 in		
b	= .195 in		
h_n	= .200 in		
ℓ	= .100 in		

Figure 4.7a – RWE4P Results – Disc Radius Variation, Eigenvalues – Axial Mode

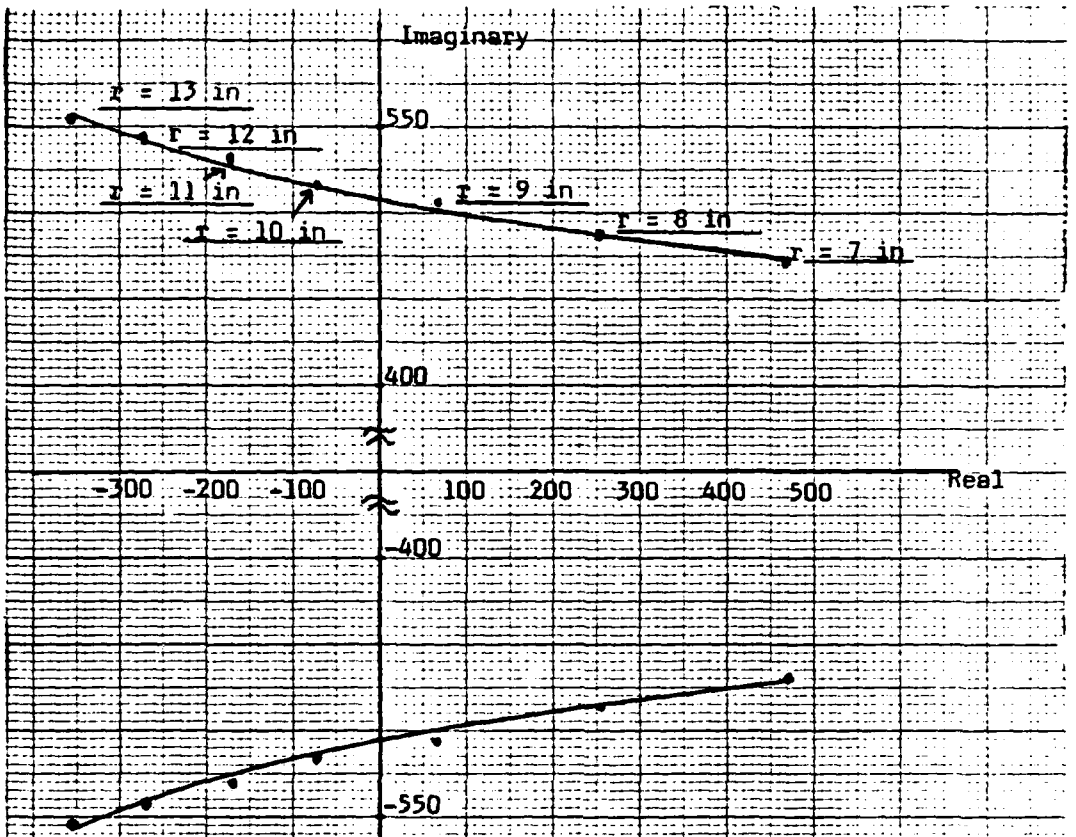

Parameter Values

P_A = 2.55 psi

P_B = 1.00 psi

M_A = .667

M_B = 1.000

a = .195 in

b = .195 in

h_n = .200 in

ρ = .100 in

ω = 579.45 Rad/Sec

= 92.22 Rev/Sec

Δr = 1.0 in

Figure 4.7b - RWE4P - Disc Radius Variation, Eigenvalues - Circumferential Mode

4.C.4 Upstream Pressure (P_A) Variation

Figure 4.8 presents upstream pressure variation results. Both Axial and Circumferential modes destabilize when P_A is increased. Increasing upstream pressure implies increasing force applied against seal and disc. Since both disc and seal are physically constrained only flow modes can react to this increasing force. Such a reaction should reflect reduced stability.

Unfortunately, actual destabilization (left to right crossing of imaginary axis) is not illustrated here. At P_A = 2.55 psi, flow through seal strip B (Figure 3.7) chokes. Further increase in P_A, until flow through seal strip A chokes, should destabilize the Circumferential Mode. In addition to this upper realistic limit, a lower realistic limit was also encountered.

Circumferential modal frequency exceeds disc rotational frequency when $P_A < 1.3108$ psi. As explained in 4.C.2, such a condition is unrealistic. This condition, possibly, corresponds to a reversal of flow direction thereby violating a system constraint -- $P_A > P_C$.

4.C.5. Disc to Seal Base Nominal Clearance (h_n) Variation

Figure 4.9 presents results of h_n variation simulations. Within realistic limits, both Axial and Circumferential modes are stabilized by increasing h_n. This result might be attributed to a reduced rate of change of chamber pressure. As h_n increases, axial fluid velocity and modal frequency decrease th ereby reducing rate of change of

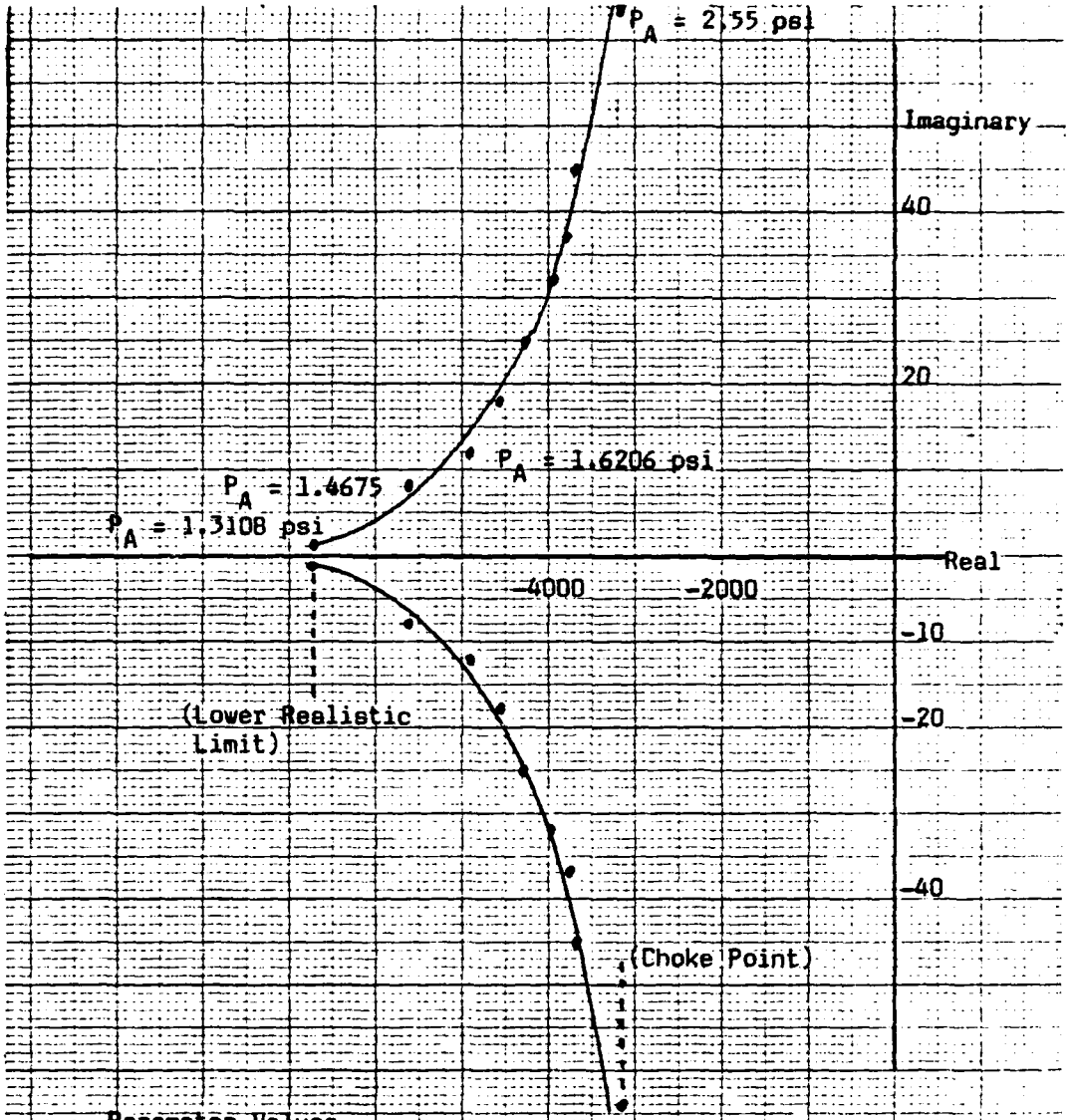

Parameter Values

ΔP_A	= .1549 psi		
P_B	= 1.000 psi	b	= .195 in
r	= 10.8 in	ℓ	= .100 in
h_n	= .200 in	ω	=579.45 Rad/Sec
a	= .195 in		= 92.22 Rev/Sec

Figure 4.8a - RWE4P Results - Seal Upstream Pressure Variation, Eigenvalues - Axial Mode

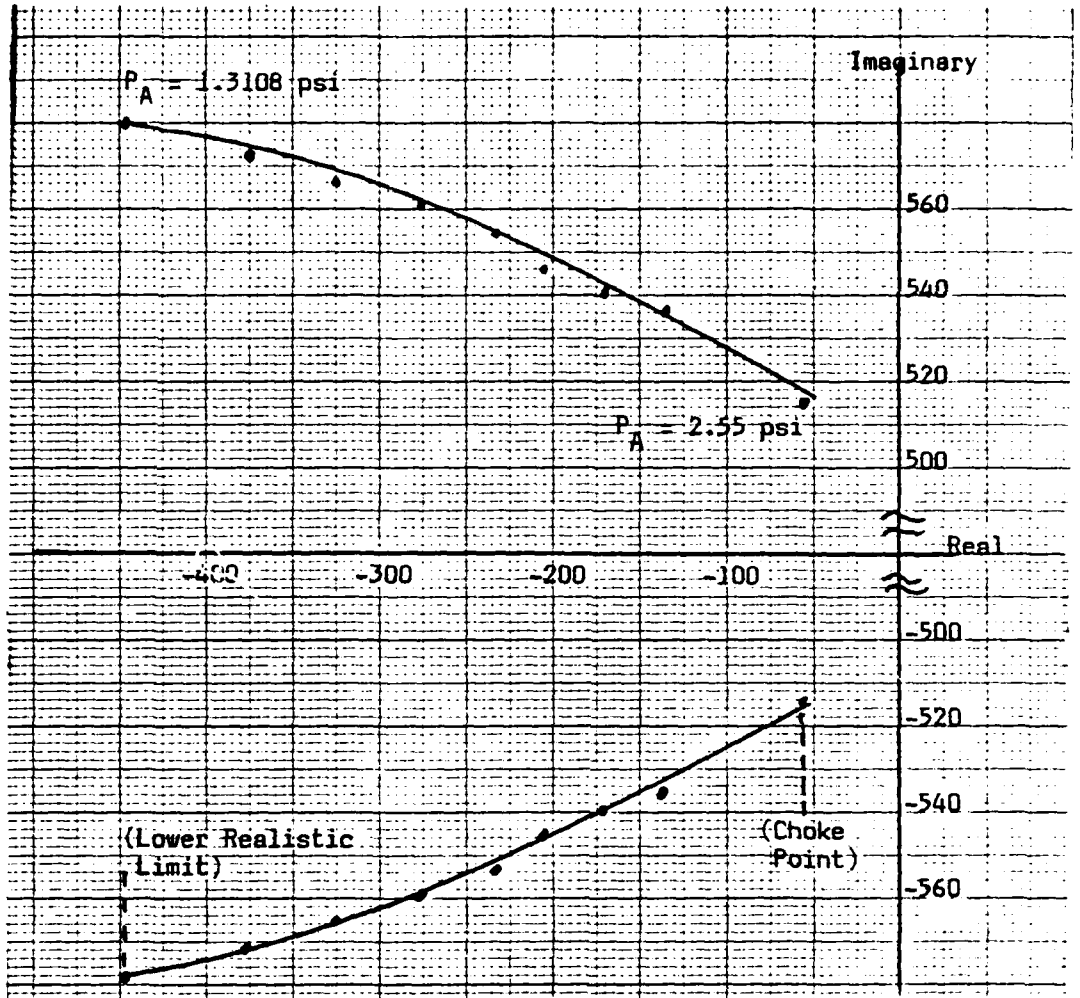

Parameter Values

ΔP_A = .1549 psi
P_B = 1.000 psi
r = 10.0 in
h_n = .200 in
a = .195 in
b = .195 in

ℓ = .100 in
ω = 579.45 Rad/Sec
= 92.22 Rev/Sec

Figure 4.8b - RWE4P Results - Seal Upstream Pressure Variation, Eigenvalues - Circumferential Mode

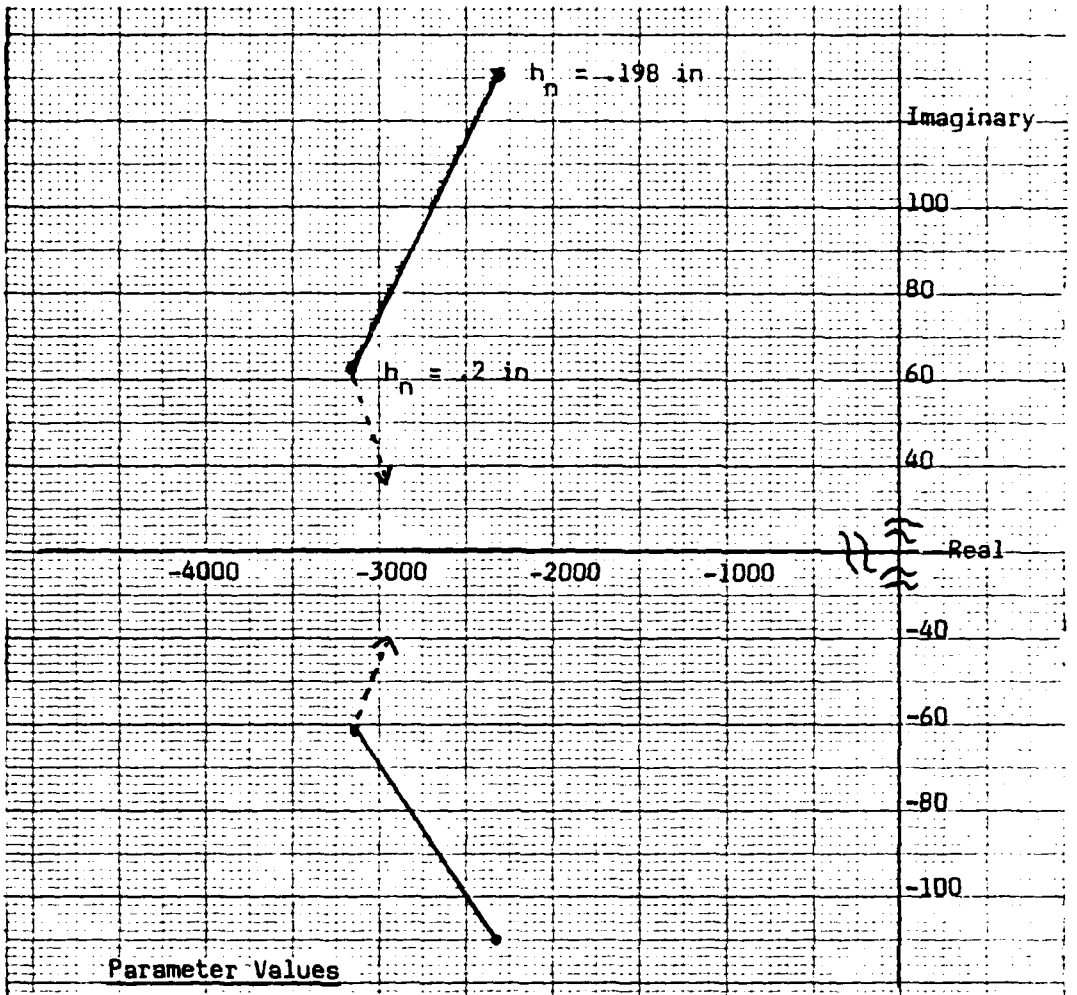

Parameter Values

(Upper Realistic Limit: $h_n \approx .27$ in)

P_A = 2.55 psi
P_B = 1.00 psi
r = 10.0 in
ℓ = .100 in
M_A = .667
M_B = 1.000

a = .195 in
b = .195 in
ω = 579.45 Rad/Sec
= 92.22 Rev/Sec

Figure 4.9a - RWT4P Results - Nominal Seal Strip Separation Variation, Eigenvalues - Axial Mode

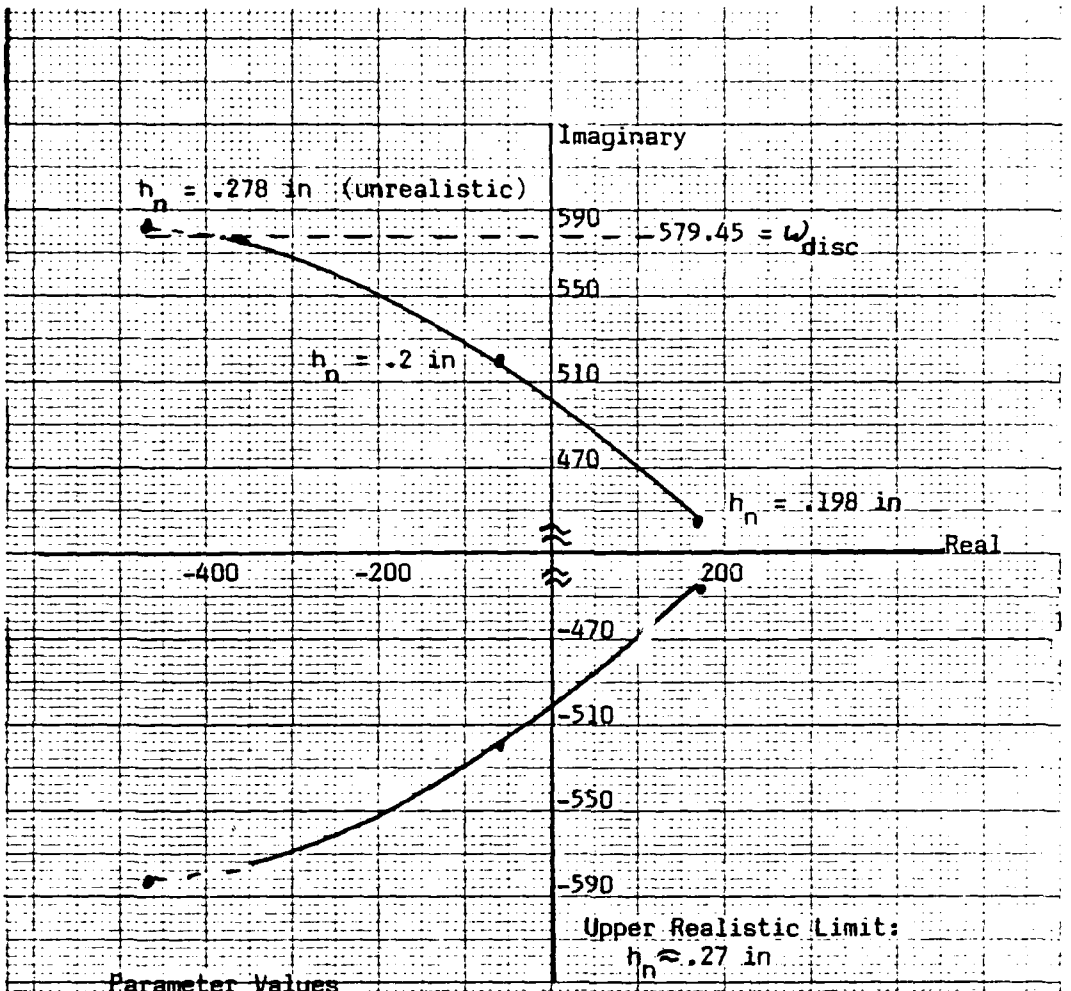

Parameter Values

P_A	= 2.55 psi	a = .195 in	
P_B	= 1.00 psi	b = .195 in	
r	= 10.0 in	ω = 579.45 Rad/Sec	
ℓ	= .100 in	= 92.22 Rev/Sec	
M_A	= .667		
M_B	= 1.000		

Figure 4.9b - RWE4P Results - Nominal Seal Strip Separation Variation, Eigenvalues - Circumferential Mode

chamber pressure (equation 3.51 - ζ_P coefficient).

This effect is valid between narrow limits only. The obvious lower limit is $h_n = a$ and/or $h_n = b$ resulting in complete cessation of flow. The upper limit is $h_n \approx .27$ in. (interpolated result). This limit corresponds to an unrealistic Circumferential modal frequency greater than ω. Consequently, this limit corresponds to a clearance so great that the assumption of complete kinetic energy destruction within the seal chamber is violated.

4.C.6. Disc Angular Velocity (ω) Variation

Figure 4.10 presents disc angular velocity variation results. Both Axial and Circumferential modes stabilize with increasing ω. This stabilization can, again, be attributed to increasing friction between seal fluid and interacting surfaces with increasing disc surface speed.

4.C.7. Seal Divergence ($a > b$) Variation

Figure 4.11 presents seal divergence variation results. Both seal modes are stabilized by increasing seal divergence. Decreasing nominal chamber pressure with increasing seal divergence suggests that greater exit with respect to inlet mass flow area, reducing chamber pressure, is responsible for this stabilizing trend.

4.C.8 Seal Convergence ($a < b$) Variation

Figure 4.12 presents seal convergence variation results. Seal

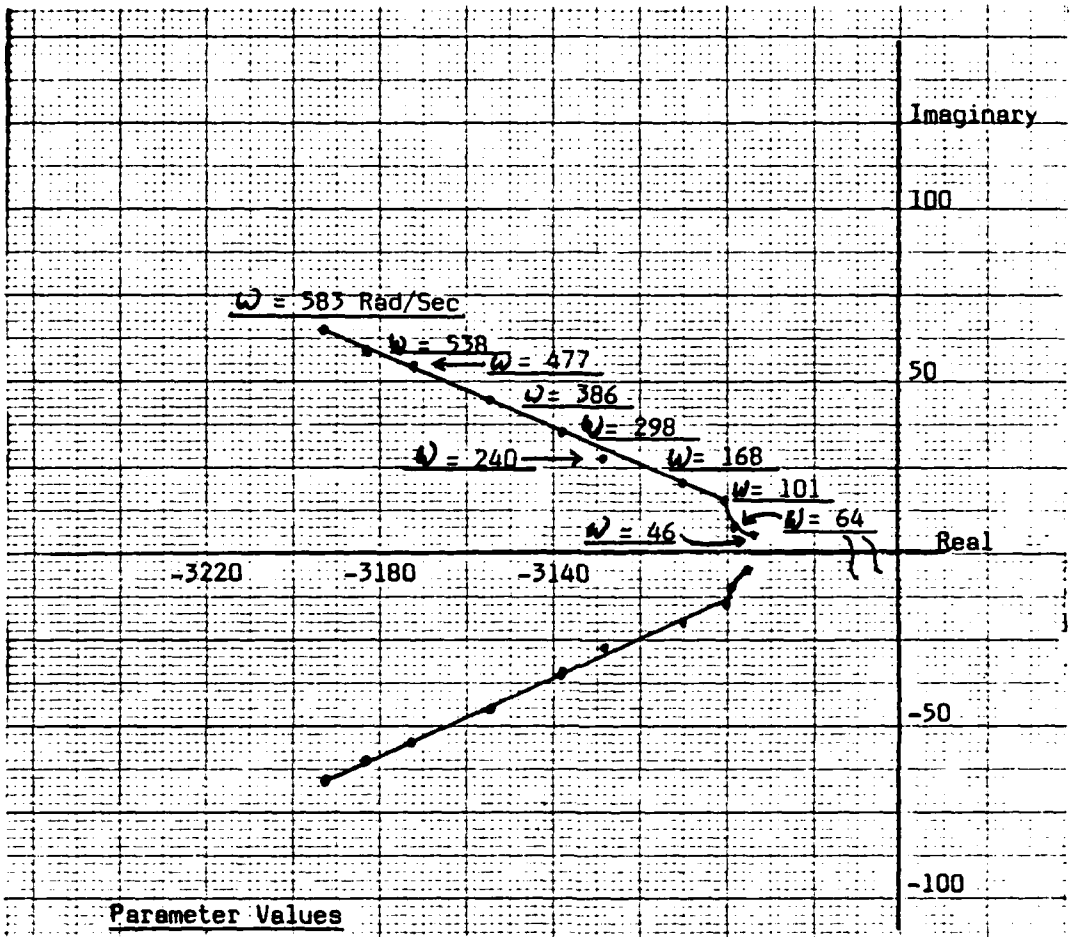

Parameter Values

P_A	=	2.55 psi	M_A	=	.667
P_B	=	1.00 psi	M_B	=	1.000
r_o	=	10.0 in			
ℓ	=	.100 in			
h_n	=	.200 in			
a	=	.195 in			
b	=	.195 in			

Figure 4.10a - RWE4P Results - Disc Speed Variation, Eigenvalues - Axial Mode

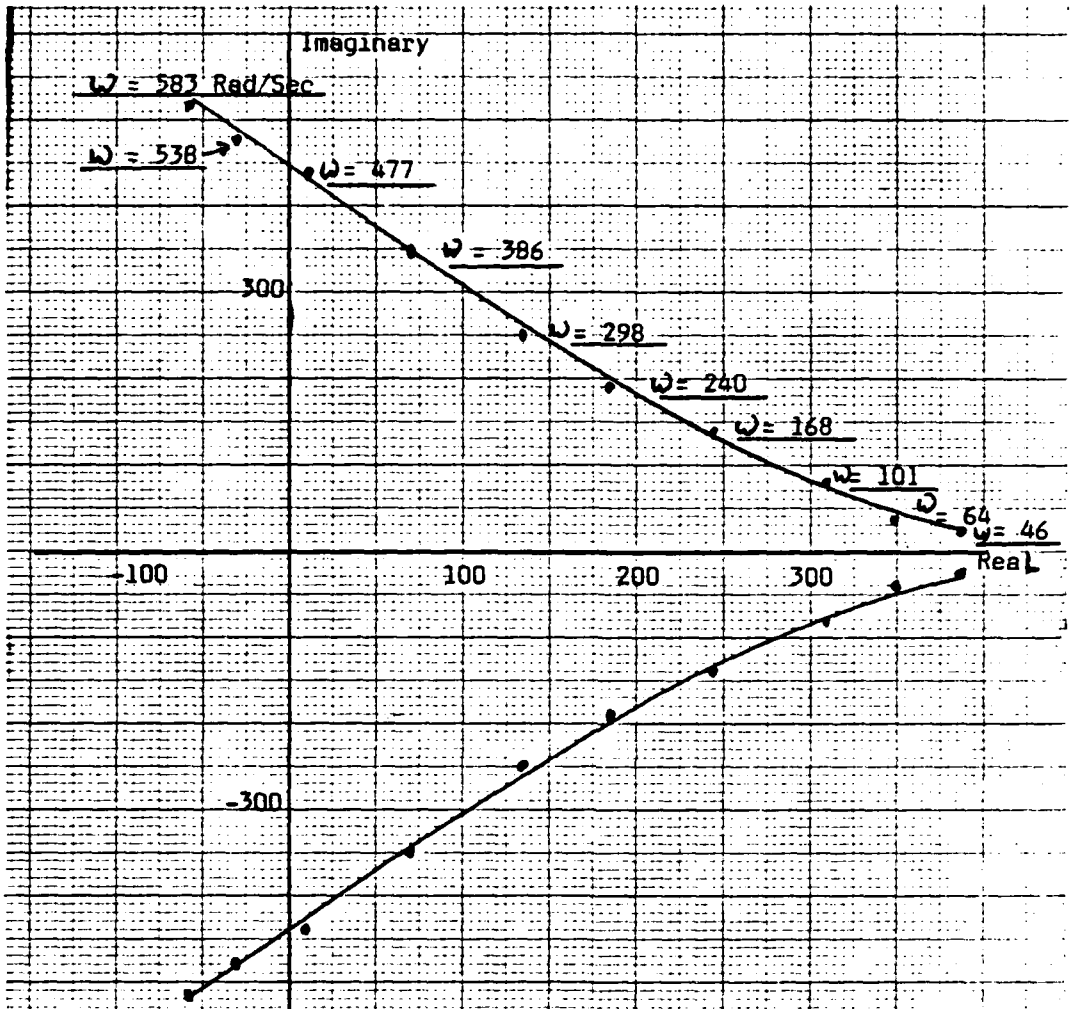

Parameter Values

P_A	=	2.55 psi	M_A	=	.667
P_B	=	1.00 psi	M_B	=	1.000
r	=	10.0 in			
ℓ	=	.100 in			
h_n	=	.200 in			
a	=	.195 in			
b	=	.195 in			

Figure 4.10b - RWE4P Results - Disc Speed Variation, Eigenvalues - Circumferential Mode

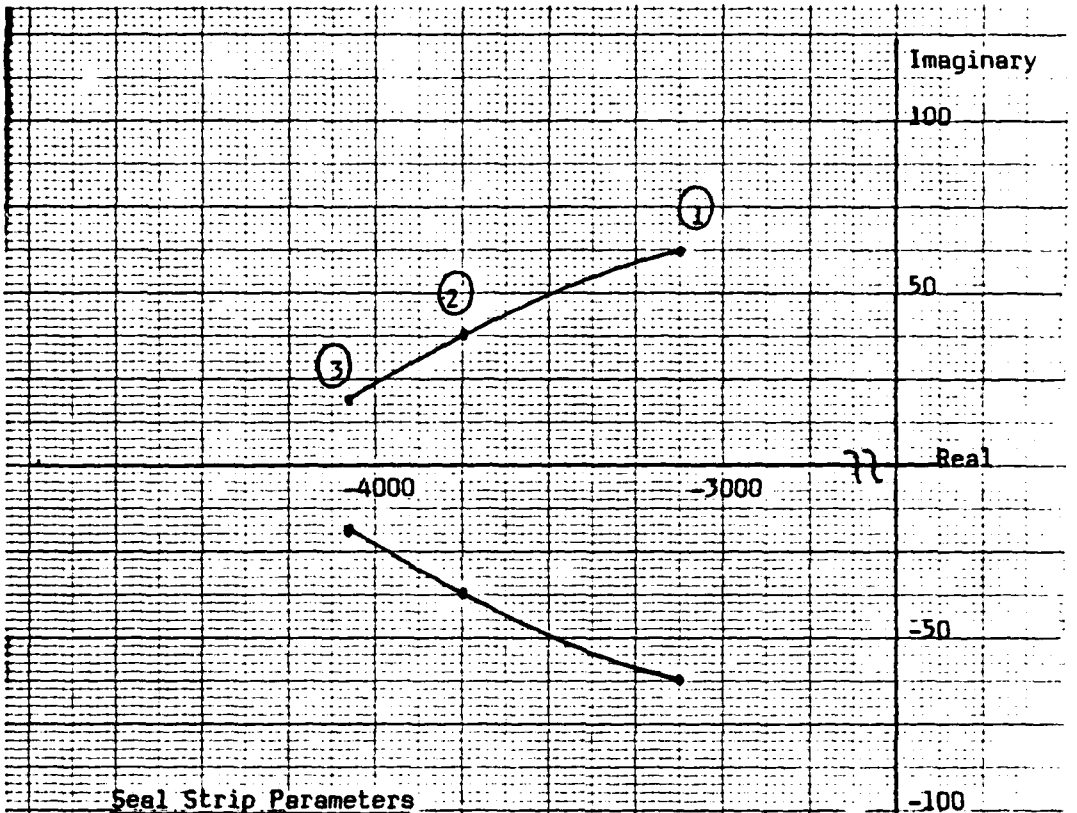

Seal Strip Parameters

(1) a = .195 in, b = .195 in, P_n = 1.89 psi,
M_A = .667 , M_B=1.000

(2) a = .196 in, b = .194 in, P_n = 1.69 psi,
M_A = .817 , M_B= .874

(3) a = .197 in, b = .193 in, P_n = 1.34 psi,
M_A =1.0 , M_B= .667

Nominal Values

P_A = 2.55 psi
P_B = 1.00 psi
h_n = .200 in
ℓ = .100 in

r = 10.0 in
ω = 579.45 Rad/Sec
= 92.22 Rev/Sec

Figure 4.11a - RWE4P Results - Seal Divergence Variation, Eigenvalues - Axial Mode

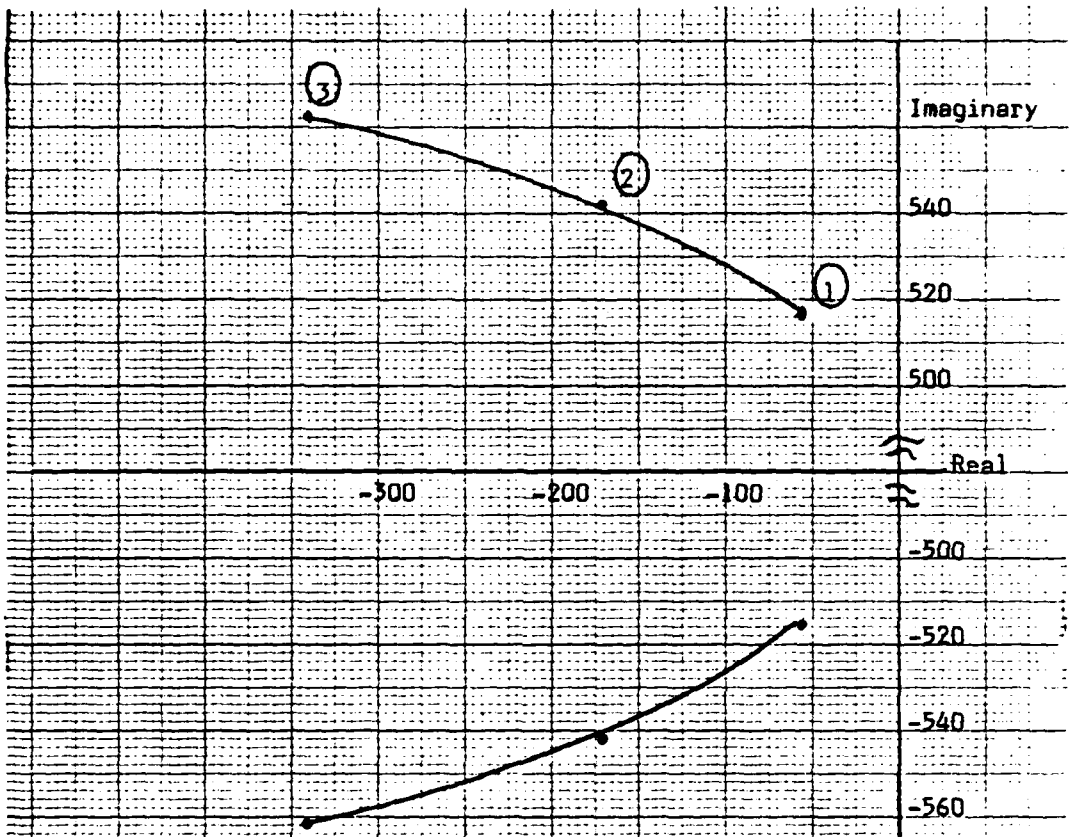

Seal Strip Parameters

(1) a = .195 in, b = .195 in, P_n = 1.89 psi
M_A = .667 , M_B=1.000

(2) a = .196 in, b = .194 in, P_n = 1.69 psi
M_A = .817 , M_B= .874

(3) a = .197 in, b = .193 in, P_n = 1.34 psi
M_A = 1.0 , M_B= .667

Nominal Values

P_A = 2.55 psi h_n = .200 in r = 10.0 in
P_B = 1.00 psi R = .100 in ω = 579.45 Rad/Sec

Figure 4.11b - RWE4P Results - Seal Divergence Variation, Eigenvalues - Circumferential Mode

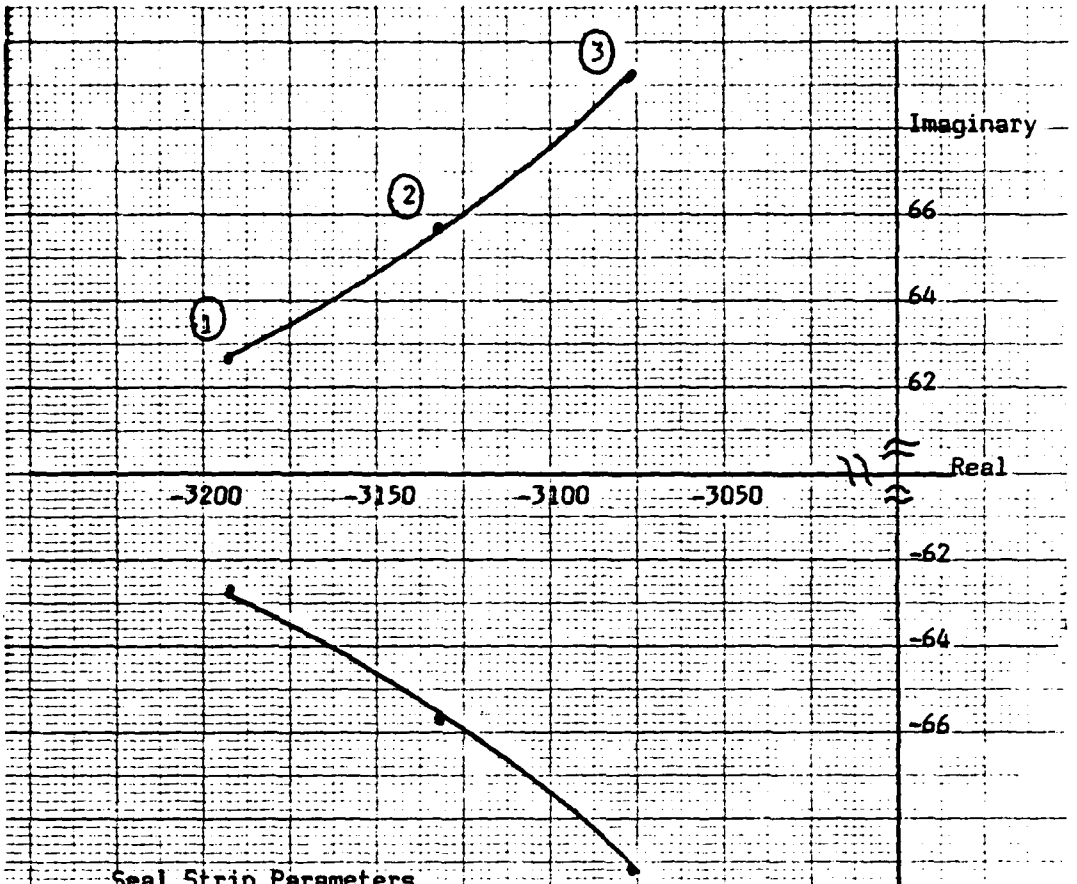

Seal Strip Parameters

(1) a = .195 in, b = .195 in, P_n = 1.89 psi,
M_A = .667 , M_B = 1.000

(2) a = .194 in, b = .196 in, P_n = 1.89 psi,
M_A = .667 , M_B = 1.000

(3) a = .193 in, b = .197 in, P_n = 1.89 psi,
M_A = .667 , M_B = 1.000

Nominal Values

P_A = 2.55 psi
P_B = 1.00 psi
h_n = .200 in
ℓ = .100 in

r = 10.0 in
ω = 579.45 Rad/Sec
= 92.22 Rev/Sec

Figure 4.12a - RWD4P Results - Seal Convergence Variation, Eigenvalues - Axial Mode

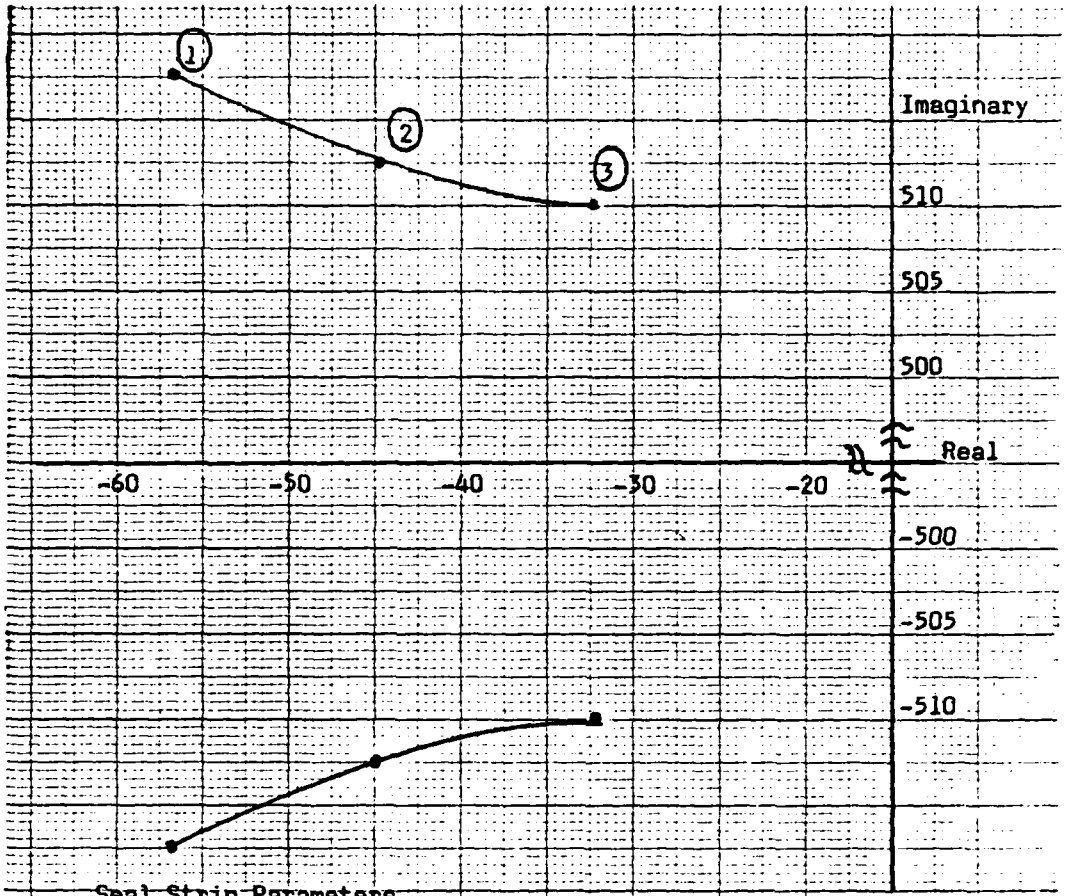

Seal Strip Parameters

(1) a = .195 in, b = .195 in, P_n = 1.89 psi,
M_A = .667 , M_B = 1.000

(2) a = .194 in, b = .196 in, P_n = 1.89 psi,
M_A = .667 , M_B = 1.000

(3) a = .193 in, b = .197 in, P_n = 1.89 psi,
M_A = .667 , M_B = 1.000

Nominal Values

P_A = 2.55 psi h_n = .200 in r = 10.0 in
P_B = 1.00 psi ℓ = .100 in ω = 579.45 Rad/Sec

Figure 4.12b - RWE4P Results - Seal Convergence Variation, Eigenvalues - Circumferential Mode

convergence destabilizes both seal modes. Convergence results are expected to be equal and opposite to seal divergence results. Unfortunately, identical support pressures (P_A and P_B) for both simulations causes choked flow at seal strip B and, therefore, constant nominal chamber pressure with increasing seal convergence. However, evident reduced stabilization, with respect to seal divergence, can be attributed to rate of change of chamber pressure per equations 3.48. These mass flow rate variation relations are affected by axial flow area. They are also strong coefficients of δP in continuity equation 3.51.

4.C.9 Variable Seal Geometry at High Chamber Pressure

The results in Figure 4.13 indicate that straight seal geometry is not as stable as convergent or divergent geometries for seal modes at high chamber pressure. This result might indicate that any unequal seal geometry is stabilizing at high pressure and/or low axial fluid velocity. However, it is believed that, for flow Mach Numbers closer to 1.0, these results would be similar to those in Figures 4.11 and 4.12.

4.C.10 General Trends

The most obvious trend among these RWE4P simulations is the Circumferential mode's role as the least stable seal mode. In every simulation, it is either the least stable or the only unstable seal mode. Eigenvector analysis further supports this observation. For all simulations, the largest eigenvector component is the "A_u" component (equation 3.56b). This cosine related circumferential velocity

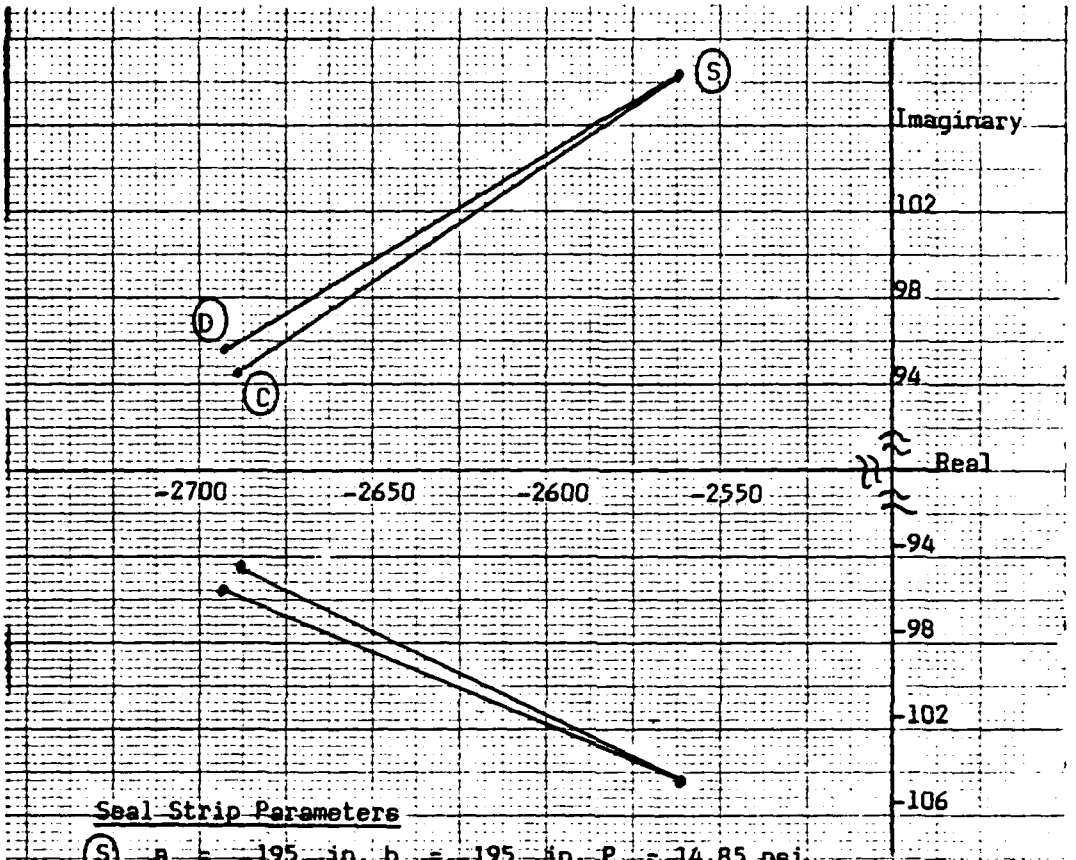

Seal Strip Parameters

(S) a = .195 in, b = .195 in, P_n = 14.85 psi
M_A = .1196 , M_B = .1208

(D) a = .196 in, b = .194 in, P_n = 14.79 psi
M_A = .1409 , M_B = .0951

(C) a = .194 in, b = .196 in, P_n = 14.91 psi
M_A = .0938 , M_B = .1418

Nominal Values

P_A = 15.0 psi h_n = .200 in r = 10.0 in
P_B = 14.7 psi ℓ = .100 in ω = 579.45 Rad/Sec

Figure 4.13a - RWE4P Results - Variable Seal Geometry at High Chamber Pressure, Eigenvalues - Axial Mode

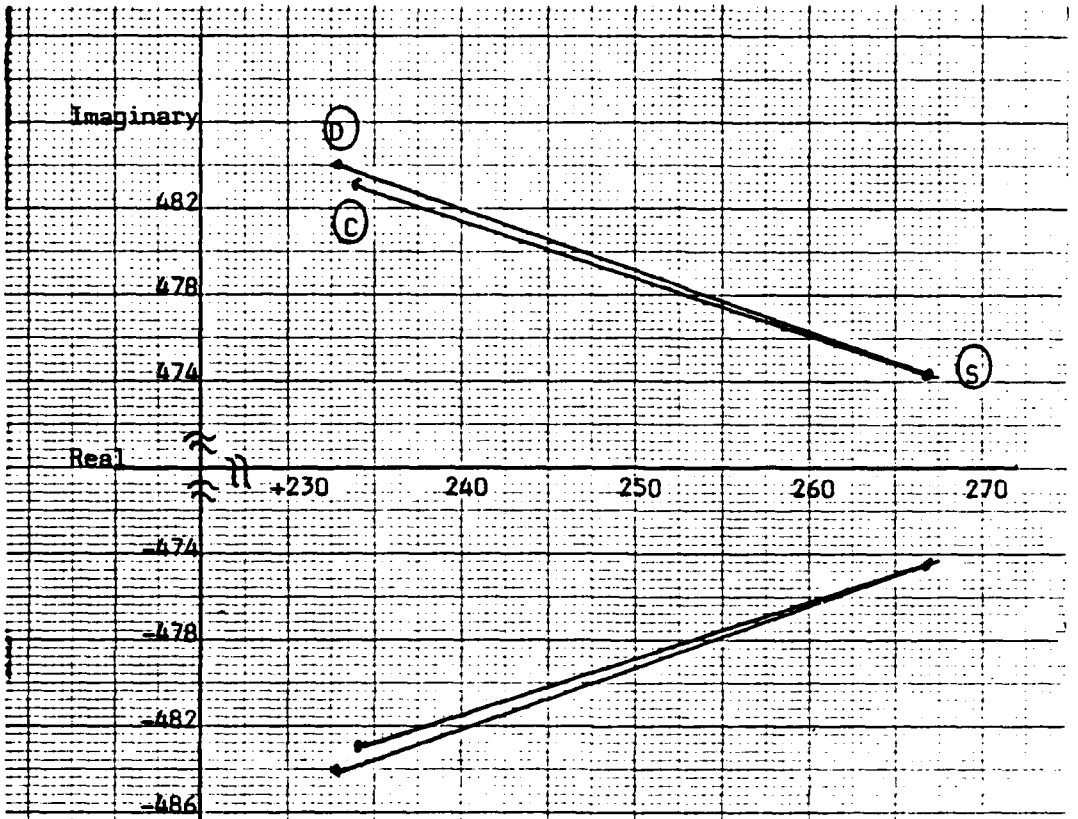

Seal Strip Parameters

(S) a = .195 in, b = .195 in, P_n = 14.85 psi
M_A = .1196 , M_B = .1208

(D) a = .196 in, b = .194 in, P_n = 14.79 psi
M_A = .1409 , M_B = .0951

(C) a = .194 in, b = .196 in, P_n = 14.91 psi
M_A = .0938 , M_B = .1418

Nominal Values

P_A = 15.0 psi h_n = .200 in r = 10.0 in
P_B = 14.7 psi ℓ = .100 in ω = 579.45 Rad/Sec

Figure 4.13b - RWT4P Results - Variable Seal Geometry at High Chamber Pressure, Eigenvalues - Circumferential Mode

coefficient exceeds axial pressure components (A_p and B_p in equation 3.56a) by, at least, a factor of 10^4. Consequently, the Circumferential mode, as the most volatile seal mode, deserves maximum attention when stability is discussed. Additionally, its modal frequency always exceeds that of the Axial mode.

One more pattern common to all RWE4P simulations is that of Axial and Circumferential modal frequencies adding to equal disc rotational frequency (ω). Explained earlier, this criterion is responsible for locating many realistic limits for seal parameters.

Of all parameter variations performed with this isolated disc and seal system, increasing seal divergence and disc speed are the most stabilizing. Increasing disc radius also has an overall stabilizing affect on the seal. The stabilizing effects of increasing both ω and r are due to consequent increasing friction between seal fluid and interacting surfaces. Although seal base to disc nominal clearance increase also stabilizes both seal modes, its limited realistic range made its usefullness as a stabilizing design parameter unpromising.

Because most RWE4P results have satisfactory physical explanations they can serve somewhat as a modeling accuracy verification. Their primary purpose, however, is, still, to provide information describing affects that individual seal parameters have on seal stability. In the next section, these parameter variations will be evaluated in the context of a coupled seal and rotor bearing system.

4.D Coupled Rotor Bearing and Seal System (RWE4S) - Results

4.D.1 Overview

Now that both rotor bearing and labyrinth seal models have been operationally proven, coupled system reactions to seal parameter variations can be discussed. First, the behavior of Myrick's 4 modes will be presented graphically. All modes are identified by comparing RWE4S eigenvalues with RWE4 and RWE4P eigenvalues obtained under the same operating conditions.* When an RWE4S eigenvalue pair more closely equals one RWE4 or RWE4P eigenvalue pair than any other, it is assigned that RWE4 or RWE4P mode's designator. Secondly, differences in behavior for these modes between coupled and rotor bearing (RWE4) systems will be discussed. Such a discussion will explain seal influence on the rotor bearing system. Finally, rotor bearing system influence on seal modes will be discussed by relating coupled system results with those for the isolated seal and disc.

The format of this discussion will parallel that used for discussing RWE4P results. The same seal and disc parameters will be varied individually. Corresponding plots for Modes 1 through 4 will be presented and explained.

4.D.2 Seal Strip Separation (ℓ) Variation

Figure 4.14 presents seal strip separation variation results

* Parameter values in Tables 4.1 and 4.2

for Myrick's first 4 modes.

Mode 1 behaves as expected for ℓ values that are near nominal (Table 4.2). Increasing ℓ beyond .1 in. (nominal) stabilizes this fundamental Myrick mode. This event might be interpreted as a "stability transfer" between Mode 1 and destabilizing seal modes (Figure 4.6). However, Mode 1 promptly begins to destabilize for $\ell >$ .1255 in., indicating an upper limit for such a stability transfer. This stability turning point also corresponds closely to actual destabilization of the Circumferential seal mode. Another eigenvalue real part direction change toward increasing stability at ℓ = .2002 in. could be either an aberation or an indication that seal strip separation growth cannot, by itself, destabilize Mode 1. However, an absence of eigenvalue real part direction change for seal modes at ℓ = .2002 in. suggests that Mode 1 destabilization will continue with continued increase in ℓ. Further speculation of such a stability transfer must await presentation of remaining ℓ variation results.

The remarkable stability of Mode 2 justifies Shapiro and Colsher's high appraisal of this mode (Figure 4.5). Despite computational accuracy to 7 digits (single precision), no change in stability or modal frequency is noticeable.

Mode 3's behavior is similar to that of Mode 1, but, with larger real part variation and reversal of modal frequency change direction. It, too, stabilizes with ℓ increase up to .1255 in. However, its modal frequency decreases for $\ell >$ .1006 in., after a gradual increase for $\ell <$ .1006 in., and then begins another gradual increase for $\ell >$ .1504 in.

Mode 4 destabilizes with increasing ℓ. Its range of eigenvalue

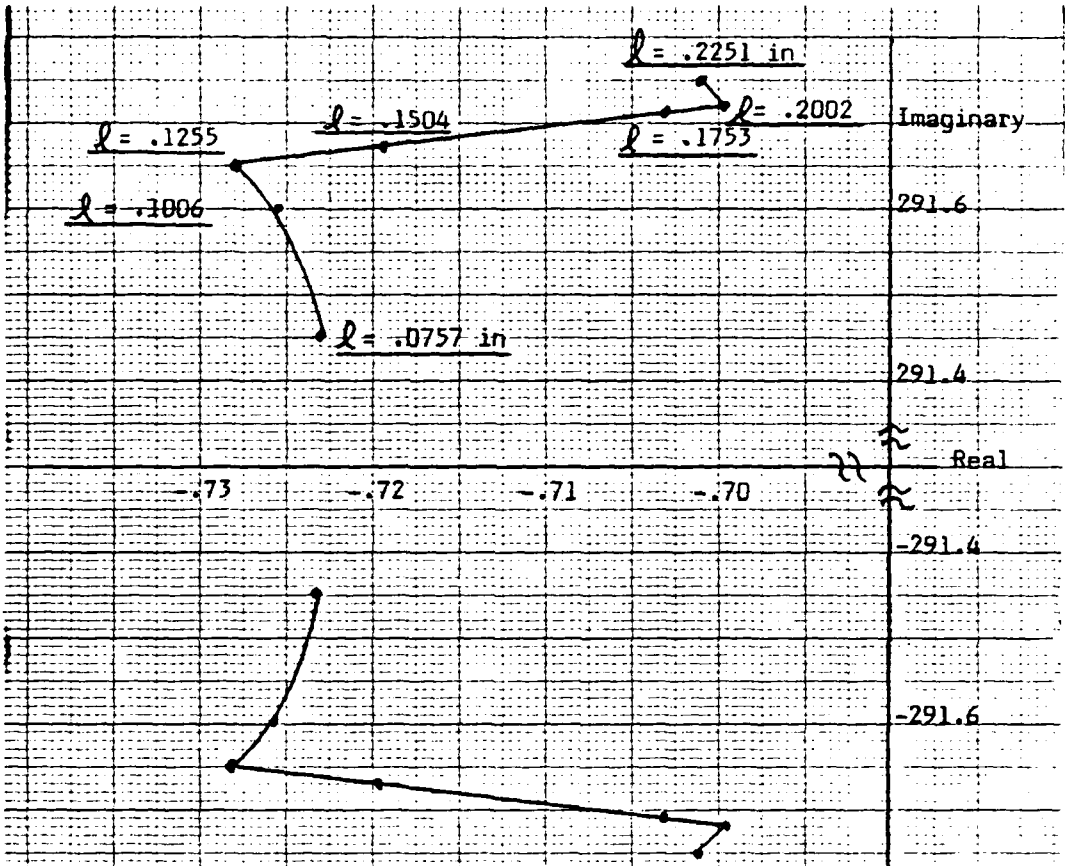

Parameter Values

P_A	= 2.55	psi
P_B	= 1.00	psi
a	= .195	in
b	= .195	in
h_n	= .200	in
$\Delta\ell$	= .0249	in
r	= 10.0	in
ω	=579.45	Rad/Sec = 92.22 Rev/Sec

Figure 4.14a - RWE4S Results - Seal Strip Separation Variation, Eigenvalues - Mode 1

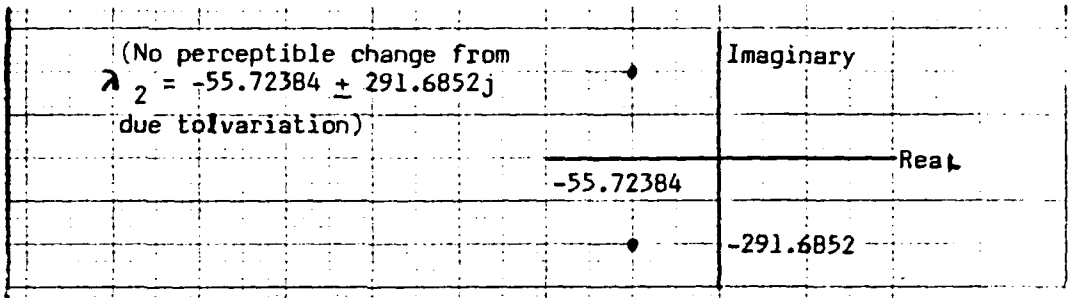

Figure 4.14b – RWE4S Results – Seal Strip Separation Variation, Eigenvalues – Mode 2

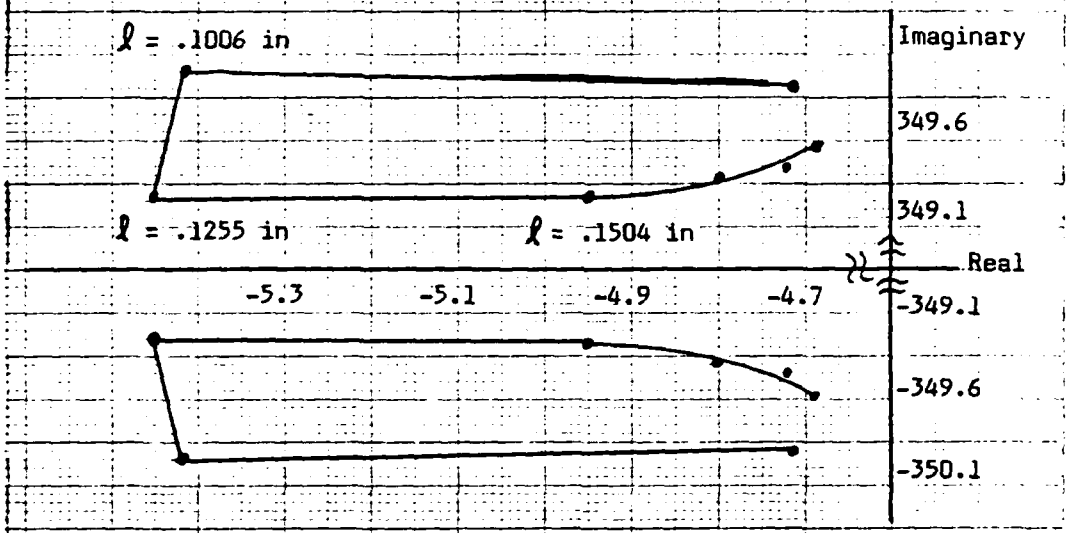

Parameter Values (Modes 2 and 3)

P_A =	2.55	psi	$\Delta\ell$ =	.0249	in
P_B =	1.00	psi	ω =	579.45	Rad/Sec
h_n =	.200	in	=	92.22	Rev/Sec
a =	.195	in			
b =	.195	in			
r =	10.0	in			

Figure 4.14c – RWE4S Results – Seal Strip Separation Variation Eigenvalues – Mode 3

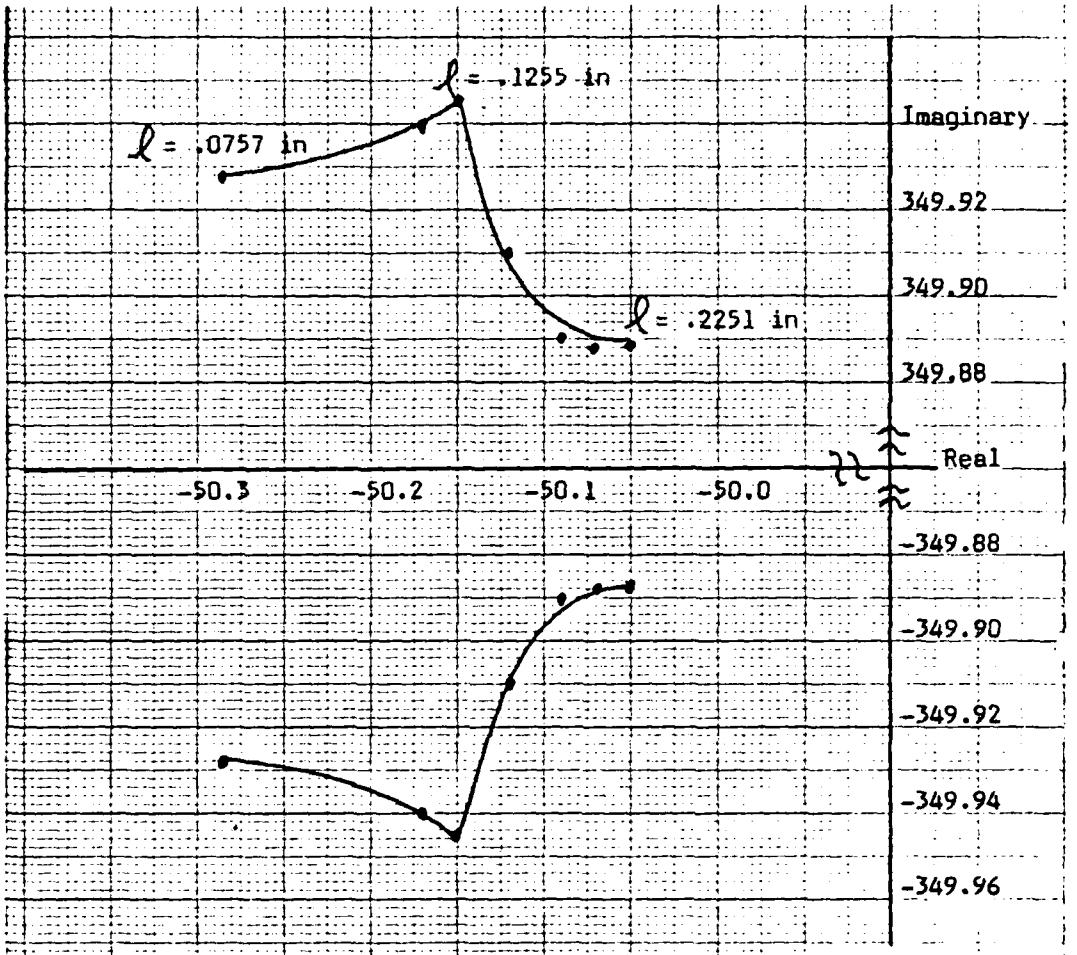

Parameter Values

P_A	= 2.55	psi	ω = 579.45 Rad/Sec
P_B	= 1.00	psi	= 92.22 Rev/Sec
h_n	= .200	in	
a	= .195	in	
b	= .195	in	
r	= 10.0	in	
$\Delta\ell$	= .0249	in	

Figure 4.14d - RWE4S Results - Seal Strip Separation Variation, Eigenvalues - Mode 4

real part variation is between that for Modes 1 and 3. At ℓ = .1255 in., its rate of destabilization decreases. Its modal frequency also begins to decrease at this point after a previous gradual increase.

For rotor bearing system Modes 1, 3, and 4, $\ell \simeq$ .1255 in. represents a transition point. Modes 1 and 3 begin destabilization while Mode 4 continues its destabilization. This point also roughly corresponds to actual Circumferential seal mode destabilization. It is plausible, therefore, that the straight geometry seal has a stabilizing effect on the rotor bearing system's most delicate modes (1 and 3) until the seal itself becomes unstable. Such an effect might also be described as a "stability transfer" from seal modes to Modes 1 and 3. This suggests that unstable circumferential flow within the seal acts, through friction, to destabilize all rotor bearing system modes. Therefore, $\ell \simeq$ .1255 in. represents an upper design limit for RWE4S straight seal stability.

4.D.3 Disc Radius (r) Variation

Figure 4.15 presents r variation results for Modes 1 through 4.

Mode 1 stabilizes normally with increasing r, i.e., it follows a smooth trend without observed aberrations. Its modal frequency also increases with increasing r.

Mode 2 is, again, unaffected. However, Mode 3 behaves almost in an equal and opposite manner with respect to ℓ variation results. Here, r = 10 in. (nominal value) is close to a transition toward destabilization. Since this value also represents near instability for the seal's Circumferential mode (Figure 4.7) a "stability transfer"

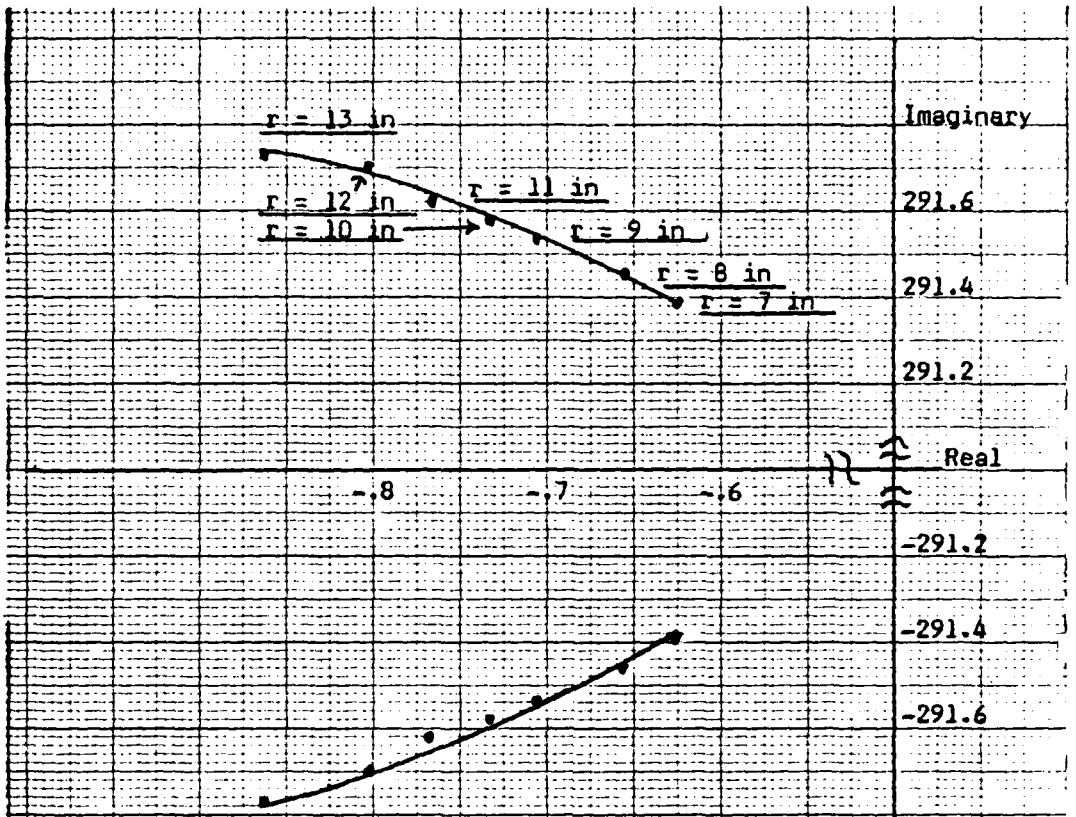

Parameter Values

P_A	= 2.55 psi	ω	= 579.45 Rad/Sec
P_B	= 1.00 psi		= 92.22 Rev/Sec
h_n	= .200 in		
a	= .195 in		
b	= .195 in		
ℓ	= .100 in		
Δr	= 1.0 in		

Figure 4.15a - RWB4S Results - Disc Radius Variation, Eigenvalues - Mode 1

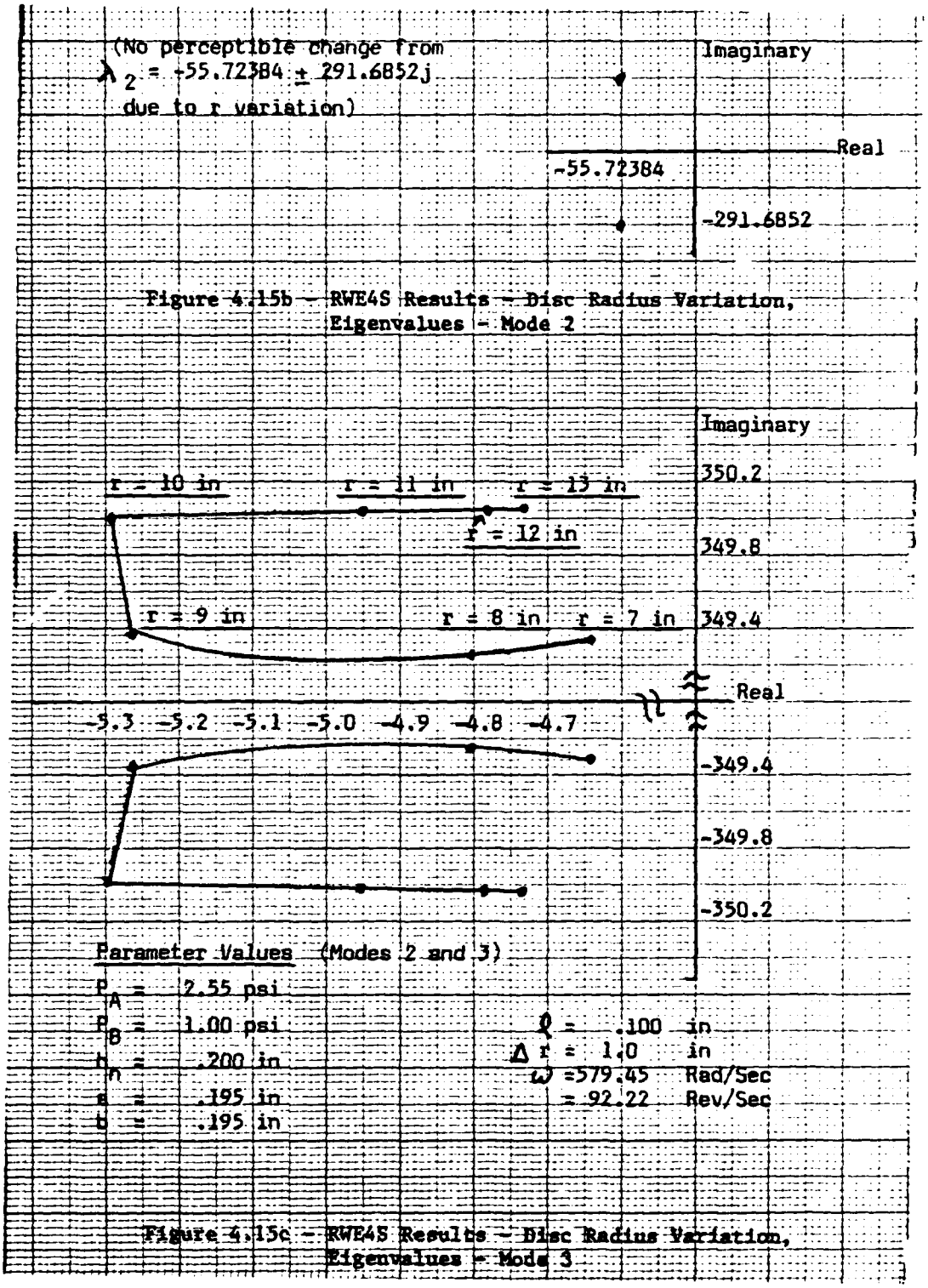

Figure 4.15b – RWE4S Results – Disc Radius Variation, Eigenvalues – Mode 2

Parameter Values (Modes 2 and 3)

P_A =	2.55 psi		
P_B =	1.00 psi	ℓ =	.100 in
h_n =	.200 in	Δr =	1.0 in
a =	.195 in	ω =	579.45 Rad/Sec
b =	.195 in	=	92.22 Rev/Sec

Figure 4.15c – RWE4S Results – Disc Radius Variation, Eigenvalues – Mode 3

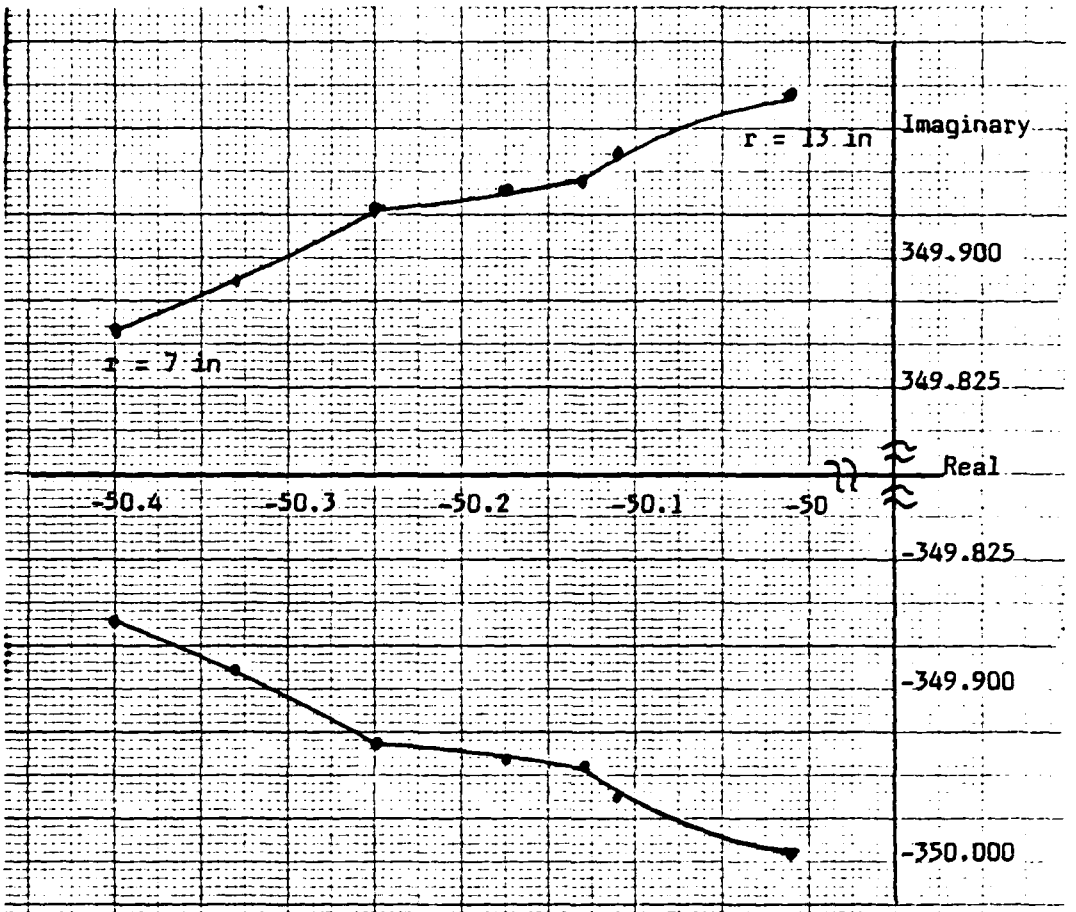

Parameter Values

P_A =	2.55	psi
P_B =	1.00	psi
h_n =	.200	in
a =	.195	in
b =	.195	in
R =	.100	in
Δr =	1.0	in

ω = 579.45 Rad/Sec
= 92.22 Rev/Sec

Figure 4.15d - RWE4S Results - Disc Radius Variation, Eigenvalues - Mode 4

theory similar to that proposed for ℓ variation, again, appears plausible.

Mode 4 destabilizes with increasing r. Its modal frequency simultaneously increases. The value r = 10 in. appears to have no special significance for this mode. However, this root locus plot is more erratic than that for Mode 1, for either seal mode, or for Mode 4 during ℓ variation. Considering also Mode 1's relatively smooth stabilizing behavior and the similarity in form between Mode 3 in both r and ℓ variations, increasing disc radius seems to have an approximately opposite effect on rotor bearing system behavior than does increasing seal strip separation.

Since increasing both ℓ and r should increase disc to seal fluid friction and since the rotor bearing system disc is modeled as a point mass, such friction is not responsible for this difference. Instead, some other feature of the Circumferential seal mode should be considered responsible. This is the only seal mode that destabilizes with increasing ℓ while stabilizing with increasing r.

4.D.4 Upstream Pressure (P_A) Variation

Figure 4.16 presents P_A variation results for Myrick's modes. These results are much less erratic than those for ℓ and r variations.

Mode 1 stabilizes with increasing P_A. Its modal frequency simultaneously decreases slightly. Mode 2 is unaffected. Mode 3 destabilizes with increasing P_A. Mode 4 stabilizes with increasing P_A while its modal frequency decreases.

Increasing pressure difference across the seal is intuitively

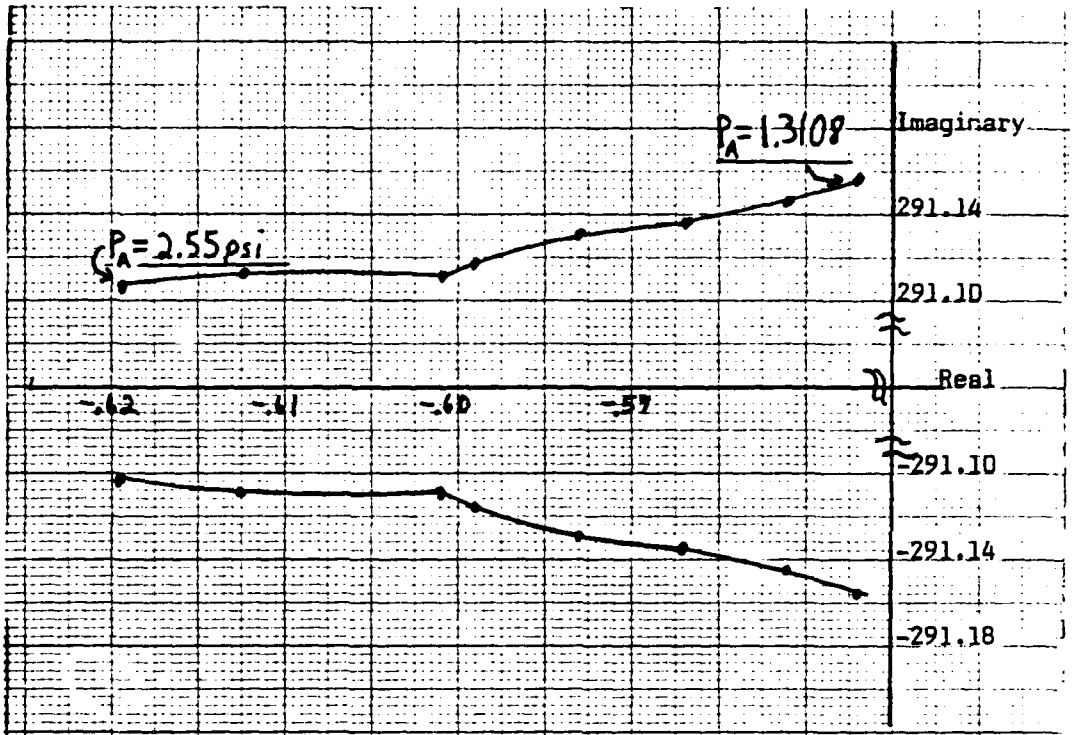

Parameter Values

P_B	=	1.00	psi
ΔP_A	=	.1549	psi
h_n	=	.200	in
a	=	.195	in
b	=	.195	in
ℓ	=	.100	in
r	=	10.0	in
ω	=	579.45	Rad/Sec
	=	92.22	Rev/Sec

Figure 4.16a - RWE4S Results - Seal Upstream Pressure Variation, Eigenvalues - Mode 1

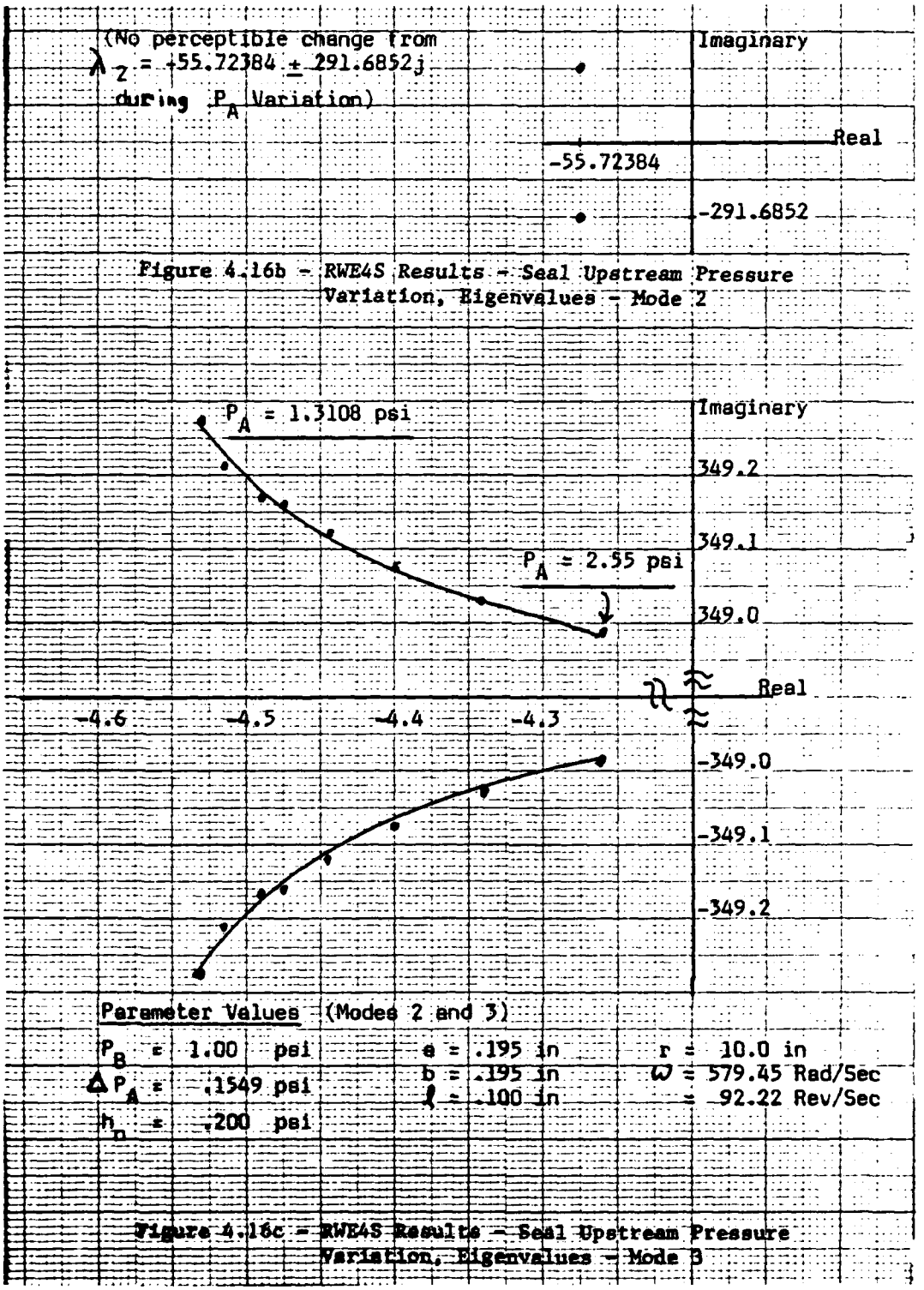

Figure 4.16b - RWE4S Results - Seal Upstream Pressure Variation, Eigenvalues - Mode 2

Parameter Values (Modes 2 and 3)

P_B =	1.00 psi	a =	.195 in	r =	10.0 in
ΔP_A =	.1549 psi	b =	.195 in	ω =	579.45 Rad/Sec
h_o =	.200 psi	ℓ =	.100 in	=	92.22 Rev/Sec

Figure 4.16c - RWE4S Results - Seal Upstream Pressure Variation, Eigenvalues - Mode 3

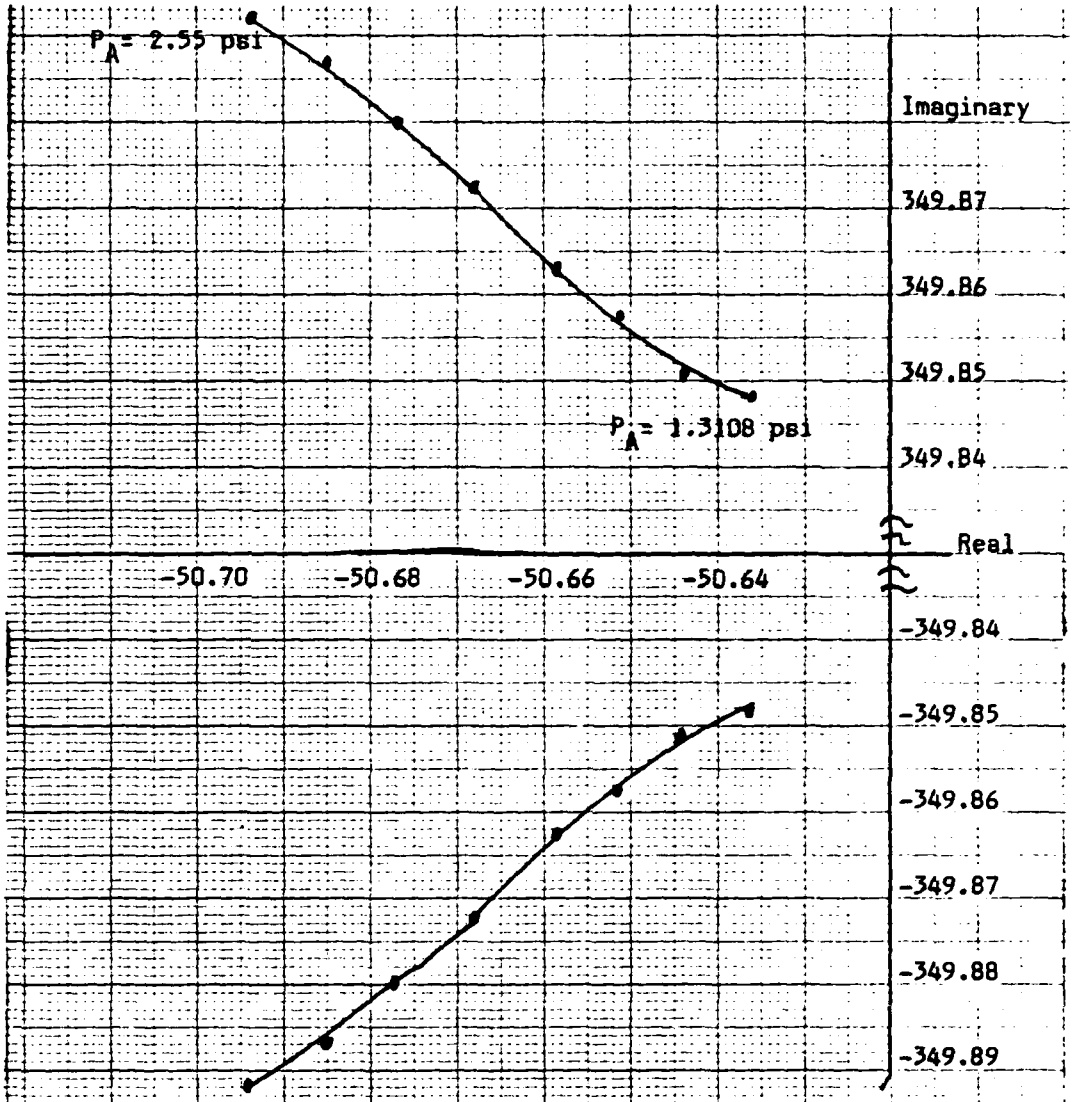

Parameter Values

P_B	=	1.00	psi	ℓ =	.100 in
ΔP_A	=	.1549	psi	r =	10.0 in
				ω =	579.45 Rad/Sec
h_n	=	.200	in	=	92.22 Rev/Sec
a	=	.195	in		
b	=	.195	in		

Figure 4.16d - RWEAS Results - Seal Upstream Pressure Variation, Eigenvalues - Mode 4

believed to be destabilizing. Accordingly, Mode 1 should be destabilized by such increasing pressure since it is the most susceptible mode to self excited instability. However, these results challenge such a belief. This surprising result is significant in that increasing upstream pressure might help reduce the nemesis of Mode 1 -- speed induced or self excited instability. By increasing upstream pressure when rotor speed approaches the stability threshold, Mode 1 instability might be postponed.

4.D.5 Seal Base to Disc Nominal Clearance (h_n) Variation Results.

Figure 4.17 presents h_n variation results. As in isolated disc and seal simulations, an upper realistic limit is encountered. Root locus plots reflect unrealistic eigenvalues with dotted lines.

Mode 1 is stabilized by increasing h_n within realistic limits while its modal frequency is decreased. Mode 2 is finally affected by a seal parameter variation. It is slightly stabilized. Its modal frequency is increased with increasing h_n. Mode 3 is destabilized with increasing h_n while its modal frequency is increased. Mode 4 is also destabilized. Its modal frequency is decreased.

4.D.6 Disc Angular Velocity (ω) Variation

Figure 4.18 presents disc speed variation results. Mode 1 demonstrates a stability threshold (92.69 rev/sec) slightly higher than the RWE4 result (92.56 rev/sec). It also exhibits a stabilizing trend

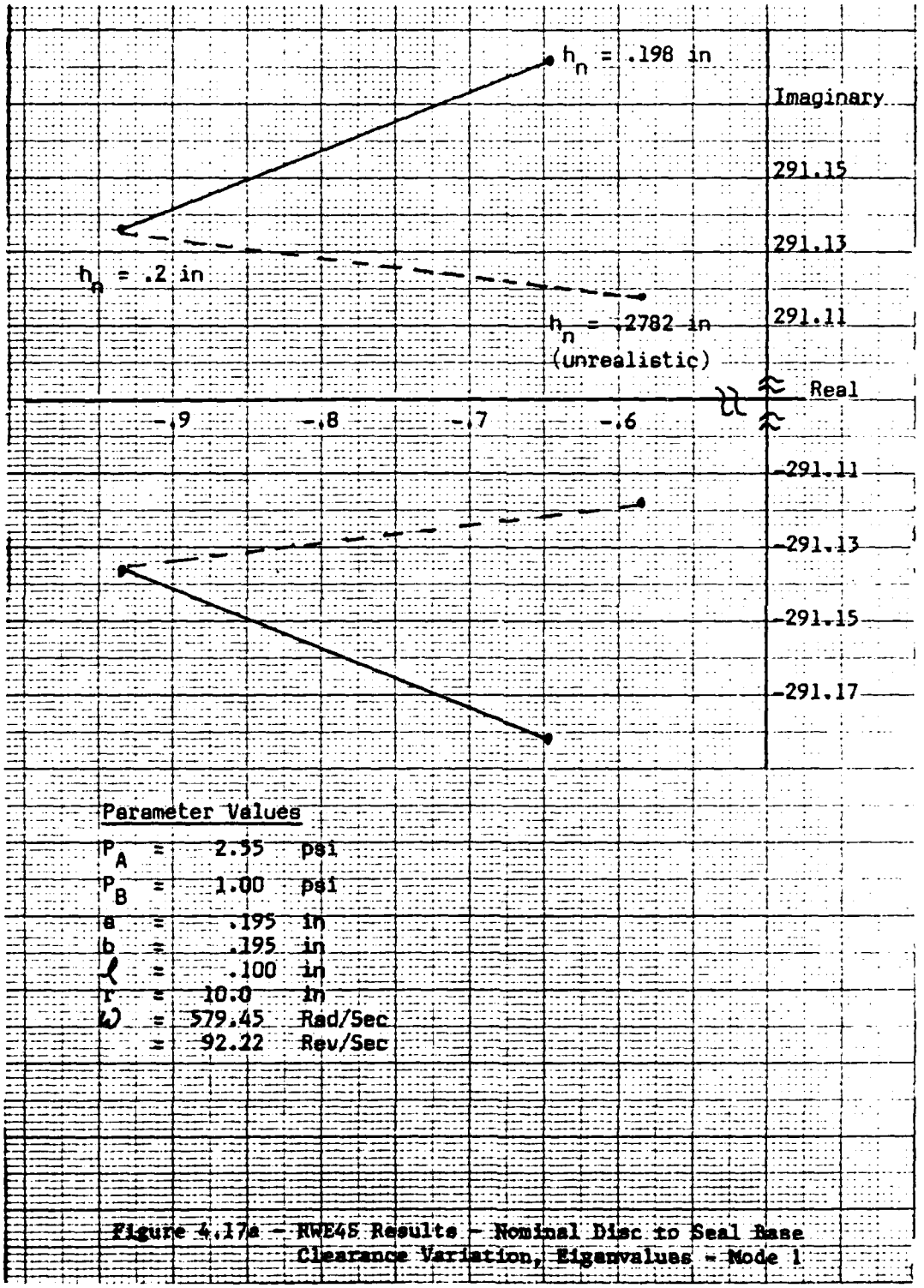

Parameter Values

P_A	=	2.55	psi
P_B	=	1.00	psi
a	=	.195	in
b	=	.195	in
ℓ	=	.100	in
r	=	10.0	in
ω	=	579.45	Rad/Sec
	=	92.22	Rev/Sec

Figure 4.17a – RWE45 Results – Nominal Disc to Seal Base Clearance Variation, Eigenvalues – Mode 1

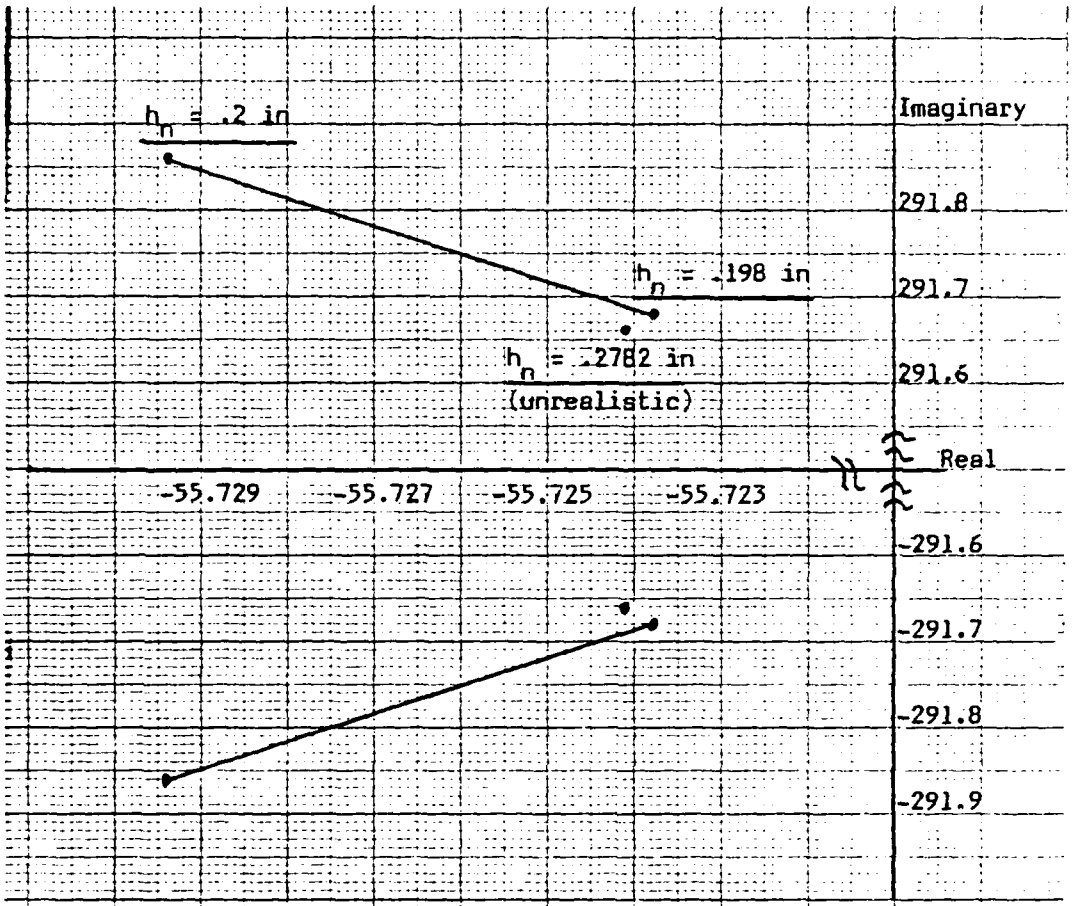

Parameter Values

P_A	= 2.55 psi	ω	= 579.45 Rad/Sec
P_B	= 1.00 psi		= 92.22 Rev/Sec
a	= .195 in		
b	= .195 in		
ℓ	= .100 in		
r	= 10.0 in		

Figure 4.17b - RWE4S Results - Nominal Disc to Seal Base Clearance Variation, Eigenvalues - Mode 2

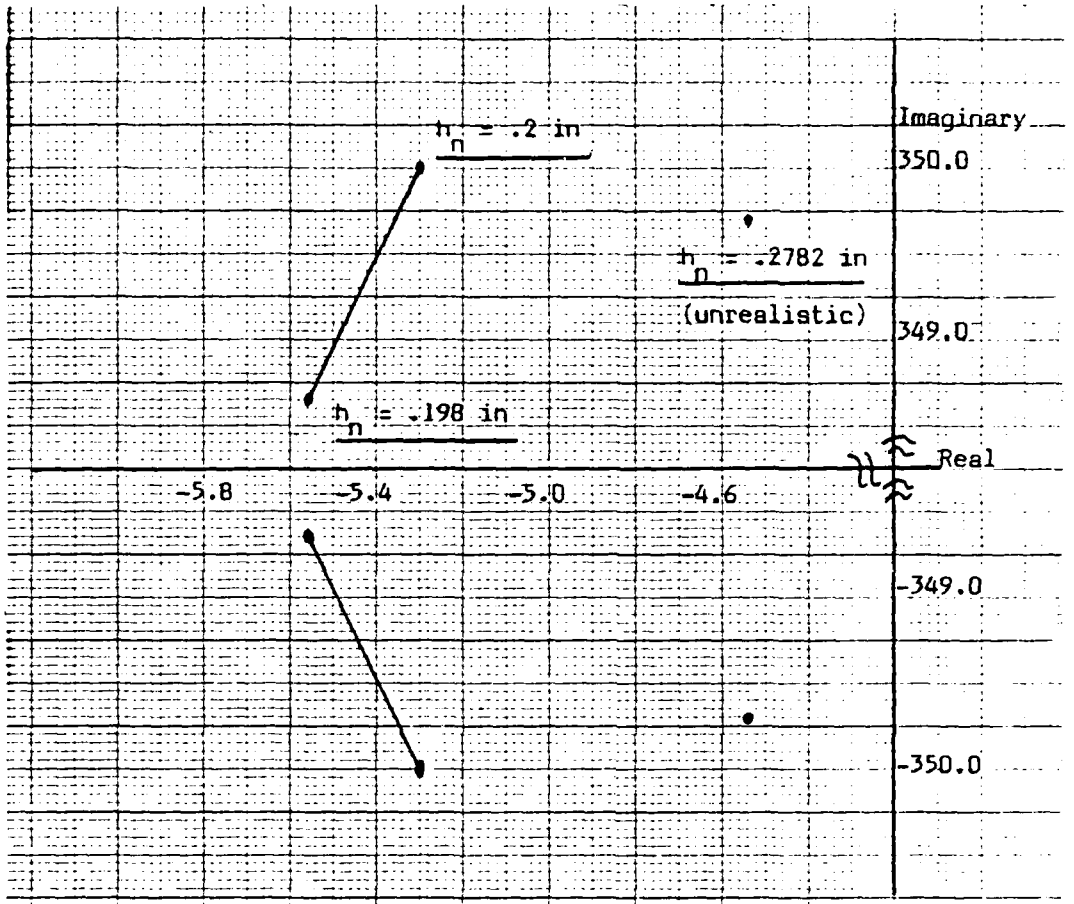

Parameter Values

P_A	=	2.55 psi	ω	= 579.45 Rad/Sec
P_B	=	1.00 psi		= 92.22 Rev/Sec
a	=	.195 in		
b	=	.195 in		
ℓ	=	.100 in		
r	=	10.0 in		

Figure 4.17c - RWE4S Results - Nominal Disc to Seal Base Clearance Variation, Eigenvalues - Mode 3

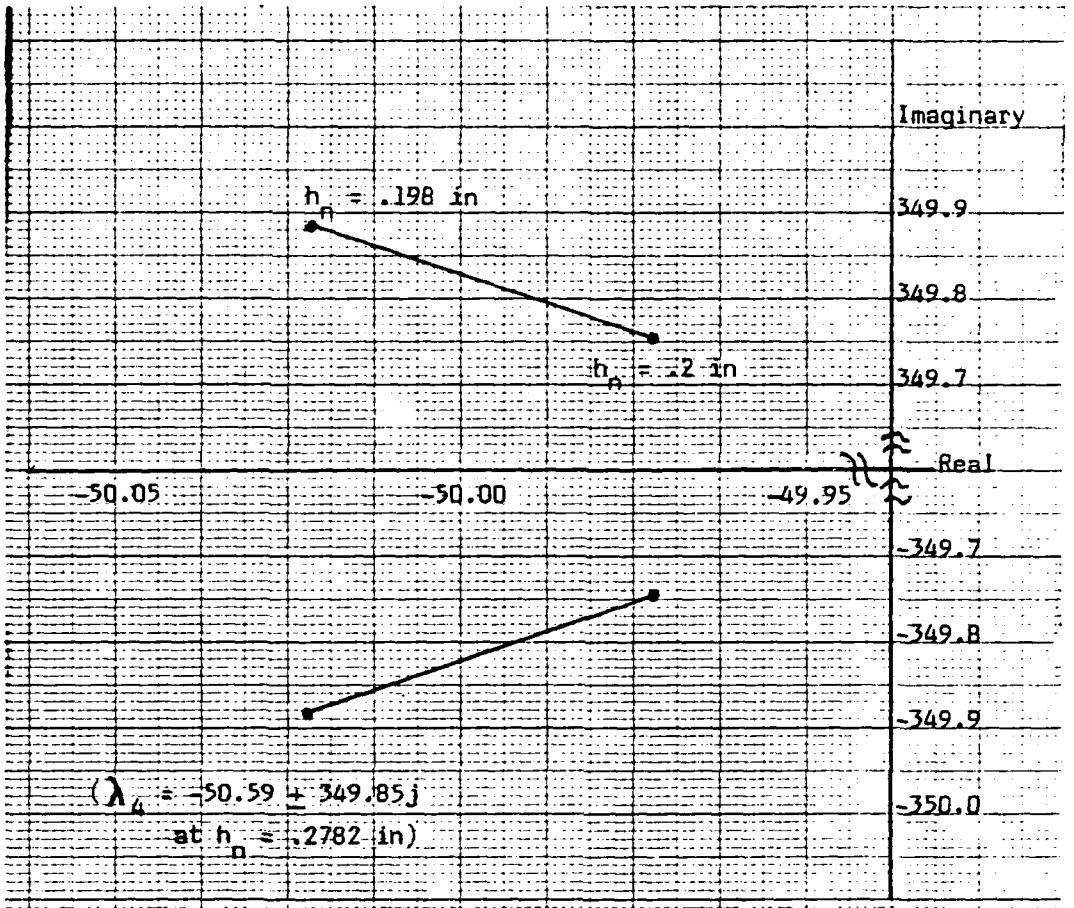

Parameter Values

P_A	= 2.55 psi	ω	= 579.45 Rad/Sec
P_B	= 1.00 psi		= 92.22 Rev/Sec
a	= .195 in		
b	= .195 in		
ℓ	= .100 in		
r	= 10.0 in		

Figure 4.17d – RWE4S Results – Nominal Disc to Seal Base Clearance Variation, Eigenvalues – Mode 4

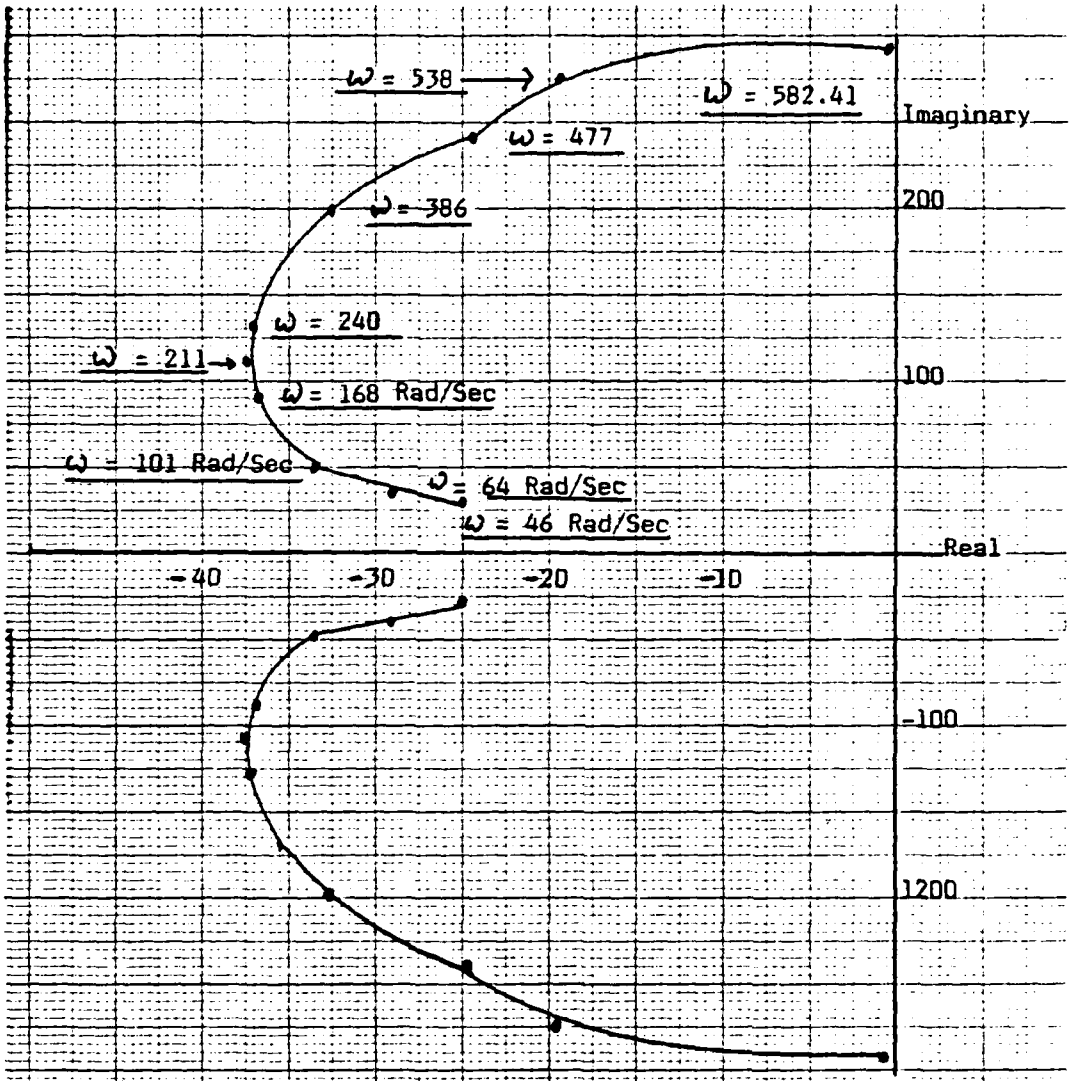

Parameter Values

P_A =	2.55 psi	b =	.195 in
P_B =	1.00 psi	ℓ =	.100 in
h_n =	.200 in	r =	10.0 in
a =	.195 in		

Figure 4.18a - RWE4S Results - Disc Speed Variation, Eigenvalues - Mode 1

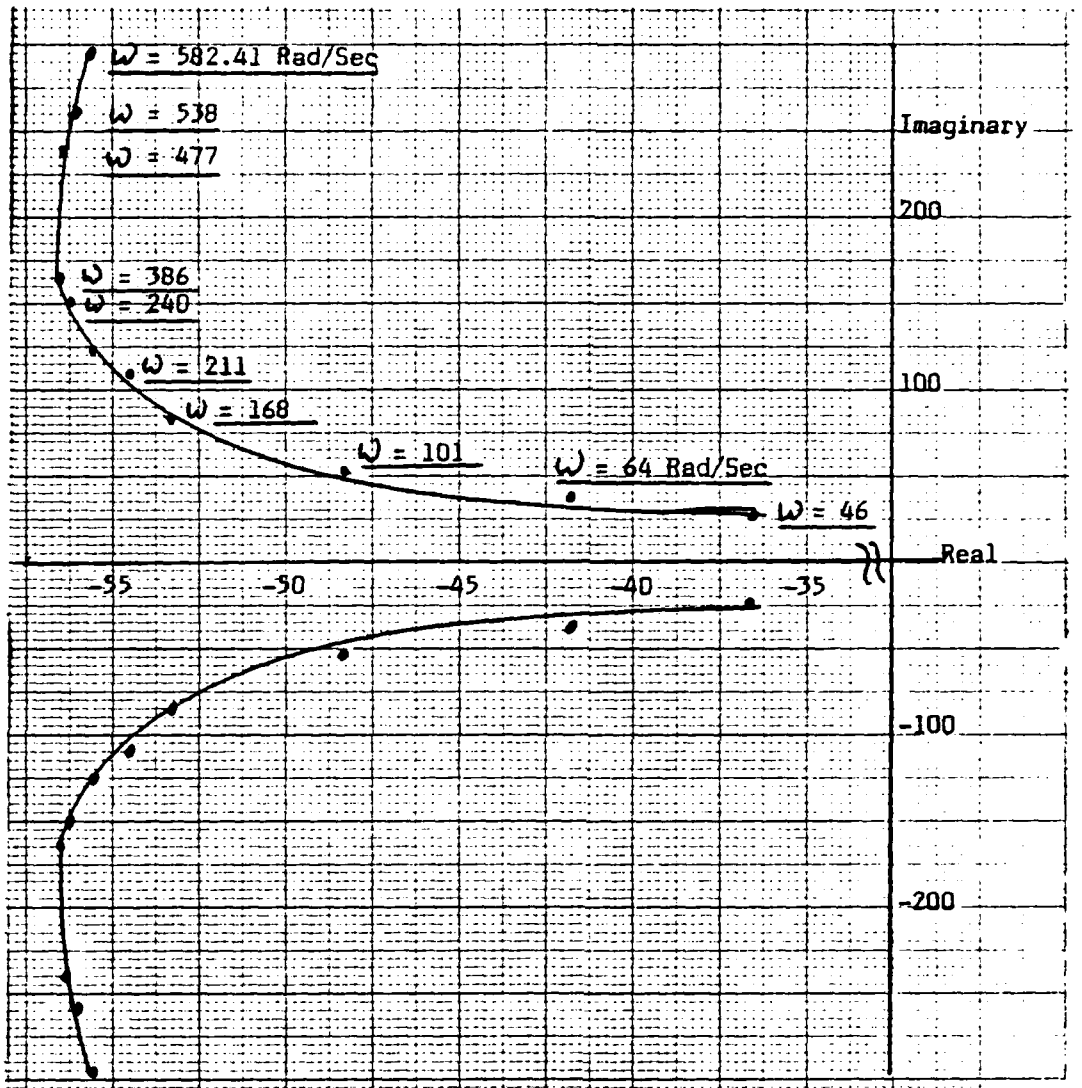

Parameter Values

P_A = 2.55 psi		b = .195 in	
P_B = 1.00 psi		ℓ = .100 in	
h_n = .200 in		r = 10.0 in	
a = .195 in			

Figure 4.18b - RWE4S Results - Disc Speed Variation, Eigenvalues - Mode 2

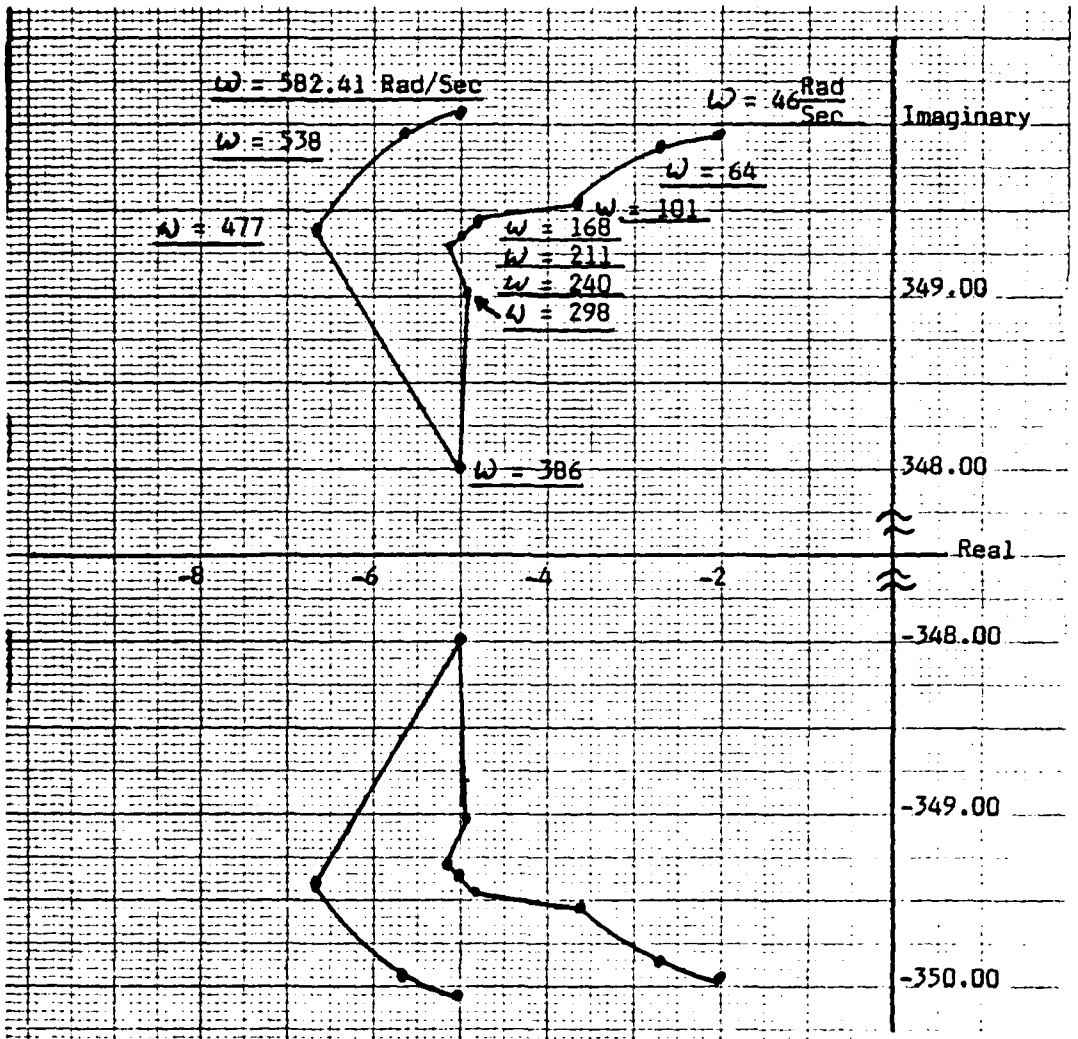

Parameter Values

P_A	= 2.55 psi	ℓ	= .100 in
P_B	= 1.00 psi	r	= 10.0 in
a	= .195 in		
b	= .195 in		
h_n	= .200 in		

Figure 4.18c - RWE4S Results - Disc Speed Variation, Eigenvalues - Mode 3

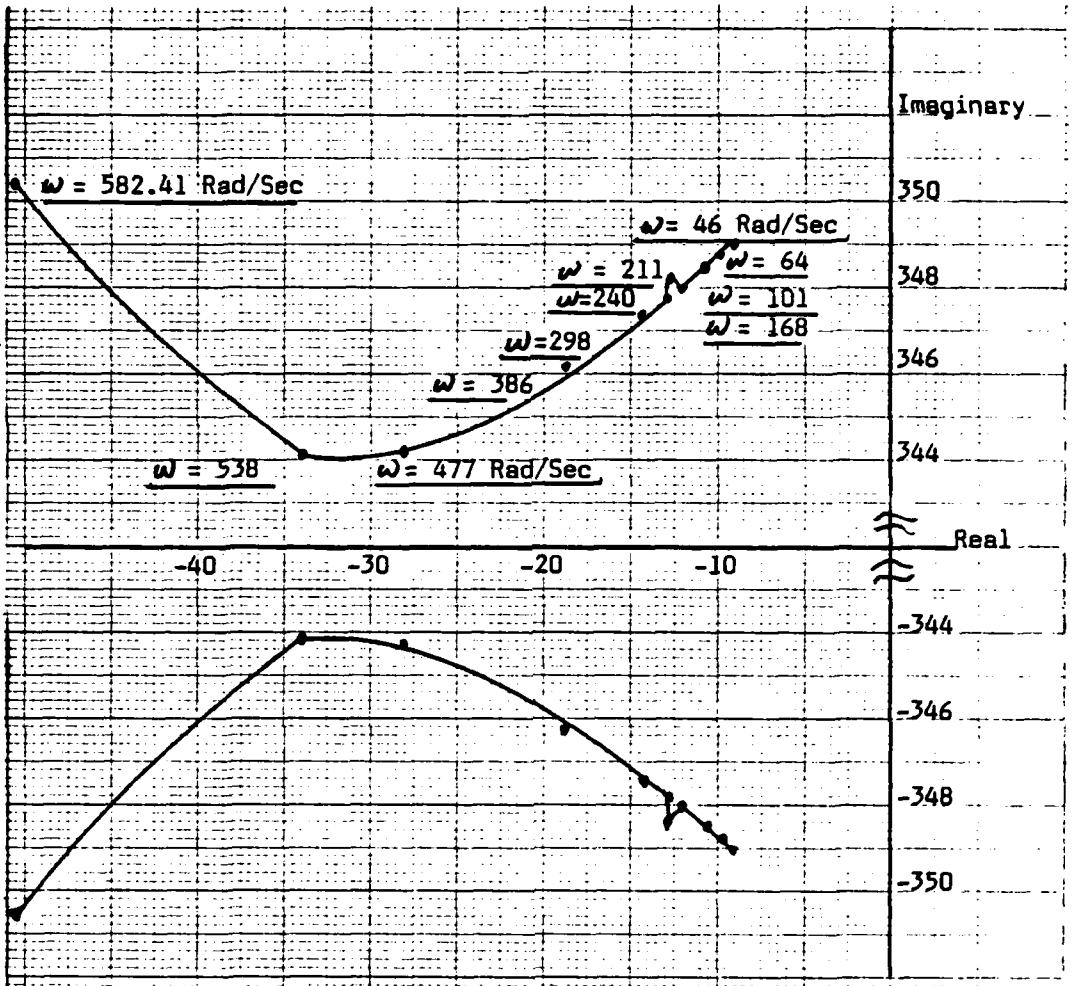

Parameter Values

P_A	=	2.55	psi	ℓ =	.100 in
P_B	=	1.00	psi	r =	10.0 in
h_n	=	.200	in		
a	=	.195	in		
b	=	.195	in		

Figure 4.18d - RWE4S Results - Disc Speed Variation, Eigenvalues - Mode 4

for ω values less than 38.22 rev/sec (240 rad/sec). Its modal frequency increases smoothly with increasing ω.

Mode 2 behaves similarly. Its transition toward destabilization with increasing ω begins at about 69 rev/sec (435 rad/sec). Although beyond range of physical operation, its stability threshold is about 464 rev/sec (2915 rad/sec).*

Mode 3 behaves erratically during speed variation. Initially, it stabilizes with ω increases up to 76 rev/sec (477 rad/sec). This eigenvalue plot changes direction 3 more times before starting a destabilizing journey that, apparently, never quite reaches the imaginary axis (eigenvalue real part at 1392 rev/sec = -.63, corresponding to ζ = .005). Such erratic behavior supports Mode 3's reputation as a lightly damped mode readily destabilized by mass unbalance but not by increasing speed.

Mode 4 is stabilized by increasing ω during the useful range of this simulation. However, like Modes 1 and 2, it also turns toward the imaginary axis. This turning point occurs at about 126 rev/sec (790 rad/sec). Its fictitious stability threshold is just below that of Mode 2 thereby supporting eventual convergence of Modes 2 and 4 with increasing ω (Figure 4.4 -- RWE4 Results). Similarly, at another large ω value, Modes 1 and 3 converge -- Mode 1, presumably, transverses the imaginary axis several times while Mode 3 approaches it asymptotically.

* Mode 1 periodically becomes unstable and then stable as speed increases toward this "threshold". Therefore, physical failure is expected well before this speed is achieved.

4.D.7 Seal Divergence Variation

Figure 4.19 presents seal divergence results. As noted, simulation 1 represents a straight geometry seal. Simulations 2 and 3 represent divergent seal geometries. Total flow area through both seal strips is maintained.

Mode 1 is stabilized by increasing seal divergence. Its modal frequency is also increased. Mode 2, again, proves itself resistant to change. Mode 3 reexhibits its penchant for erratic behavior. It is stabilized by moderate seal divergence, but, destabilized by continued divergence. Mode 4 is destabilized by increasing seal divergence.

Since stabilization of Mode 1 is required to increase stability threshold seal divergence is, apparently, beneficial. Since degree of seal divergence is physically limited*, actual destabilization of Mode 3 or 4 is unlikely with increasing seal divergence.

4.D.8 Seal Convergence Variation

Figure 4.20 presents seal convergence variation results. Conditions stated for seal divergence apply here also.

As expected, Mode 1 is destabilized by increasing seal convergence. Its small degree of destabilization relative to variable divergence induced stabilization (Figure 4.19) can be attributed to constant nominal chamber pressure caused by choked flow at seal strip B.

* $.19 \text{ in.} < a,b < h_n$

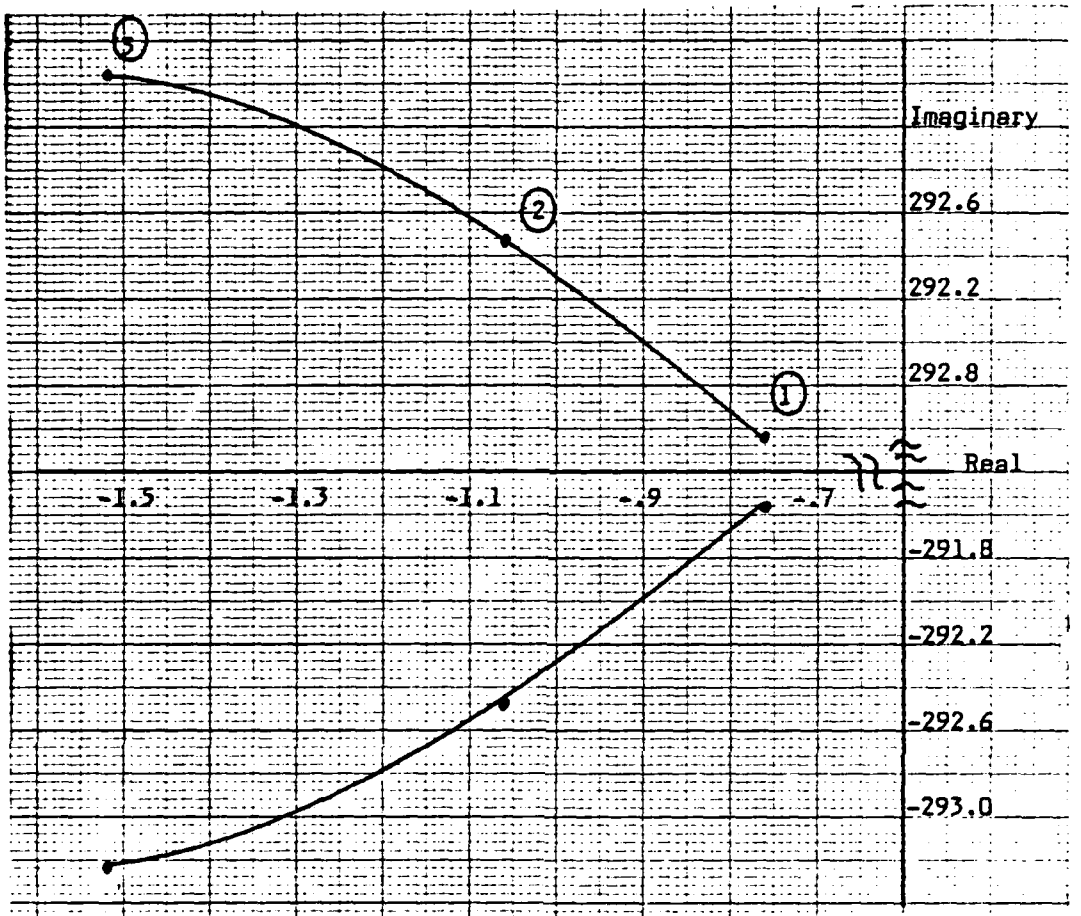

Parameter Values			Seal Strip Dimensions			
P_A	=	2.55 psi	(1)	a =	.195 in, P_n	= 1.89 psi
P_B	=	1.00 psi		b =	.195 in	
h_n	=	.200 in	(2)	a =	.196 in, P_n	= 1.69 psi
ℓ	=	.100 in		b =	.194 in	
r	=	10.0 in	(3)	a =	.197 in, P_n	= 1.34 psi
ω	=	579.45 Rad/Sec		b =	.193 in	

Figure 4.19a – RWE4S Results – Seal Divergence Variation, Eigenvalues – Mode 1

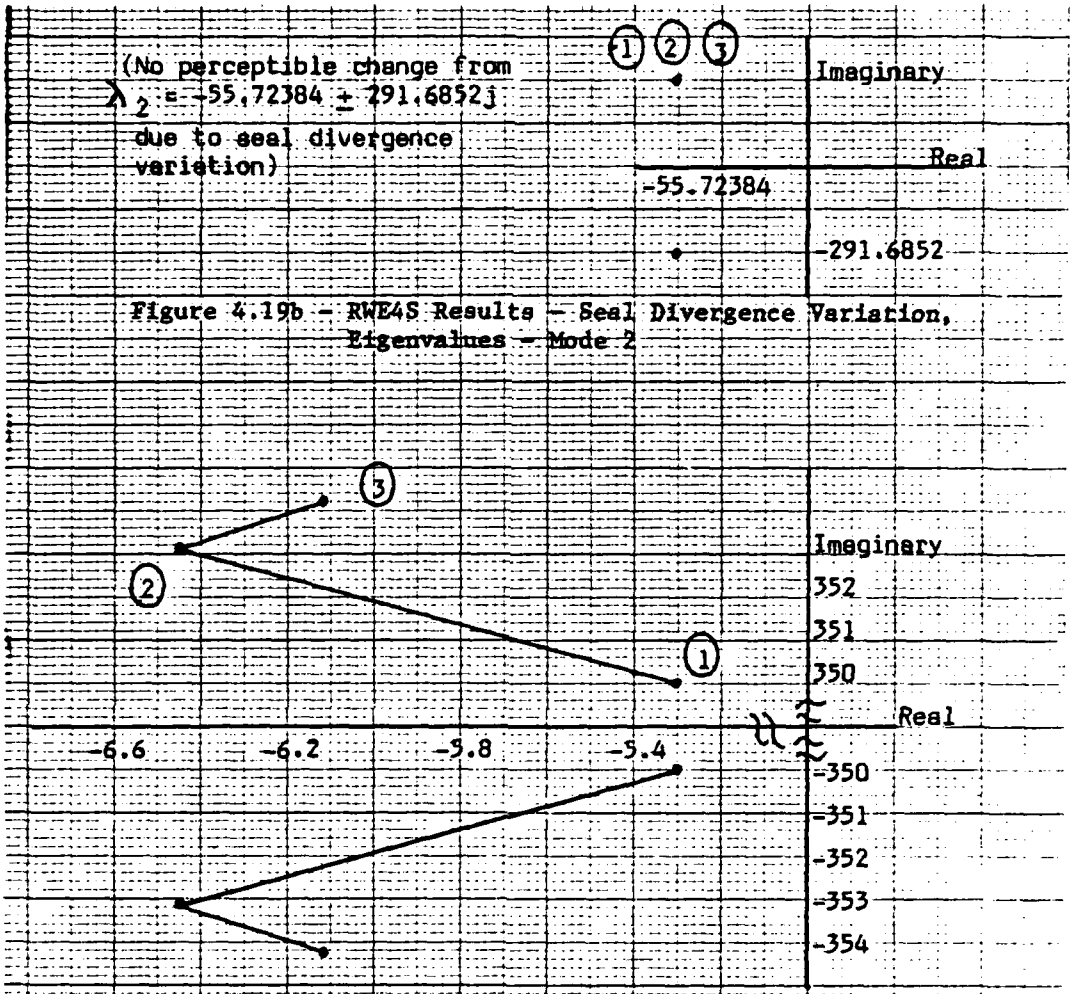

Figure 4.19b – RWE4S Results – Seal Divergence Variation, Eigenvalues – Mode 2

Parameter Values (Modes 2 and 3)			Seal Strip Dimensions		
P_A	= 2.55	psi	①	a = .195 in, P_n	= 1.89 psi
P_B	= 1.00	psi		b = .195 in	
h_n	= .200	in	②	a = .196 in, P_n	= 1.69 psi
ℓ	= .100	in		b = .194 in	
r	= 10.0	in	③	a = .197 in, P_n	= 1.34 psi
ω	= 579.45	Rad/Sec		b = .193 in	

Figure 4.19c – RWE4S Results – Seal Divergence Variation, Eigenvalues – Mode 3

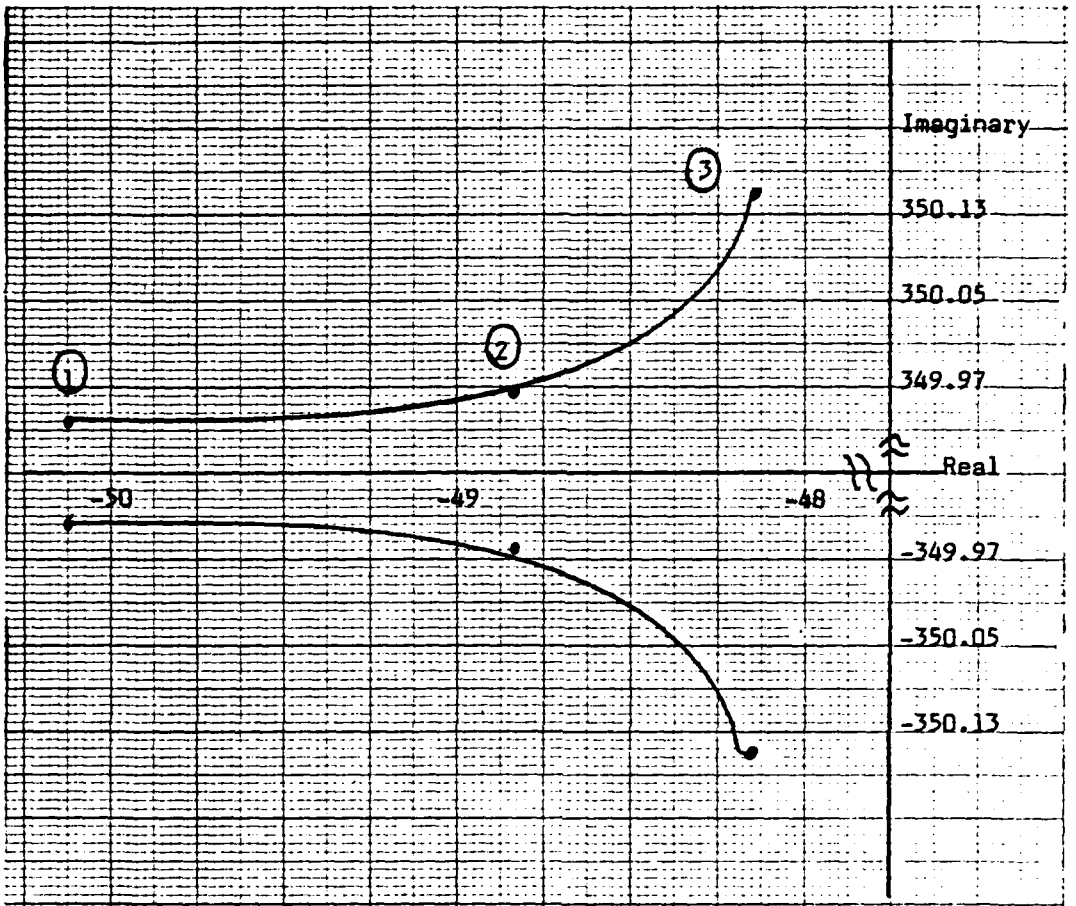

Parameter Values		Seal Strip Dimensions			
P_A = 2.55 psi		(1)	a = .195 in,	P_n = 1.89 psi	
P_B = 1.00 psi			b = .195 in		
h_n = .200 in		(2)	a = .196 in,	P_n = 1.69 psi	
ℓ = .100 in			b = .194 in		
r = 10.0 in		(3)	a = .197 in,	P_n = 1.34 psi	
ω = 579.45 Rad/Sec			b = .193 in		

Figure 4.19d - RWE4S Results - Seal Divergence Variation, Eigenvalues - Mode 4

Mode 3 is stabilized by increasing seal convergence while mode 4 is destabilized. Again, rates of eigenvalue real part change relative to variable seal divergence simulations are marginal due to constant nominal chamber pressure.

4.D.9 Variable Seal Geometry at High Chamber Pressure

Figure 4.21 presents high chamber pressure results. Here, seal geometry varies from convergent to divergent while relative pressure drop across the seal* is maintained at a relatively low level. Nominal chamber pressure is increased approximately by a factor of 10. The stability reversals evident for seal modes (Figure 4.13) are not exhibited by rotor bearing system modes.

Mode 1 is stabilized by decreasing seal convergence (or increasing divergence) thereby maintaining predicted behavior (Figure 4.19). Mode 3 also stabilizes as expected. Mode 4 satisfies the prediction of Figure 4.19 by destabilizing with increasing divergence.

It should be remembered that these results, particularly Mode 1's, are of primary interest when considering stability threshold enhancement. Here, predicted Mode 1 stabilization with diverging seal geometry is encouraging. Unfortunately, the seal Circumferential mode is unstable during all of these high pressure simulations making experimental verification impossible. Additionally, more simulations at other pressure (P_A, P_B) and pressure drop (P_A-P_B) values are needed to provide confidence in maintaining this assertion of improved stability at

* $(P_A - P_B)/P_A$

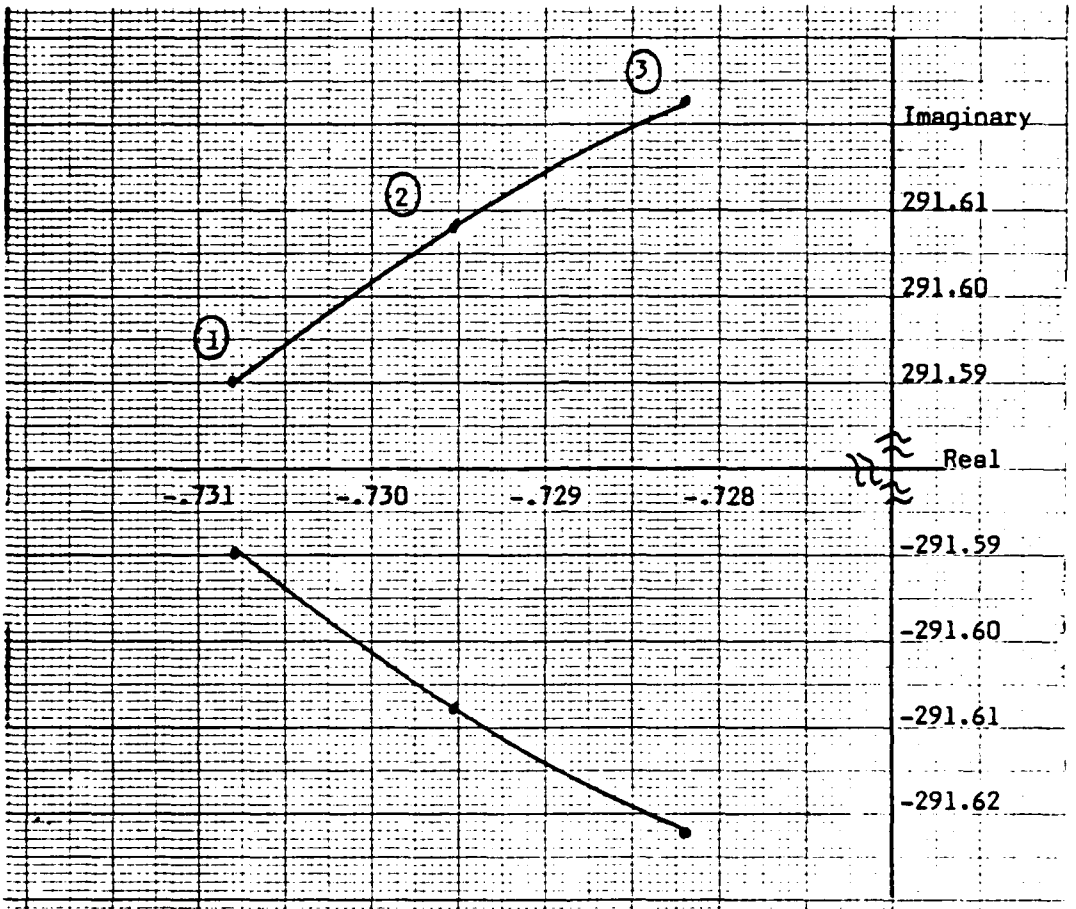

Parameter Values		Seal Strip Dimensions		
P_A = 2.55 psi		(1) a = .195 in, P_n = 1.89 psi		
P_B = 1.00 psi		b = .195 in		
h_n = .200 in		(2) a = .194 in, P_n = 1.89 psi		
ℓ = .100 in		b = .196 in		
r = 10.0 in		(3) a = .193 in, P_n = 1.89 psi		
ω = 579.45 Rad/Sec		b = .197 in		

Figure 4.20a - RWE4S Results - Seal Convergence Variation, Eigenvalues - Mode 1

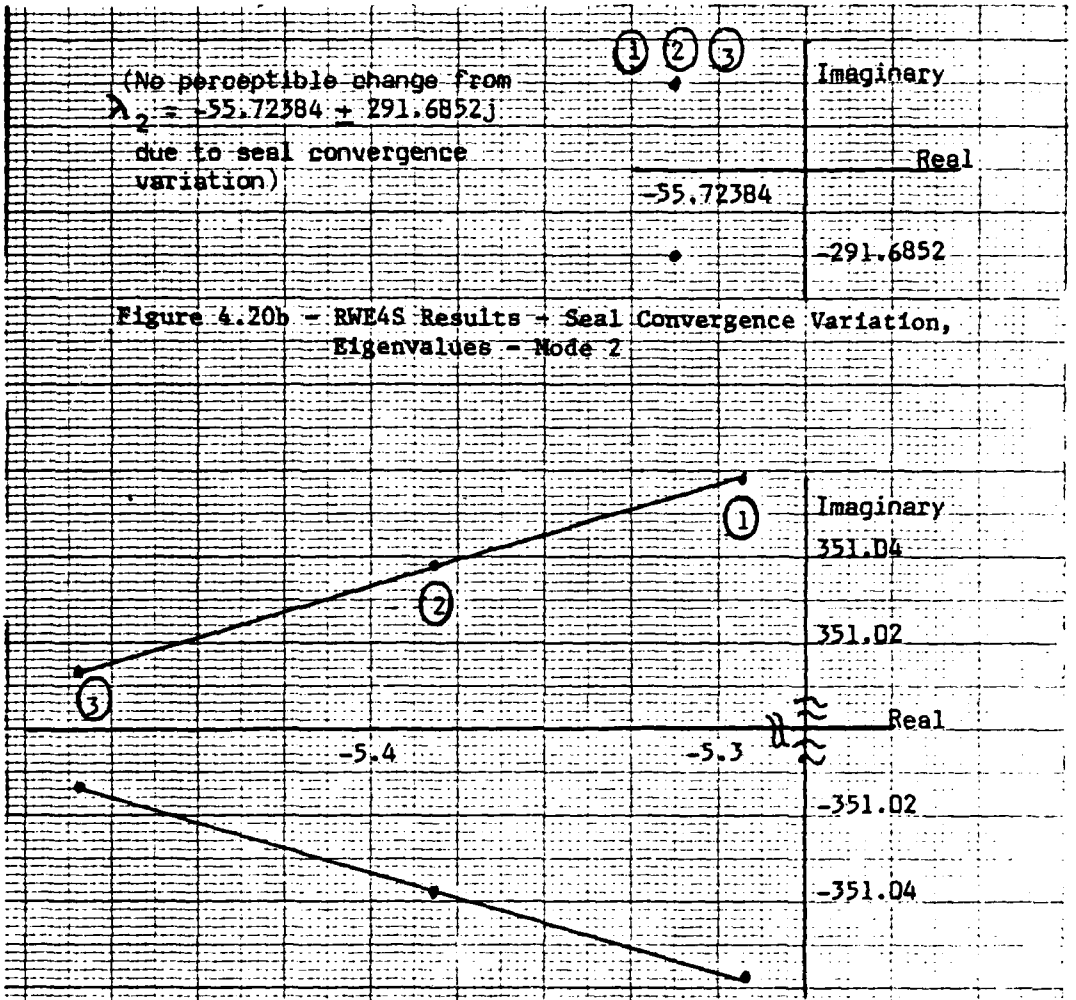

Figure 4.20b – RWE4S Results – Seal Convergence Variation, Eigenvalues – Mode 2

Parameter Values (Modes 2 and 3)			Seal Strip Dimensions		
P_A	= 2.55	psi	(1)	a = .195	in, P_n = 1.89 psi
P_B	= 1.00	psi		b = .195	in
h_n	= .200	in	(2)	a = .194	in, P_n = 1.89 psi
ℓ	= .100	in		b = .196	in
r	= 10.0	in	(3)	a = .193	in, P_n = 1.89 psi
ω	= 579.45	Rad/Sec		b = .197	in

Figure 4.20c – RWE4S Results – Seal Convergence Variation, Eigenvalues – Mode 3

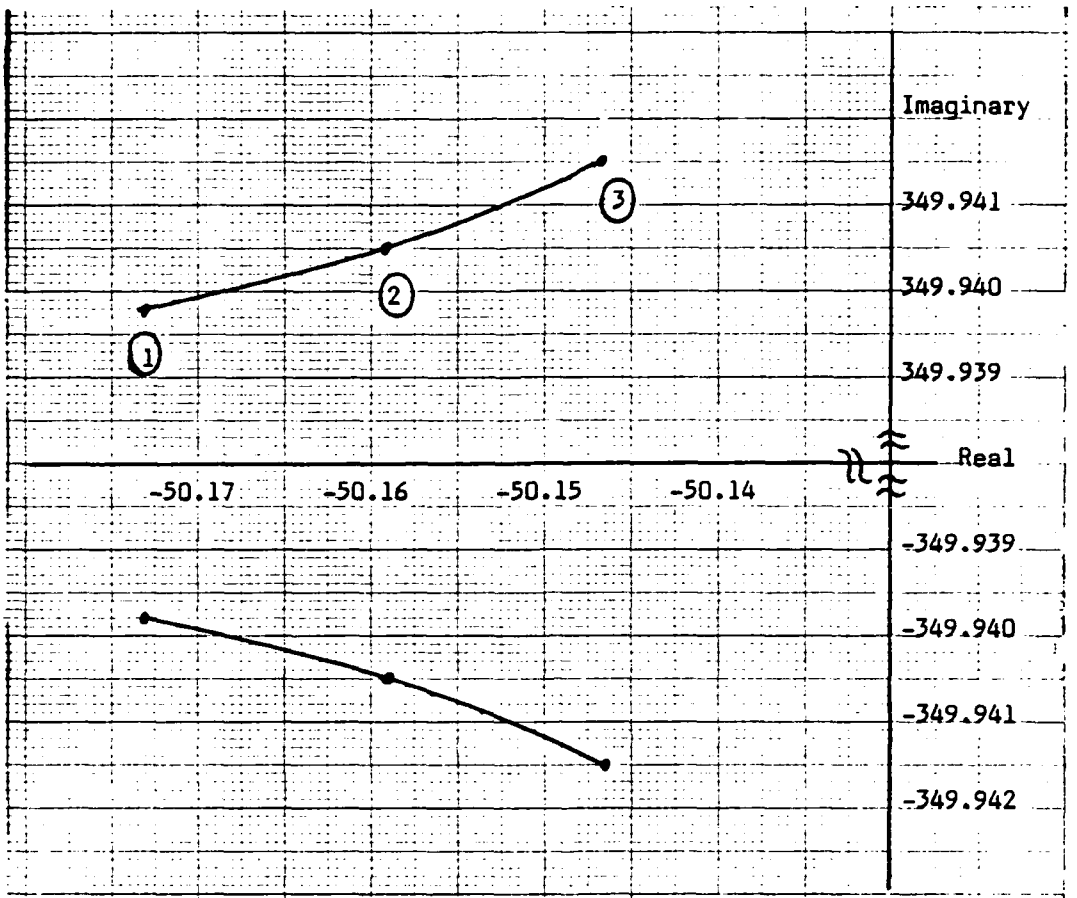

Parameter Values			Seal Strip Dimensions			
P_A	= 2.55	psi	(1)	a = .195	in, P_n	= 1.89 psi
P_B	= 1.00	psi		b = .195	in	
h_n	= .200	in	(2)	a = .194	in, P_n	= 1.89 psi
ℓ	= .100	in		b = .196	in	
r	= 10.0	in	(3)	a = .193	in, P_n	= 1.89 psi
ω	= 579.45	Rad/Sec		b = .197	in	

Figure 4.20d - RWE4S Results - Seal Convergence Variation, Eigenvalues - Mode 4

high chamber pressure using divergent seal geometry.

4.D.10 Speed (ω) Variation at Extreme Seal Divergence

Figure 4.22 presents root locus results for Myrick modes at extreme seal divergence and for variable rotor speeds starting near the Mode 1 stability threshold of Figure 4.18. This simulation is intended to determine a revised stability threshold due to seal divergence and to verify improved, divergence induced, coupled system stability per Figure 4.19.

Mode 1's stability threshold is increased to 93.13 rev/sec (585.16 rad/sec) because of seal divergence. This represents a .47% increase from the revised stability threshold achieved with a straight seal (Figure 4.18) and a .6% increase relative to the stability threshold for Myrick's rotor bearing system without seal (Figure 4.4).

Stability of Modes 2 and 3 is marginally degraded, but not enough to discourage further stabilization of Mode 1. Mode 4 continues its stabilizing behavior with increasing ω (Figure 4.18).

4.D.11 Seal and Rotor Bearing System Interactions

4.D.11.A Seal Influence on Rotor Bearing System Modes

Myrick modes are not radically affected by coupling with a labyrinth seal. Generally, points on root locus plots in Figures 4.14 through 4.22 are affected equally by seal modes. Although such affects cannot be positively attributed to any particular seal mode, the relative

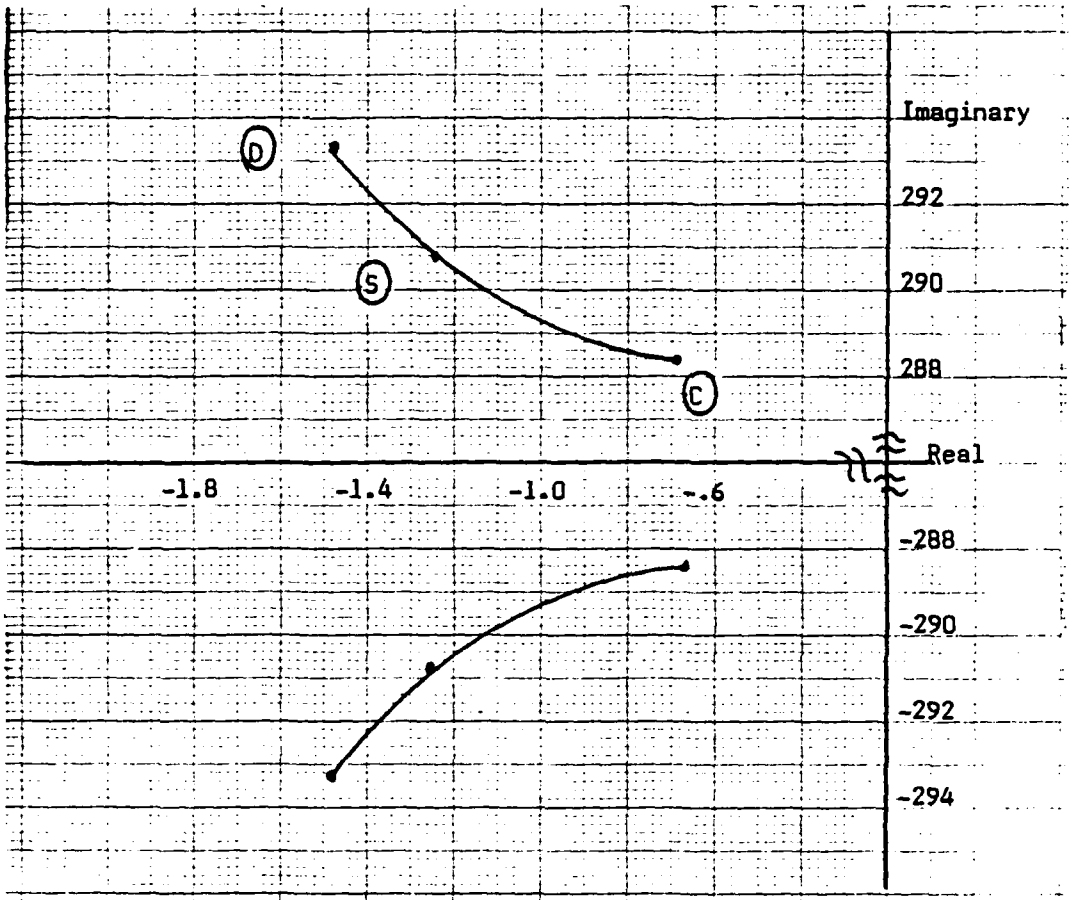

Parameter Values			Seal Strip Dimensions			
P_A	= 15.0	psi	(S)	a =	.195 in, P_n	= 14.85 psi
P_B	= 14.7	psi		b =	.195 in	
h_n	= .200	in	(D)	a =	.196 in, P_n	= 14.79 psi
ℓ	= .100	in		b =	.194 in	
r	= 10.0	in	(C)	a =	.194 in, P_n	= 14.91 psi
ω	= 579.45	Rad/Sec		b =	.196 in	

Figure 4.21a - RWE4S Results - Variable Seal Geometry at High Chamber Pressure, Eigenvalues - Mode 1

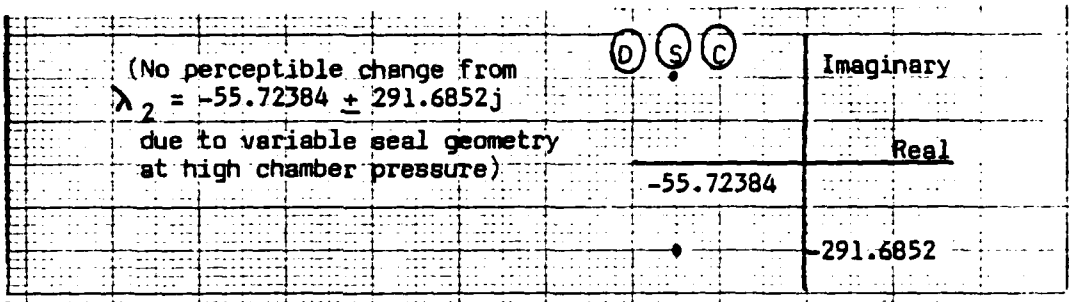

Figure 4.21b - RWE4S Results - Variable Seal Geometry at High Chamber Pressure, Eigenvalues - Mode 2

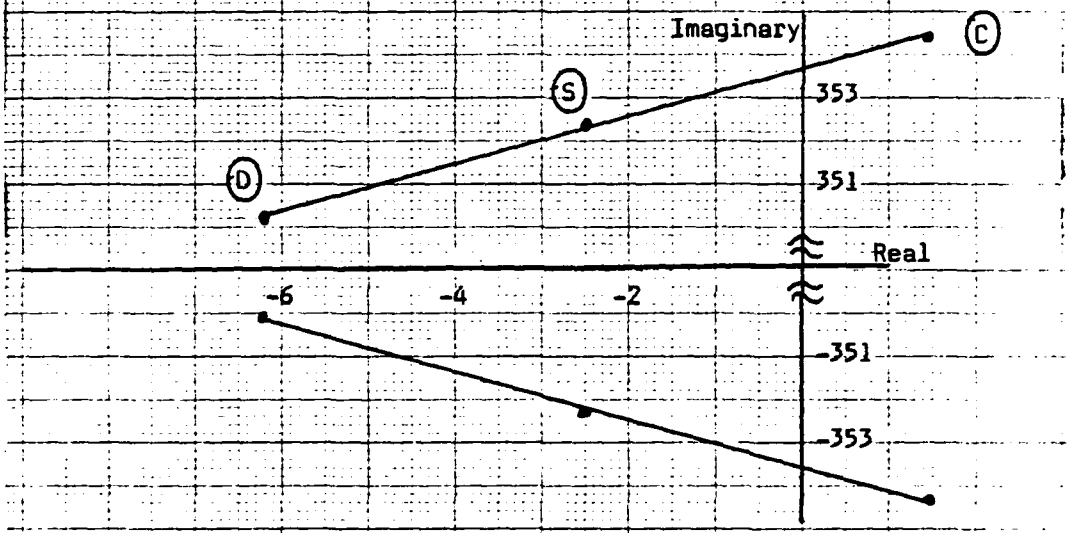

Parameter Values (Modes 2 and 3)			Seal Strip Dimensions		
P_A	= 15.0	psi	(S)	a = .195 in,	P_n = 14.85 psi
P_B	= 14.7	psi		b = .195 in	
h_n	= .200	in	(D)	a = .196 in,	P_n = 14.79 psi
ℓ	= .100	in		b = .194 in	
r	= 10.0	in	(C)	a = .194 in,	P_n = 14.91 psi
ω	= 579.45	Rad/Sec		b = .196 in	

Figure 4.21c - RWE4S Results - Variable Seal Geometry at High Chamber Pressure, Eigenvalues - Mode 3

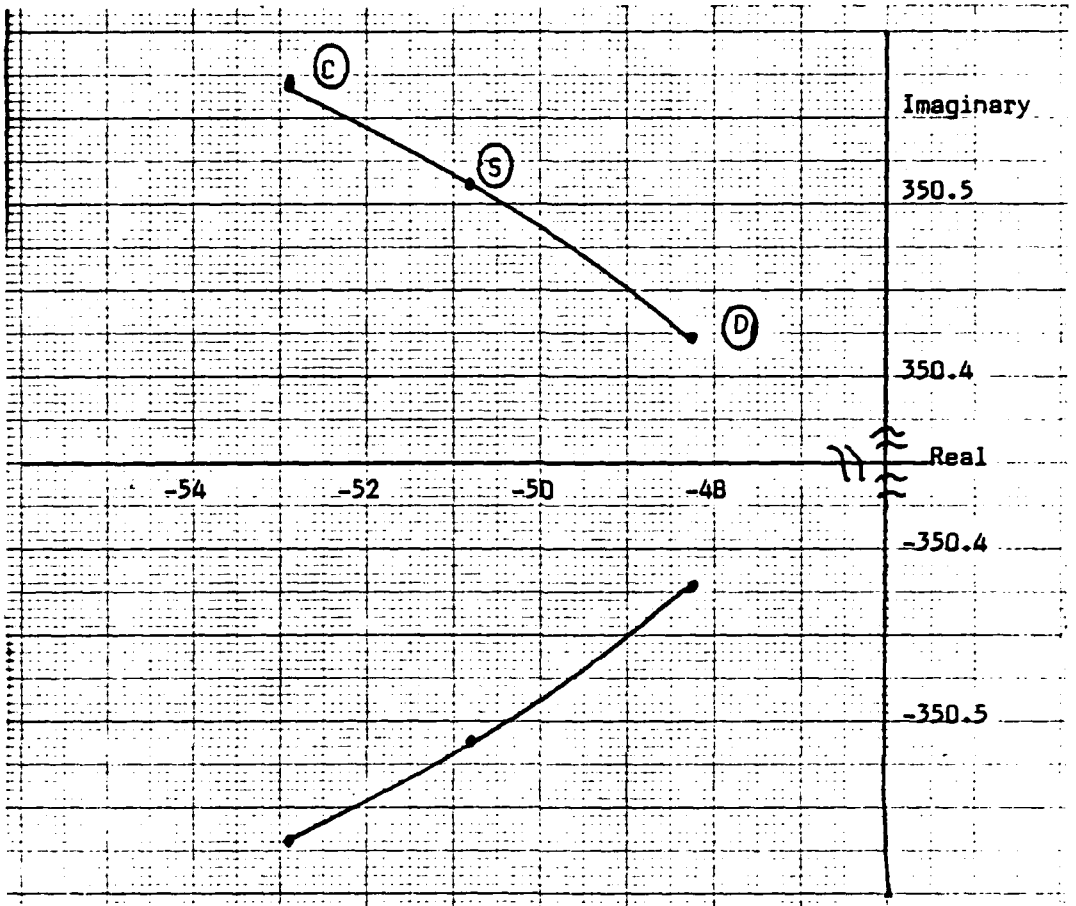

Parameter Values		Seal Strip Dimensions		
P_A = 15.0 psi		(S)	a = .195 in,	P_n = 14.85 psi
P_B = 14.7 psi			b = .195 in	
h_n = .200 in		(D)	a = .196 in,	P_n = 14.79 psi
ℓ = .100 in			b = .194 in	
r = 10.0 in		(C)	a = .194 in,	P_n = 14.91 psi
ω = 579.45 Rad/Sec			b = .196 in	

Figure 4.21d – RWE4S Results – Variable Seal Geometry at High Chamber Pressure, Eigenvalues – Mode 4

volatility of the Circumferential mode suggests its predominance. Therefore, curve shapes and relative distances among points remain practically unchanged.

Mode 1 is stabilized by the seal. The seal also acts to increases its modal frequency.

As most RWE4S simulations reveal, the seal has little perceptible effect on Mode 2. Only speed variations (not a seal parameter) significantly affects Mode 2 (Figures 4.18 and 4.22).

Mode 3 is destabilized and has decreasing modal frequency for $\omega <$ 477 rad/sec (76 rev/sec) due to seal influence. For $\omega >$ 477 rad/sec, Mode 3 is, conversely, stabilized and has increasing modal frequency as a result of seal influence.

Mode 4 is destabilized by the seal. Its modal frequency is increased.

4.D.11.B Rotor Bearing System Influence on Seal Modes

Rotor bearing system influence on seal modes is similar to seal influence on rotor bearing system modes in that RWE4P seal mode curve shapes and relative distances among points are unaffected. The Axial mode is stabilized while the Circumferential mode is destabilized when seal and rotor bearing systems are coupled. Again, because rotor bearing system modes were not isolated, no particular mode can be identified as having a predominant affect on these seal behavior changes.

Another such seal behavior change deals with affects on seal modal frequencies. When seal modes are stable, the rotor bearing system acts to reduce modal frequencies for both seal modes. Such an event

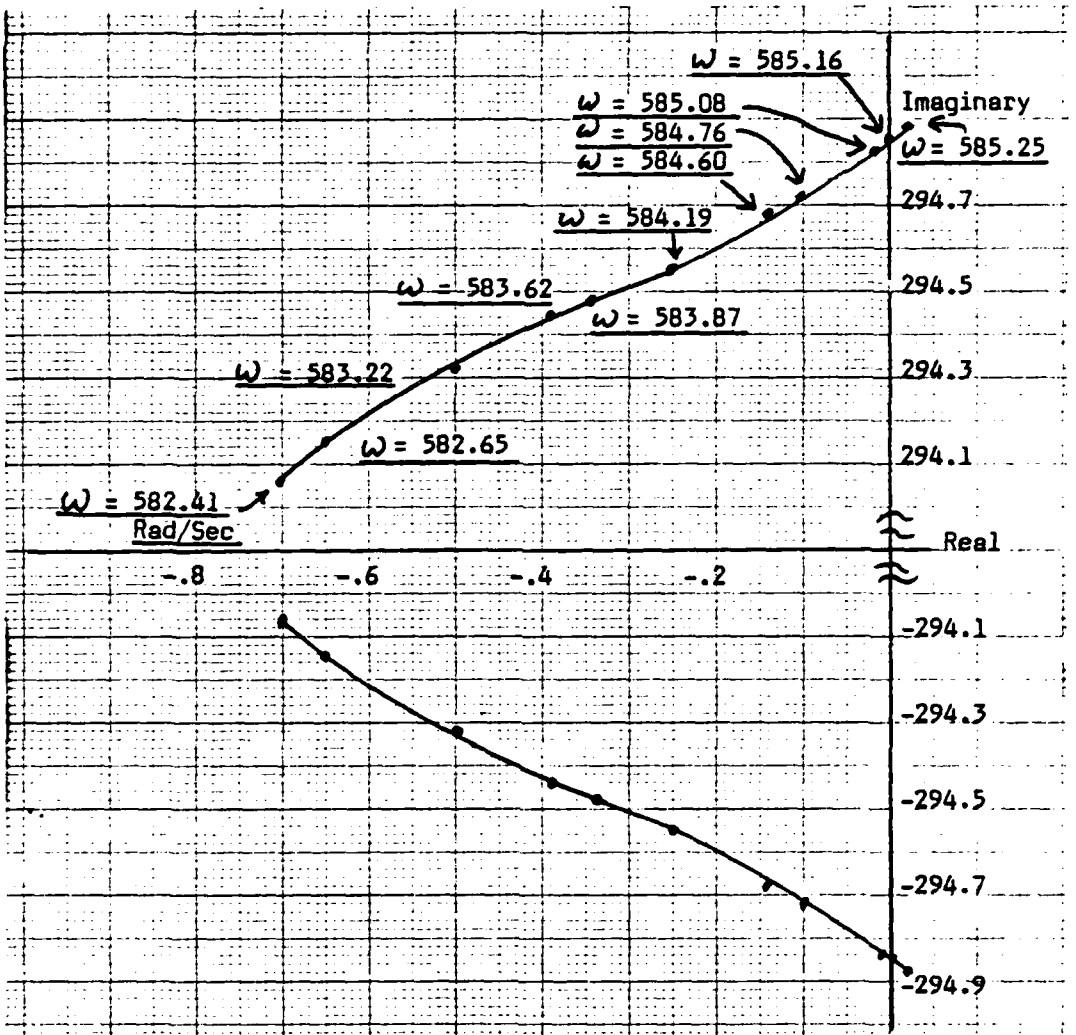

Parameter Values

P_A	=	2.55 psi	ℓ	=	.100 in
P_B	=	1.00 psi	r	=	10.0 in
h_n	=	.200 in			
a	=	.197 in			
b	=	.193 in			

Figure 4.22a – RWE4S Results – Disc Speed Variation at Extreme Seal Divergence – Mode 1

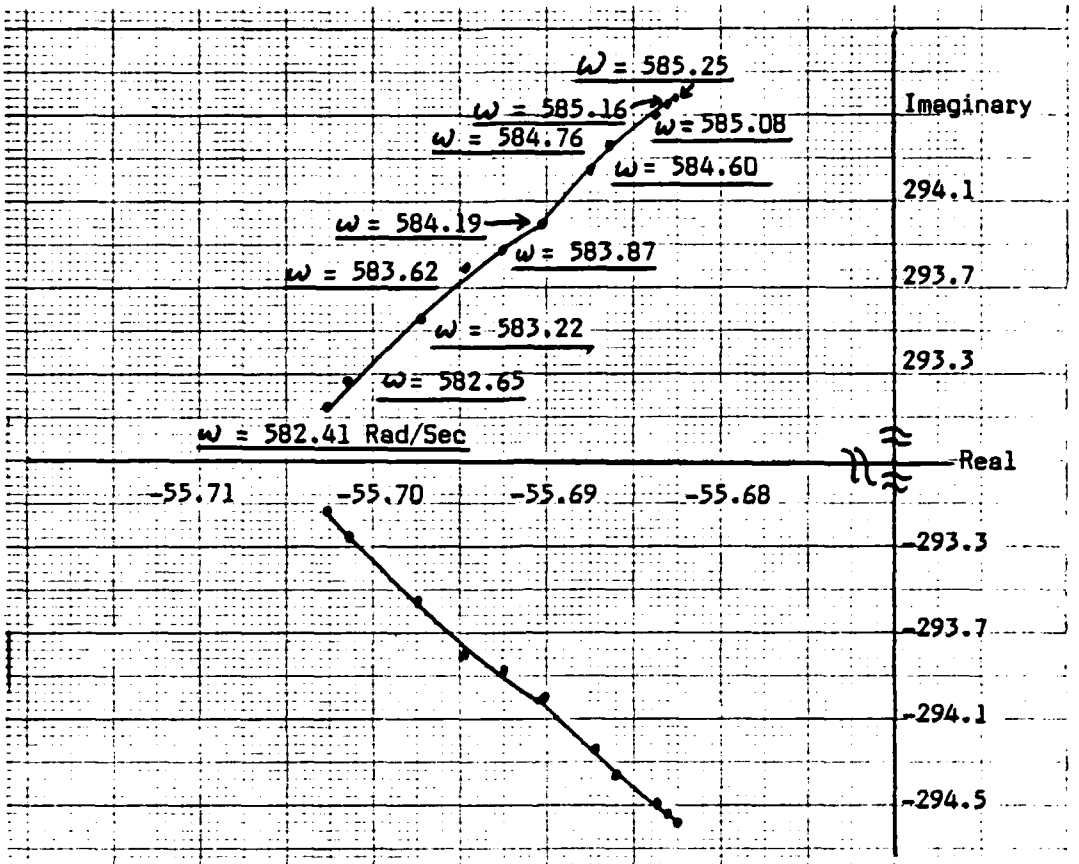

Parameter Values

P_A	=	2.55	psi
P_B	=	1.00	psi
h_n	=	.200	in
a	=	.197	in
b	=	.193	in
ℓ	=	.100	in
r	=	10.0	in

Figure 4.22b – RWE4S Results - Disc Speed Variation at Extreme Seal Divergence - Mode 2

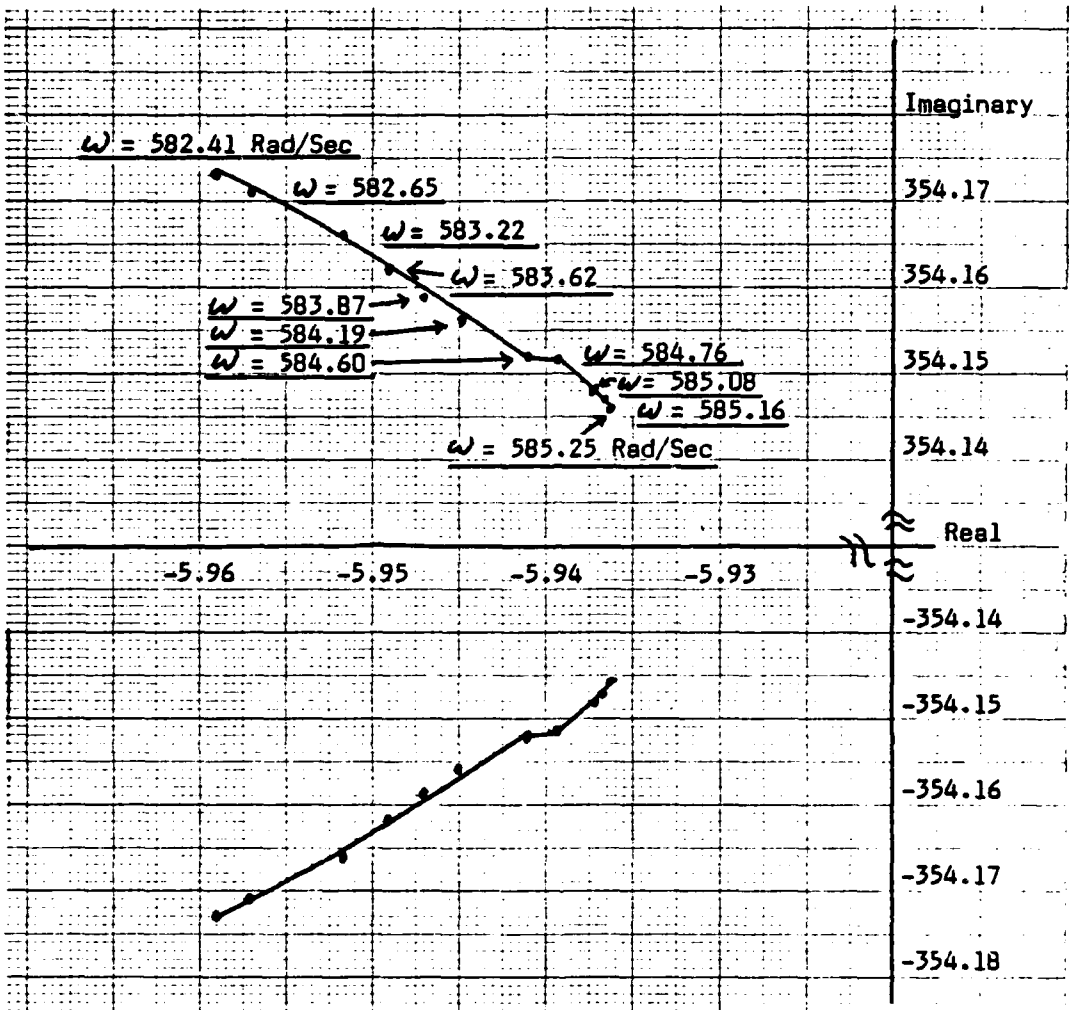

Parameter Values

P_A	= 2.55 psi	ℓ	= .100 in
P_B	= 1.00 psi	r	= 10.0 in
h_n	= .200 in		
a	= .197 in		
b	= .193 in		

Figure 4.22c - RWE4S Results - Disc Speed Variation at Extreme Seal Divergence - Mode 3

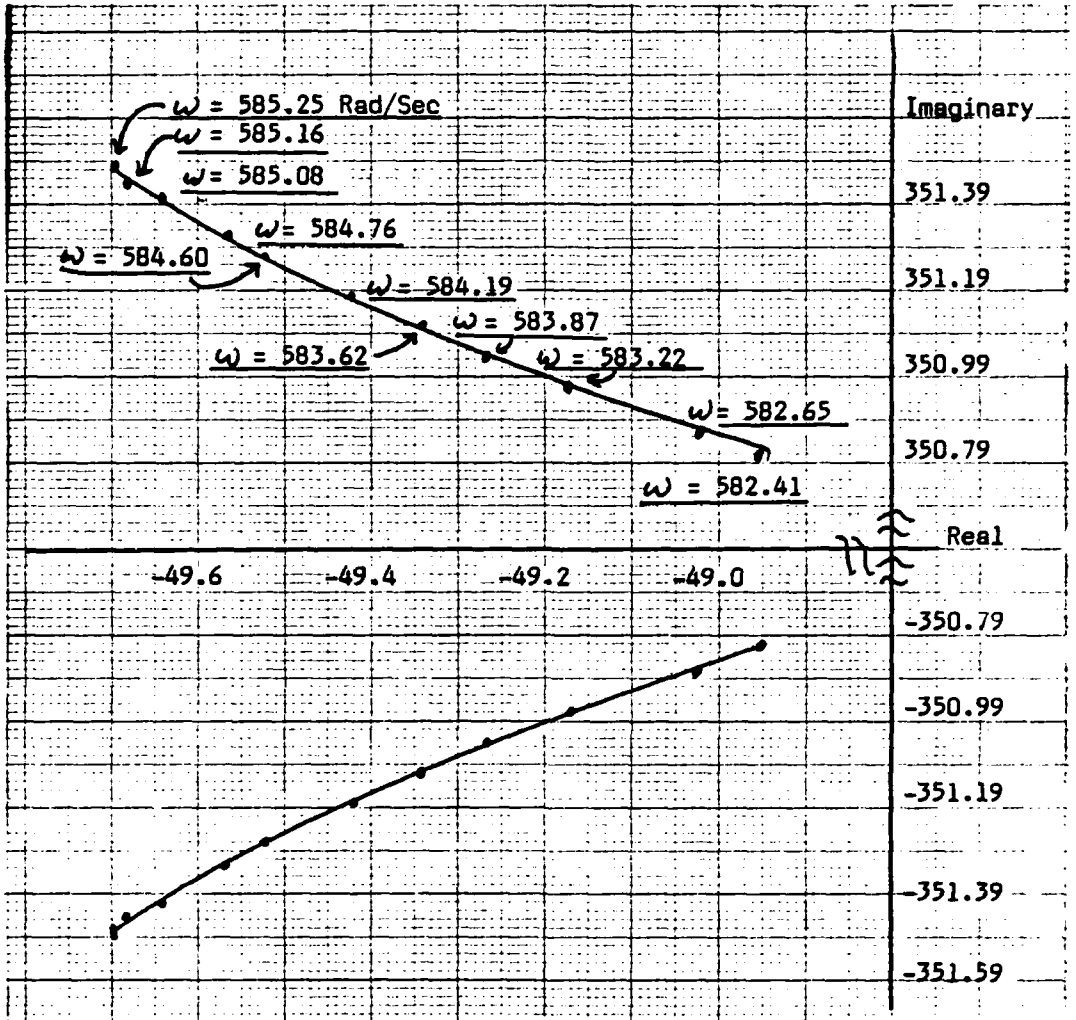

Parameter Values

P_A	=	2.55	psi	ℓ =	.100 in
P_B	=	1.00	psi	r =	10.0 in
h_n	=	.200	in		
a	=	.197	in		
b	=	.193	in		

Figure 4.22d - RWE4y Results - Disc Speed Variation at Extreme Seal Divergence - Mode 4

suggests "frequency transfer" from the seal to the rotor bearing system since seal modal frequencies now add to be less than ω. However, when the seal (Circumferential mode) is unstable, seal modal frequencies add to exceed ω. In this case, Axial (still stable) modal frequency is still reduced, but Circumferential modal frequency increases. Since this result was not encountered during isolated seal and disc simulations this excess frequency must be assumed to have the form of disc whirl. Because both systems are coupled with an unstable seal mode this whirl must be explosive--a dangerous but still realistic condition!

4.E Summary

RW5 and RWE4 rotor bearing system results compare favorably with those of Myrick and Shapiro and Colsher. Such success establishes Chapter 3's analytical rotor bearing system model as both accurate and similar to Myrick's experimental model.

RWE4P results reveal increasing disc radius, disc rotational speed, seal base to disc nominal clearance and seal divergence as having stabilizing influences on seal fluid flow. Conversely, increasing seal strip separation, chamber pressure, and seal convergence destablize fluid flow through the seal. At high pressure and low axial flow rate, both diverging and converging seal geometries stabilize seal modes relative to straight seal geometry. These results, generally, have plausible physical explanations thereby verifying seal modeling accuracy.

Coupled system results also compare favorably with earlier predictions. Because Mode 1 is most susceptible to self excited instability, parameter variation affects on it determine coupled system

stability.

Mode 1 is stabilized by increasing disc radius, seal pressure drop, nominal seal base to disc clearance, and seal divergence. It is destabilized by increasing seal convergence. In the vicinity of nominal parameter values (Table 4.2), increasing seal strip separation stabilizes Mode 1. However, an unstable seal, with further increase in ℓ, soon causes Mode 1 to destabilize. The destabilizing effect of increasing disc speed on Mode 1 is caused primarily by Oil Whip. Straight seal geometry postpones the onset of Oil Whip marginally.

Similarly, diverging seal geometry increases system stability threshold. Although still marginal in degree, this increase satisfies expectations in that, amount of stability threshold increase exceeds that of both straight and convergent seals. This marginal increase cannot be considered within range of modeling error, indicated in 4.B.2, because RWE4 and RWE4S both contain the same rotor bearing system programming. Additionally, by increasing stability threshold the least relative to seal absence, convergent seal geometry results futher reinforce this prediction of increasing stability threshold with increasing seal divergence. This trend appears to apply also at increased chamber pressure and reduced axial flow rate. Unfortunately, additional data at different combinations of such higher chamber pressure and lower flow rates are needed for verification. Such verification was not accomplished using this model because of an unstable Circumferential seal mode at high chamber pressure.

Chapter 5 CONCLUSIONS

The principle aim of this thesis has been achieved. Rotor bearing system stability has been improved by divergent seal geometry. Although such improvement was marginal (.47%), it should be noted that a specific maximized stability threshold increase was not sought. System adjustment to achieve such a threshold is warranted only when dealing with models directly proportionate with operational steam turbines.

Seal parameter affects on system stability were discovered and presented for possible later use in developing seal design criteria. Such information might be used to optimize stability of both seal and rotor bearing system modes toward the goal of turbine efficiency enhancement.

These specific and notable conclusions were developed:

1) Performances of nonlinear (RW5) and linear (RWE4) analytical rotor bearing system models are similar to that of Myrick's experimental model.

2) Labyrinth seal stability is governed primarily by its Circumferential mode.

3) Straight seal geometry increases rotor bearing system stability.

*4) Divergent seal geometry increases rotor bearing system stability threshold beyond that of straight seal geometry.

5) Convergent seal geometry destabilizes the Myrick rotor bearing system relative to straight and divergent seal geometries.

6) This coupled rotor bearing and labyrinth seal system model is not suited for experimental testing at atmospheric pressure.

APPENDIX A

A.1 Nonlinear Rotor Bearing System Programming

```
      PROGRAM RW5(RW5,OUTPUT,TAPE5=RW5,TAPE6=OUTPUT)
      DIMENSION X(20),F(20),TS(100),X3(100),K(7),X1(100),X2(100)
      COMMON/DR/SKX,SKY,BC,W,PI,SPI,DVR,DVL,CL,BR,PSDR,PER,PEL
     1,ERR,ERL,XS(20),H,DM,BM,FXLS,FYLS,FXRS,FYRS
      DATA X,F,TS,X3,XS/452*0./  $DATA K/7*0/
C     THIS PROGRAM SIMULATES ROTOR BEARING SYSTEM OPERATION USING FINITE
C     DIFFERENCE TIME INTEGRATION
C     H=TIME STEP=1.E-05 SEC
C     DV=DYNAMIC VISCOSITY OF BEARING FLUID=5.E-06LBFSEC/IN2
C     CL=JOURNAL LENGTH=1.063IN
C     W=½(JOURNAL+DISC)WEIGHT
C     BC=RADIAL BEARING CLEARANCE=.003IN
C     BR=JOURNAL RADIUS=1.081IN
C     SKX=X DIRECTION ROTOR SHAFT STIFFNESS=5348.6LBF/IN
C     SKY=Y DIRECTION ROTOR SHAFT STIFFNESS=5348.6LBF/IN
C     DM=DISC MASS=.0875LBFSEC2/IN
C     BM=JOURNAL MASS=.0096LBFSEC2/IN
C     ERI=INITIAL JOURNAL ECCENTRICITY RATIO
C     ERS=STEADY JOURNAL ECCENTRICITY RATIO
C     PEI=INITIAL ATTITUDE ANGLE
C     IH=TIME STEP COUNTER
C     ITP=PRINT COUNTER
C     MT=MAX NUMBER OF TIME STEPS
C     NN=NUMBER OF STATE VARIABLES=12
C     M=NUMBER OF PLOT POINTS
C     NP=PLOTTING OPTION(MINIPLT)
      READ(5,1)H,DV,CL,W,BC,BR,SKX,SKY,DM,BM,ERI,PEI,ERS
      READ(5,2)IH,ITP,MT,NN,M,NP
      PI=3.1415927
      SPI=9.8696044
C     INITIALIZE ECCENTRICITY RATIO
      XS(15)=ERS $ XS(13)=ERS
      DVR=5.DE-06  $DVL=5.DE-D6
      D1=(1.-(XS(15)**2))
      D2=XS(15)/(D1**2)
      D3=((16./SPI)-1.)
      D4=(D3*(XS(15)**2)+1.)
C     CALCULATE JOURNAL ANGULAR VELOCITY
      PSDR=4.*W*(BC**2)*(D1**2)/(PI*DVR*CL*XS(15)*SQRT(D4)*BR)
C     CALCULATE ATTITUDE ANGLE
      XS(16)=ATAN((PI/4.)*SQRT(D1)/XS(15))
C     LEFT BEARING
   21 D1=(1.-(XS(13)**2))
      D2=XS(13)/(D1**2)
      D3=((16./SPI)-1.)
      D4=(D3*(XS(13)**2)+1.)
      PSDL=4.*W*(BC**2)*(D1**2)/(PI*DVL*CL*XS(13)*SQRT(D4)*BR)
```

```
      XS(14)=ATAN((PI/4.)*SQRT(D1)/XS(13))
      T=0.0
C     STEADY CONDITIONS
      XS(3)=XS(13)*BC*SIN(XS(14))
      XS(4)=-XS(13)*BC*COS(XS(14))
      XS(5)=XS(3)
      XS(6)=XS(4)
      XS(1)=XS(3)
      XS(2)=XS(4)
C     STEADY BEARING FILM FORCES
      FXLS=W*SIN(XS(14))
      FYLS=W*COS(XS(14))
      FXRS=W*SIN(XS(14))
      FYRS=W*COS(XS(14))
      WRITE(6,6)T,H,XS(15),XS(16),PSDR
      WRITE(6,8)XS(13),XS(14),PSDL
C     WRITE(6,7)(XS(I),I=1,NN)
C     INITIAL CONDITIONS
      X(3)=ERI*BC*SIN(PEI)
      X(4)=-ERI*BC*COS(PEI)
      X(5)=X(3)
      X(6)=X(4)
      X(1)=X(3)
      X(2)=X(4)
      X(13)=SQRT((X(3)**2)+(X(4)**2))/BC
      X(15)=SQRT((X(5)**2)+(X(6)**2))/BC
      X(14)=PEI
      X(16)=PEI
      WRITE(6,6)T,H,X(15),X(16),PSDR
      WRITE(6,8)X(13),X(14),PSDL
C     WRITE(6,7)(X(I),I=1,NN)
      KI=0
      DO 10 II=1,MT,ITP
      KI=KI+1
      TS(KI)=T
      X1(KI)=X(1)
      X2(KI)=X(2)
      X3(KI)=X(3)
C     CALCULATE STATE VARIABLE VALUES
      DO 11 JJ=1,ITP,IH
      CALL RK4(F,X,T,NN,H)
   11 CONTINUE
      WRITE(6,6)T,H,X(15),X(16),PSDR
      WRITE(6,8)X(13),X(14),PSDL
C     WRITE(6,7)(X(I),I=1,NN)
   10 CONTINUE
   33 K(1)=1  $  K(3)=NP
      K(6)=10HX1 VS T
C     PLOT STATE VARIABLE VALUES
      CALL MINIPLT(TS,X1,M,K)
           K(6)=10HX2 VS T
      CALL MINIPLT(TS,X2,M,K,)
           K(6)=10HX2 VS X1
```

```
      CALL MINIPLT(X1,X2,M,K)
           K(6)=10HX3 VS T
      CALL MINIPLT(TS,X3,M,K)
    7 FORMAT( E23.6)
    6 FORMAT( /,5X,'T = ',E10.3,5X,'H = ',E15.6,3X,'ERR=',E12.6,3X,
     1'PER=',E12.5,3X,'PSDR=',E12.5)
    8 FORMAT(46X,"ERL=',E12.6,3X,'PEL=',E12.5,3X,'PSDL=',E12.5,/)
    1 FORMAT(E20.7)
    2 FORMAT(I10)
      STOP
      END

      SUBROUTINE DERIV(F,X,T)
      DIMENSION X(20),F(20)
      COMMON/DR/SKX,DKY,BC,W,PI,SPI,DVR,DVL,CL,BR,PSDR,PER,PEL
     1,ERR,ERL,XS(20),H,DM,BM,FXLS,FYLS,FXRS,FYRS
C     ECCENTRICITY AND ATTITUDE ANGLE INCREMENTS
      E=X(13)*BC $ ES=E**2
      F(13)=(X(3)*X(9)+X(4)*X(10))/(X(13)*(BC**2))
      F(14)=-(X(4)*X(9)-X(3)*X(10))/ES
      E=X(15)*BC $ ES=E**2
      F(15)=(X(5)*X(11)+X(6)*X(12))/(X(15)*(BC**2))
      F(16)=-(X(6)*X(11)-X(5)*X(12))/ES
   21 D1=(1.-(X(13)**2))
      D2=X(13)/(D1**2)
      D3=((16./SPI)-1.)
      D4=(D3*(X(13)**2)+1.)
      DO 46 I=13,14
      K I+2
      F(I)=F(I)/PSDL
   46 F(K)=F(K)/PSDR
C     BEARING FORCE CALCULATION
      FEL=-(((1.-2.*F(14))*2.*(X(15)**2)/(D1**2))+(PI*F(13)*
     1(1.+2.*(X(13)**2))/(D1**2.5)))
      FPL=-((2.*F(14)-1.)*PI*X(13)/(2.*(D1**1.5)))
     1-(4.*F(13)*X(13)/(D1**2)))
      FM=DVL*PSDL*BR/(2.*(BC**2))
      FXL=((FEL*SIN(X(14))+FPL*COS(X(14)))*FM)-FXLS
      FYL=((-FEL*COS(X(14))+FPL*SIN(X(14)))*FM)-FYLS
      D1=(1.-(X(15)**2))
      D2=X(15)/(D1**2)
      D3=((16./SPI)-1.)
      D4=(D3*(X(15)**2)+1.)
      FER=-(((1.-2.*F(16))*2.*(X(15)**2)/(D1**2))+(PI*F(15)*
     1(1.+2.*(X(15)**2))/(D1**2.5)))
      FPR=-(((2.*F(16)-1.)*PI*X(15)/(2.*(D1**1.5)))
     1-(4.*F(15)*X(15)/(D1**2)))
      FM=DVR*PSDR*BR/(2.*(BC**2))
      FXR=((FER*SIN(X(16))+FPR*COS(X(16)))*FM)-FXRS
      FYR=((-FER*COS(X(16))+FPR*SIN(X(16)))*FM)-FYRS
      DO 49 I=13,14
      K=I+2
      F(I)=F(I)*PSDL
```

```
 49 F(K)=F(K)*PSDR
    DO 57 I=1,6
 57 X(I)=X(I)-XS(I)
C     STATE VARIABLE INCREMENTS
    F(1)=X(7)
    F(2)=X(8)
    F(3)=X(9)
    F(4)=X(10)
    F(5)=X(11)
    F(6)=X(12)
    F(7)=(-SKX*(X(1)-X(3))-SKX*(X(1)-X(5))/DM
    F(8)=(-(X(2)-X(4))-(X(2)-X(6)))*SKY/DM
    F(9)=(-SKX*(X(3)-X(1))+FXL)/BM
    F(10)=(-SKY*(X(4)-X(2))+FYL)/BM
    F(11)=(-SKX*(X(5)-X(1))+FXR)/BM
    F(12)=(-SKY*(X(2))+FYR)/BM
    DO 58 I=1,6
 58 X(I)=X(I)+XS(I)
    RETURN
    END

    SUBROUTINE RK4(F,Y,X,NN,HH)
C     4TH ORDER RUNGE-KUTTA
    DIMENSION Y(20),F(20)
    DIMENSION SAVEY(20),PHI(20)
    N=NN $ H=HH
    M=0
  1 M=M+1
    CALL DERIV(F,Y,X)
    GO TO (2,3,4,5),M
  2 DO 22 J=1,N
    SAVEY(J)=Y(J)
    PHI(J)=F(J)
 22 Y(J)=Y(J)+.5*F(J)*H
    X=X+.5*H
    GO TO 1
  3 DO 33 J=1,N
    PHI(J)=PHI(J)+2.0*F(J)
 33 Y(J)=SAVEY(J)+.5*H*F(J)
    GO TO 1
  4 DO 44 J=1,N
    PHI(J)=PHI(J)+2.0*F(J)
 44 Y(J)=SAVEY(J)+H*F(J)
    X=X+.5*H
    GO TO 1
  5 DO 55 J=1,N
 55 Y(J)=SAVEY(J)+(PHI(J)+F(J))*H/6.0
    RETURN
    END
```

A.2 Linear Rotor Bearing System Model Programming

```
      PROGRAM RWE4(RWE4,OUTPUT,TAPE5=RWE4,TAPE6=OUTPUT)
      DIMENSION A(40,40),XR(40),XI(40),BRE(40,40),BI(40,40)
C     THIS PROGRAM GENERATES EIGENVALUES AND EIGENVECTORS FOR THE MYRICK
C     ROTOR BEARING SYSTEM
C     SKX=SHAFT STIFFNESS IN X DIRECTION=5348.6 LBF/IN
C     SKY=SHAFT STIFFNESS IN Y DIRECTION=5348.6 LBF/IN
C     BM=JOURNAL MASS=.0096 LBFSEC**2/IN
C     DM=DISC MASS=.0875 LBFSEC**2/IN
C     W = ½(JOURNAL + DISC) WEIGHT=20.625 LBF
C     DVL=BEARING FLUID DYNAMIC VISCOSITY (LBFSEC/IN**2)
C     CL=JOURNAL LENGTH=1.603 IN
C     BR=JOURNAL RADIUS=1.081 IN
C     BC=JOURNAL TO BEARING RADIAL CLEARANCE=.003 IN
      READ(5,11)SKX,SKY,BM,DM,W,CL,BR,BC
      PI=3.1415927
      SPI=9.8696044
      DVL=5.0E-06 $ DVR=5.0E-06
C     SET INITIAL ECCENTRICITY RATIO
      ERR=.075 $ ERL=.075
      PRINT 11,DM,BM
      PRINT 11
   21 D1=(1.-(ERR**2))
      D2=ERR/(D1**2)
      D3=((16./SPI)-1.)
      D4=(D3*(ERR**2)+1.)
C     CALCULATE ANGULAR VELOCITY
      PSDR=-4.*W*(BC**2)*(D1**2)/(PI*DVR*CL*ERR*SQRT(D4)*BR)
      FM=DVR*PSDR*BR/(BC**2)
      FMD=FM/PSDR
      PER=ATAN((PI/4.)*SQRT(D1)/ERR)
C     CALCULATE BEARING COEFFICIENTS
      BKEER=FM*(-2.*D2-(D2*(ERR**2)*4./D1))/BC
      BKEPR=-PI*FM*ERR/(4.*(D1**1.5)*ERR*BC)
      BDEER=-PI*FMD*(1.+2.*(ERR**2))/(2.*(D1**2.5)*BC)
      BDEPR=2.*ERR*D2*FMD/(ERR*BC)
      BKPER=FM*((PI/(4.*(D1**1.5)))+(.75*PI*(ERR**2)/((D1**2.5))))
     1/BC
      BKPPR=-ERR*D2*FM/(ERR*BC)
      BDPER=2.*(D2/BC)*FMD
      BDPPR=-PI*FMD*ERR/(2.*(D1**1.5)*ERR*BC)
      S=SIN(PER)
      C=COS(PER)
C     BEARING COEFFICIENTS IN X-Y FORM
      BKXXR=((BKEER*S+BKEPR*C)*S+(BKPER*S+BKPPR*C)*C)
      BKXYR=((-BKEER*C+BKEPR*S)*S+(-BKPER*C+BKPPR*S)*C)
      BKYXR=(-(BKEER*S+BKEPR*C)*C+(BKPER*S+BKPPR*C)*S)
      BKYYR=(-(-BKEER*C+BKEPR*S)*C+(-BKPER*C+BKPPR*S)*S)
      BDXXR=((BDEER*S+BDEPR*C)*S+(BDPER*S+BDPPR*C)*C)
      BDXYR=((-BDEER*C+BDEPR*S)*S+(-BDPER*C+BDPPR*S)*C)
      BDYXR=(-(BDEER*S+BDEPR*C)*C+(BDPER*S+BDPPR*C)*S)
      BDYYR=(-(-BDEER*C+BDEPR*S)*C+(-BDPER*C+BDPPR*S)*S)
```

```
      NC=0 $ N=12
C     INITIALIZE A MATRIX
      DO 26 I=1,N
      DO 27 J=1,N
   27 A(I,J)=0.0
   26 CONTINUE
      DO 3 I=1,6
      KI=I+6
      A(I,KI)=1.
    3 CONTINUE
C     LOAD A MATRIX
      A(7,1)=-(SKX*2.)/DM
      A(7,3)=SKX/DM
      A(7,5)=SKX/DM
      A(8,2)=-(SKY*2.)/DM
      A(8,4)=SKY/DM
      A(8,6)=SKY/DM
      A(9,1)=SKX/BM
      A(9,3)=-(SKX+BKXXR)/BM
      A(9,4)=-BKXYR/BM
      A(9,9)=-BDXXR/BM
      A(9,10)=-BDXYR/BM
      A(10,2)=SKY/BM
      A(10,3)=-BKYXR/BM
      A(10,4)=-(SKY+BKYYR)/BM
      A(10,9)=-BDXYR/BM
      A(10,10)=-BDYYR/BM
      A(11,1)=SKX/BM
      A(11,5)=-(SKX+BKXXR)/BM
      A(11,6)=-BKXYR/BM
      A(11,11)=-BDXXR/BM
      A(11,12)=-BDXYR/BM
      A(12,2)=SKY/BM
      A(12,5)=-BKYXR/BM
      A(12,6)=-(SKY+BKYYR)/BM
      A(12,11)=-BDYXR/BM
      A(12,12)=-BDYYR/BM
      DO 89 II=1,12
      DO 88 JJ=1,12
   88 A(II,JJ)=-A(II,JJ)
   89 CONTINUE
      J=1
C     CALCULATE EIGENVALUES AND EIGENVECTORS
      CALL QRHMOD(A,N,J,XR,XI,BRE,BI)
      PSDR=-PSDR
      PRINT 2,PSDR,ERR,PER
C     PRINT EIGENVALUES
      PRINT 30,(XR(I),XI(I),I=1,N)
      PRINT 11
      PRINT 11
C     INCREMENT ECCENTRICITY RATIO
      ERR=ERR-.0001
```

```
      IF(ERR.LT..074)GO TO 23
      IF(ERR.GE..25) GO TO 23
      GO TO 21
   23 CONTINUE
C     PRINT EIGENVECTORS
      PRINT 30,((BRE(I,J),BI(I,J),I=1,N),J=1,N)
    2 FORMAT(9X,'PSDR = ',E12.4,3X,"ERR = ',E12.4,3X,'PER = ',E12.4/)
   30 FORMAT(5X,E15.6,5X,E15.6)
   11 FORMAT(E15.6)
    6 FORMAT(10X,7E15.5/)
      STOP
      END
```

A.3 Linear Rotor Bearing System and Labyrinth Seal - Coupled (RWE4S) and Isolated Seal and Disc (RWE4P) Programming

```
      PROGRAM RWE4S(RWE4S,OUTPUT,TAPE5=RWE4S,TAPE6=OUTPUT)
      DIMENSION AM(40,40),XR(40),BRE(40,40),BI(40,40),PC(4,4)
      DATA PC/16*0./
C     THIS PROGRAM GENERATES EIGENVALUES AND EIGENVECTORS FOR A ROTOR
C      BEARING SYSTEM WITH SINGLE LABYRINTH SEAL
C     SKX= X DIRECTION ROTOR ELASTICITY=5348.6 LBF/IN
C     SKY= Y DIRECTION ROTOR ELASTICITY=5348.6 LBF/IN
C     BM = JOURNAL MASS=.0096 LBF*SEC2/IN
C     DM = DISC MASS=.0879 LBF*SEC2/IN
C     W  = ½ WEIGHT OF ROTOR BEARING SYSTEM ROTATING PARTS=20.625 LBF
C     CL = JOURNAL LENGTH=1.000 IN
C     BR = JOURNAL RADIUS=1.081 IN
C     BC = RADIAL BEARING CLEARANCE=.003 IN
C     CLC= LABYRINTH SEAL AXIAL LENGTH
C     WD = LABYRINTH SEAL CIRCUMFERENTIAL LENGTH=PI*RD*2.
C     PSI= UPSTREAM SEAL PRESSURE
C     TI = SEAL TEMPERATURE=560R
C     R  = GAS CONSTANT (AIR)=247104 IN2/SEC2R
C     A  = UPSTREAM SEAL STRIP HEIGHT
C     B  = DOWNSTREAM SEAL STRIP HEIGHT
C     DC = DISC TO SEAL RADIAL CLEARANCE
C     AMNI= INITIAL UPSTREAM MACH# (ASSUMED)
C     CK = SPECIFIC HEAT RATIO
C     CWB= DOWNSTREAM SEAL STRIP DISCHARGE COEFFICIENT
C     PSE= SEAL DISCHARGE PRESSURE
C     DV = SEAL FLUID DYNAMIC VISCOSITY
C     SPI= PI**2
C     ERR,ERL= JOURNAL ECCENTRICITY RATIOS, RIGHT&LEFT JOURNALS
C     RD = DISC RADIUS
C     VK = KINEMATIC VISCOSITY
      READ(5,11)SKX,SKY,BM,DM,W,CL,BR,BC,CLC,WD,PSI,TI,R,A,B
     1,DC,AMNI,CK,RD,CWB,PSE
      DV=2.8E 09
      PI=3.1415927
      SPI=9.8696044
      CK1=(CK-1.)/CK $ CK1R=1./CK1 $ CKR-1./CK
      CK2=(CK+1.)/(2.*(CK-1.))
      CK3=(3.-CK)/(2.*(CK-1.))
      CK4=(CK-1.)/2. $ CK5=(CK+1.)/2. $ CK5R=1./CK5
      CK6=CK2*2. $ CK7=(1.-2.*CK)/CK
      CK8=SQRT(1.+CK4)
      CK9=(1./CK5)**CK1R
      CK10=1./((1.+CK4)**CK2)
      CK11=SQRT((CK/R)*(CK5R**CK6))
C     BEARING FLUID DYNAMIC VISCOSITY
      DVL=5.0E-06 $ DVR=5.0E-06
C     INITIALIZED JOURNAL ECCENTRICITY RATIO (VALUE AS REQUIRED)
      ERR=.076
C     ITERATE SEAL PARAMETERS
      DC 22 IBI=1,10
```

```
C     SEAL ENTRANCE/EXIT AREAS
  21  AB=(DC-B)*WD
      AA=(DC-A)*WD
C     CALCULATE SEAL CHAMBER PRESSURE
      AMNS=AMNI
  24  FMAS=AMNS/((1.+CK4*(AMNS**2))**CK2)
      PNP=1./((1.+CK4*(AMNS**2))**CK1R)
      CWA=-.3179464*PNP+.9123729
      IF(AMNS.LE.0.)AMNS=0.
      IF(AMNS.LE.0.)GO TO 37
      PN=PNP*PSI
      AMN=SQRT((1./CK4)*(((PSI/PN)**CK1)-1.))
      CWB=-.3179464*(PSE/PN)+.9123729
      BMNS=SQRT((1./CK4)*(((PN/PSE)**CK1)-1.))
      IF(BMNS.GE.1)BMNS=1.
      IF(BMNS.GE1.)CWB=.74
      FMBS=BMNS/((1.+CK4*(BMNS**2))**CK2)
      PNN=AA*PSI*FMAS*CWA/(AB*FMBS*CWB)
      IF(BMNS.GE.1.)PNN=PSE/CK9
      IF(PNN.GT.PN)AMNS=AMNS-.00001
      IF(PNN.LT.PN)AMNS=AMNS+.00001
      IF(PNN.LE.(PN+.0005*PN).AND.PNN.GE.(PN-.0005*PN) GO TO 37
      IF(AMN.GE.1.)AMNS=1.
      GO TO 24
  37  IK=1  $ N=16  $ NN=20  $ MM=10  $ NP=4
      PRINT 11,AMN,AMNS,BMNS,PN,PNN
      PRINT 11
      AMNI=AMN
      D1=(1.-(ERR**2))
      D2=ERR/(D1**2)
      D3=((16./SPI)-1.)
      D4=(D3*(ERR**2)+1.)
C     CALCULATE ROTOR ANGULAR VELOCITY
      PSDR=-4.*W*(BC**2)*(D1**2)/(PI*DVR*CL*ERR*SQRT(D4)*BR)
      FM=DVR*PSDR*BR/(BC**2)
      FMD=FM/PSDR
C     CALCULATE JOURNAL ATTITUDE ANGLE
      PER=ATAN((PI/4.)*SQRT(D1)/ERR)
C     CALCULATE BEARING COEFFICIENTS
      BKEER=FM*(-2.*D2-(D2*(ERR**2)*4./D1))/BC
      BKEPR=-PI*FM*ERR/(4.*(D1**1.5)*ERR*BC)
      BDEER=-PI*FMD*(1.+2.*(ERR**2))/(2.*(D1**2.5)*BC)
      BDEPR=2.*ERR*D2*FMD/(ERR*BC)
      BKPER=FM*((PI/(4.*(D1**1.5)))+(.75*PI*(ERR**2)/((D1**2.5))))
     1/BC
      BKPPR=-ERR*D2*FM/(ERR*BC)
      BDPER=2.*(D2/BC)*FMD
      BDPPR=-PI*FMD*ERR/(2.*(D1**1.5)*ERR*BC)
      S=SIN(PER)
      C=COS(PER)
      BKXXR=((BKEER*S+BKEPR*C)*S+(BKPER*S+BKPPR*C)*C)
      BKXYR=((-BKEER*C+BKEPR*S)*S+(-BKPER*C+BKPPR*S)*C)
      BKYXR=( -(BKEER*S+BKEPR*C)*C+(BKPER*S+BKPPR*C)*S)
```

```
      BKYYR=( -(-BKEER*C+BKEPR*S)*C+(-BKPER*C+BKPPR*S)*S)
      BDXXR=((BDEER*S+BDEPR*C)*S+(BDPER*S+BDPPR*C)*C)
      BDXYR=(-BDEER*C+BDEPR*S)*S+(-BDPER*C+BDPPR*S)*C)
      BDYXR=( -(BDEER*S+BDEPR*C)*C+(BDPER*S+BDPPR*C)*S)
      BDYYR=( -(-BDEER*C+BDEPR*S)*C+(-BDPER*C+BDPPR*S)*S)
      ACH=CLC*WD
      ED=ERR*BC
C     ZERO A MATRIX
      DO 26 I=1,N
      DO 27 J=1,N
   27 AM(I,J)=0.0
   26 CONTINUE
C     X1 THRU X6 INITIALIZATION IN AM
      DO 3 I=1,6
      KI=I+6
      AM(I,KI)=1.
    3 CONTINUE
      RD2=RD/2.
      PSDU=-PSDR*RD
      HN=DC
      AA=(HN-A)*WD
      AB=(HN-B)*WD
C     SEAL FRICTION COEFFICIENTS
      UN=(PSDU/2.)
C     REO=REYNOLDS# AT SEAL BASE
      REO=ABS(PN*UN*HN/(2.*R*TI*DV))
      FFEO=-1./4.38
      AFO=.04176
      IF(REO.GT.1.E+05)FFEO=-1./7.4
      IF(REO.GT.1.E+05)AFO=.01423
C     REI=REYNOLDS# AT DISC
      REI=ABS(PN*(PSDU-UN)*HN/(2.*R*TI*DV))
      FFEI=-1./4.48
      AFI=.04176
      IF(REI.GT.1.E+05)FFEI=-1./7.4
      IF(REI.GT.1.E+05)AFI=.01423
      FFNI=-1./FFEI
      FFNO=1./FFEO
C     DISC AND SEAL BASE FRICTION FACTORS
      FFI=(REI**FFEI)*AFI
      FFO=(REO**FFEO)*AFO
      RT=R*TI
C     SEAL AXIAL FLOW COEFFICIENTS
      BK=SQRT(CK/RT)*PSE
C     DISCHARGE COEFFICIENT AT B
      CWBN=-.3179464*(PSE/PN)+.9123729
      CWBK=.3179464*PSE/(PN**2)
C     MACH# .LE.1
      IF((PSE/PN).LE.CK9)CWBN=.74
      IF((PSE/PN).LE.CK9)CWBK=0.
C     MACH# AT B .LE.1
      BMN=SQRT((1./CK4)*(((PN/PSE)**CK1)-1.))
      IF((PSE/PN).LE.CK9)BMN=1.
```

```
      GMB1=(1.+CK4*(BMN**2))
      GMB=SQRT(GMB1)
      FMB=BMN*GMB
      FMBK=((CK4*((BMN**2))+GMB1)/GMB)*(PSE**CK7)/
     1((PN**CKR)*CK*BMN)
C     AXIAL FLOW AT B-COEFFICIENTS
      PMBK=BK*AB*(CWBN*FMBK+FMB*CWBK)
      HMBK=BK*CWBN*FMB*WD
C     DISCHARGE COEFFICIENT AT A
      CWAN=-.3179464*(PN/PSI)+.9123729
      AK=SQRT(CK/(R*TI))*PSI
      CWAK=-.3179464/PSI
      IF((PN/PSI).LE.CK9)CWAN=.74
      IF((PN/PSI).LE.CK9)CWAK=0.
      AMN=SQRT((1./CK4)*(((PSI/PN)**CK1)-1.))
      IF((PN/PSI).LE.CK9)AMN=1.
      GMA1=(1.+CK4*(AMN**2))
      GMA=GMA1**CK2
      FMA=AMN/GMA
      FMAK=-(GMA-(AMN**2)*CK5*(GMA1**CK3))*(PN**CK7)/((GMA1**CK6)
     1*(PSI**CKR)*CK*AMN)
C     AXIAL FLOW AT A-COEFFICIENTS
      PMAK=AK*AA*(CWAN*FMAK+FMA*CWAK)
      HMAK=CWAN*FMA*WD*AK
C     CONTINUITY EQUATION COEFFICIENTS
      C1PT=CLC*HN
      C1P=(PMAK-PMBK)*RT/WD
      C1H=(HMAK-HMBK)*RT/WD
      C1US=-CLC*PN*HN
      C1PS=CLC*HN*UN
      C1HT=-CLC*PN
      C1HS=-CLC*PN*UN
      FFOE=(FFNO+1.)*FFEO
      FFIE=(FFNI+1.)*FFEI
      VK=DV*RT/PN
C     MOMENTUM EQUATION FRICTION TERMS
      FIPK=-(AFI/FFNI)*(REI**FFIE)*((PSDU-UN)**3)*HN*PN*CLC
     1/(4.*DV*(RT**2))
      FOPK=(AFO/FFNO)*(REO**FFOE)*(UN**3)*HN*PN*(CLC+2.*HN)
     1/(4.*DV*(RT**2))
      FIHK=((AFI*UN/FFNI)*(((PSDU-UN)*HN/(2.*VK))**FFIE))
     1*PN*((PSDU-UN)**2)*CLC/(4.*RT*VK)
      FIUK=((AFI*HN/FFNI)*(((PSDU-UN)*HN/(2.*VK))**FFIE))
     1*PN*((PSDU-UN)**2)*CLC/(4.*RT*VK)
      FOHK=((AFO*UN/FFNO)*((UN*HN/(2.*VK))**FFOE))
     1*PN*(UN**2)*(CLC+2.*HN)/(4.*RT*VK)
      FOUK=((AFO*HN/FFNO)*((UN*HN/(2.*VK))**FFOE))
     1*PN*(UN**2)*(CLC+2.*HN)/(4.*RT*VK)
C     MOMENTUM EQUATION COEFFICIENTS
      C2P=(.5*(FFI*((PSDU-UN)**2)*CLC FFO*(UN**2)*(CLC+2)*HN))/RT
     1)+FIPK+FOPK
      C2H=(-FFO*FN*(UN**2)/RT)+FIHK+FOHK
      C2U=(-FFI*PN*(PSDU-UN)*CLC/RT)+(-FFO*PN*UN*(CLC+2.*HN)/RT)+FIUK+
```

```
     1FOUK
      C2PT=-CLC*UN*HN/RT
      C2PS=-CLC*HN*(((UN**2)/RT-1.)
      C2UT=-CLC*PN*HN/RT
      C2US=-CLC*PN*2.*UN*HN/RT
C     C2HT=-CLC*PN*UN/RT
      C2HS=-CLC*PN*(1.+(UN**2)/RT
C     ZERO SEAL MATRIX
      DO 100 IP=1,NP
      DO 101 JP=1,NP
  101 PC(IP,JP)=0
  100 CONTINUE
C     SEAL MATRIX LOADING
      PC(1,1)=C1P/C1PT
      PC(1,2)=C1PS/(RD*C1PT)
      PC(1,4)=C1US/(RD*C1PT)
      PC(2,1)=-C1PS/(RD*C1PT)
      PC(2,2)=C1P/C1PT
      PC(2,3)=-C1US/(RD*C1PT)
      PC(3,1)=-(C2P+(C1P*C2PT/C1PT))/C2UT
      PC(3,2)=-(C2PS+(C1PS*C2PT/C1PT))/(RD*C2UT)
      PC(3,3)=-C2U/C2UT
      PC(3,4)=-(C2US+(C1US*C2PT/C1PT))/(RD*C2UT)
      PC(4,1)=(C2PS+(C1PS*C2PT/C1PT))/(RD*C2UT)
      PC(4,2)=-(C2P+(C1P*C2PT/C1PT))/C2UT
      PC(4,3)=(C2US+(C1US*C2PT/C1PT))/(RD*C2UT)
      PC(4,4)=-C2U/C2UT
C     DISC TO SEAL COUPLING COEFFICIENTS
      CAH=-C1H/C1PT
      CCH=(C1H*C2PT/(C1PT*C2UT))+C2H/C2UT
      CBH=C1HS/(RD*C1PT)
      CDH=-(C2PT*C1HS/(RD*C1PT*C2UT))-(C2HS/(RD*C2UT))
      CAHD=-C1HT/C1PT
      CCHD=(C2PT*C1HT/(C1PT*C2UT))+(C2HT/C2UT)
      KP=13
      KP3=KP+3
C     A MATRIX LOADING WITH SEAL COEFFICIENTS
      DO 50 I=KP,KP3
      DO 51 J=KP,KP3
      KPJ=J-KP+1
      KPI=I-KP+1
   51 AM(I,J)=PC(KPI,KPJ)
   50 CONTINUE
C     SEAL TO DISC COUPLING
      AM(7,14)=PI*RD*CLC/DM
      AM(8,13)=PI*RD*CLC/DM
C     DISC TO SEAL COUPLING
      AM(13,2)=CAH
      AM(15,2)=CCH
      AM(14,2)=CBH
      AM(16,2)=CDH
      AM(13,8)=CAHD
      AM(15,8)=CCHD
```

```
C     A MATRIX LOADING WITH ROTOR BEARING SYSTEM COEFFICIENTS
      AM(7,1)=(-(SKX*2.)/DM)
      AM(7,3)=SKX/DM
      AM(7,5)=SKX/DM
      AM(8,2)=(-(SKY*2.)/DM)
      AM(8,4)=SKY/DM
      AM(8,6)=SKY/DM
      AM(9,1)=SKX/BM
      AM(9,3)=-(SKX+BKXXR)/BM
      AM(9,4)=-BKXYR/BM
      AM(9,9)=-BDXXR/BM
      AM(9,10)=-BDXYR/BM
      AM(10,2)=SKY/BM
      AM(10,3)=-BKYXR/BM
      AM(10,4)=-(SKY+BKYYR)/BM
      AM(10,9)=-BDYXR/BM
      AM(10,10)=-BDYYR/BM
      AM(11,1)=SKX/BM
      AM(11,5)=-(SKX+BKXXR)/BM
      AM(11,6)=-BKXYR/BM
      AM(11,11)=-BDXXR/BM
      AM(11,12)=-BDXYR/BM
      AM(12,2)=SKY/BM
      AM(12,5)=-BKYXR/BM
      AM(12,6)=-(SKY+BKYYR)/BM
      AM(12,11)=-BDYXR/BM
      AM(12,12)=-BDYYR/BM
   73 DO 89 II=1,12
      DO 88 JJ=1,N
   88 AM(II,JJ)=-AM(II,JJ)
   89 CONTINUE
      J=1
C     CALCULATE EIGENVALUES & EIGENVECTORS FOR AM
C     RWE4P ONLY
      CALL QRHMOD(PC,NP,J,XR,XI,BRE,BI)

C     RWE4S ONLY
      CALL QRHMOD(AM,N,J,XR,XI,BRE,BI)
      PSD=-PSDR
      PRINT 11,A,B,PSI,PSE
      PRINT 6,CLC,RD,DC,REI,REO,FFI,FFO
      PRINT 2,PSD,ERR,PER
C     PRINT EIGENVALUES
      PRINT 30,(XR(I),XI(I),I=1,N)
      PRINT 11
C     SEAL PARAMETERS VARIATIONS
      A=A+.0005
      CLC=CLC+.0249
      RD=RD+1.
      PSI=PSI+.1549
      DC=DC+.0802
   22 CONTINUE
C     GO TO 23
```

```
C     SPEED VARIATIONS
      ERR=ERR-.01
      IF(ERR.LT..074)GO TO 23
      IF(ERR.GT..5)GO TO 23
      GO TO 21
   23 CONTINUE
C     PRINT EIGENVECTORS
      PRINT 30,((BRE(I,J),BI(I,J),I=1,N),J=1,N)
    2 FORMAT(9X,'PSDR = ',E12.4,3X,'ERR = ',E12.4,3X,'PER = ',E12.4/)
   30 FORMAT(5X,E15.6,5X,E15.6)
   11 FORMAT(E15.6)
    6 FORMAT(10X,7E15.5/)
      STOP
      END
```

APPENDIX B

B.1 Beaman [13] Bearing Coefficients (Equation 3.25)

$$K_{ee} = \left[\frac{-2\varepsilon}{(1-\varepsilon^2)^2} - \frac{4\varepsilon^3}{(1-\varepsilon^2)^3}\right]_n \tag{B.1}$$

$$K_{e\phi} = \left[\frac{-\pi\varepsilon}{4(1-\varepsilon^2)^{3/2}}\right]_n \tag{B.2}$$

$$K_{\phi e} = \left[\frac{\pi}{4(1-\varepsilon^2)^{3/2}} + \frac{3\pi\varepsilon^2}{4(1-\varepsilon^2)^{5/2}}\right]_n \tag{B.3}$$

$$K_{\phi\phi} = \left[\frac{-\varepsilon^2}{(1-\varepsilon^2)^2}\right]_n \tag{B.4}$$

$$B_{ee} = \left[\frac{-\pi(1+2\varepsilon^2)}{2(1-\varepsilon^2)^{5/2}}\right]_n \tag{B.5}$$

$$B_{e\phi} = \left[\frac{2\varepsilon^2}{(1-\varepsilon^2)^2}\right]_n \tag{B.6}$$

$$B_{\phi e} = \left[\frac{2\varepsilon}{(1-\varepsilon^2)^2}\right]_n \tag{B.7}$$

$$B_{\phi\phi} = \left[\frac{-\pi\varepsilon}{2(1-\varepsilon^2)^{3/2}}\right]_n \tag{B.8}$$

B.2 XY Bearing Coefficients (Equation 3.28)

$$K_{xx} = \left[\left(K_{ee}\sin\phi + \frac{K_{e\phi}}{e}\cos\phi\right)\sin\phi + \left(K_{\phi e}\sin\phi + \frac{K_{\phi\phi}}{e}\cos\phi\right)\cos\phi\right]_n \tag{B.9}$$

$$K_{xy} = \left[\left(-K_{ee}\cos\phi + \frac{K_{e\phi}}{e}\sin\phi\right)\sin\phi + \left(-K_{\phi e}\cos\phi + \frac{K_{\phi\phi}}{e}\sin\phi\right)\cos\phi\right]_n \tag{B.10}$$

$$K_{yx} = \left[-\left(K_{ee}\sin\phi + \frac{K_{e\phi}}{e}\cos\phi\right)\cos\phi + \left(K_{\phi e}\sin\phi + \frac{K_{\phi\phi}}{e}\cos\phi\right)\sin\phi\right]_n \tag{B.11}$$

$$K_{yy} = \left[-\left(-K_{ee}\cos\phi + \frac{K_{e\phi}}{e}\sin\phi \right)\cos\phi + \left(-K_{\phi e}\cos\phi + \frac{K_{\phi\phi}}{e}\sin\phi \right)\sin\phi \right]_n \tag{B.12}$$

$$B_{xx} = \left[\left(B_{ee}\sin\phi + \frac{B_{e\phi}}{e}\cos\phi \right)\sin\phi + \left(B_{\phi e}\sin\phi + \frac{B_{\phi\phi}}{e}\cos\phi \right)\cos\phi \right]_n \tag{B.13}$$

$$B_{xy} = \left[\left(-B_{ee}\cos\phi + \frac{B_{e\phi}}{e}\sin\phi \right)\sin\phi + \left(-B_{\phi e}\cos\phi + \frac{B_{\phi\phi}}{e}\sin\phi \right)\cos\phi \right]_n \tag{B.14}$$

$$B_{yx} = \left[-\left(B_{ee}\sin\phi + \frac{B_{e\phi}}{e}\cos\phi \right)\cos\phi + \left(B_{\phi e}\sin\phi + \frac{B_{\phi\phi}}{e}\cos\phi \right)\sin\phi \right]_n \tag{B.15}$$

$$B_{yy} = \left[-\left(-B_{ee}\cos\phi + \frac{B_{e\phi}}{e}\sin\phi \right)\cos\phi + \left(-B_{\phi e}\cos\phi + \frac{B_{\phi\phi}}{e}\sin\phi \right)\sin\phi \right]_n \tag{B.16}$$

B.3 Incremental Seal Strip Mass Flow Rate Coefficients

From Equation 3.49e:

$$K_{SCWA} = \left[-\frac{.3179464}{P_A} \right] \tag{B.17}$$

From Equation 3.49f:

$$K_{SCWB} = \left[.3179464\left(\frac{P_B}{P_n^2} \right) \right] \tag{B.18}$$

From Equation 3.49g:

$$K_{SSMA} = \frac{\left(1 + \left(\frac{k-1}{2}\right) M_{An}^2\right)^{\frac{(k+1)}{2(k-1)}} - M_{An}^2 \left(\frac{k+1}{2}\right)\left(1 + \left(\frac{k-1}{2}\right) M_{An}^2\right)^{\frac{(3-k)}{2(k-1)}}}{\left(1 + \left(\frac{k-1}{2}\right) M_{An}^2\right)^{(k+1)/(k-1)}} \qquad (B.19)$$

From Equation 3.49h:

$$K_{SSMB} = \left[\frac{(k-1) M_{Bn}^2 + 2\left(1 + \left(\frac{k-1}{2}\right) M_{Bn}^2\right)}{2\left(1 + \left(\frac{k-1}{2}\right) M_{Bn}^2\right)^{1/2}}\right] \qquad (B.20)$$

From Equation 3.49i:

$$K_{SMA} = \left[\frac{-P_n^{\left(\frac{1-2k}{k}\right)} P_A^{\left(\frac{k-1}{k}\right)}}{k M_{An}}\right] \qquad (B.21)$$

From Equation 3.49j:

$$K_{SMB} = \left[\frac{P_B^{\left(\frac{1-2k}{k}\right)}}{P_n^{\left(\frac{1}{k}\right)} k M_{Bn}}\right] \qquad (B.22)$$

where:

$$M_{An} = \left[\left(\frac{2}{k-1}\right)\left\{\left(\frac{P_A}{P_n}\right)^{\left(\frac{k-1}{k}\right)} - 1\right\}\right]^{1/2} \qquad (B.23)$$

and:

$$M_{Bn} = \left[\left(\frac{2}{k-1}\right)\left\{\left(\frac{P_n}{P_B}\right)^{\left(\frac{k-1}{k}\right)} - 1\right\}\right]^{1/2} \qquad (B.24)$$

B.4 Friction Coefficients in Seal Momentum Equation (Equation 3.52)

$$K_{SSiP} = -\frac{K_{fi}}{n_i}\left[\frac{(rw - u_n) h_n}{2\nu_n}\right]^{\left(\frac{-(n_i+1)}{n_i}\right)}\left(\frac{(rw - u_n)^3 h_n P_n \ell}{4\mu (RT)^2}\right) \qquad (B.25)$$

$$K_{sfop} = \frac{K_{fo}}{n_o}\left[\frac{u_n h_n}{2\nu_n}\right]^{-\left(\frac{n_o+1}{n_o}\right)}\left(\frac{u_n^3 h_n P_n (l+2h_n)}{4\mu (RT)^2}\right) \tag{B.26}$$

$$K_{sfih} = \frac{K_{fi}}{n_i}\left[\frac{(rw-u_n)h_n}{2\nu_n}\right]^{-\frac{(n_i+1)}{n_i}}\left(\frac{u_n P_n (rw-u_n)^2 l}{4\nu_n RT}\right) \tag{B.27}$$

$$K_{sfoh} = \frac{K_{fo}}{n_o}\left[\frac{u_n h_n}{2\nu_n}\right]^{-\frac{(n_o+1)}{n_o}}\left(\frac{u_n^3 P_n (l+2h_n)}{4\nu_n RT}\right) \tag{B.28}$$

$$K_{sfiu} = \frac{K_{fi}}{n_i}\left[\frac{(rw-u_n)}{2\nu_n}\right]^{-\frac{(n_i+1)}{n_i}}\left(\frac{h_n P_n (rw-u_n)^2 l}{4\nu_n RT}\right) \tag{B.29}$$

$$K_{sfou} = \frac{K_{fo}}{n_o}\left[\frac{u_n h_n}{2\nu_n}\right]^{-\frac{(n_o+1)}{n_o}}\left(\frac{h_n P_n u_n^2 (l+2h_n)}{4\nu_n RT}\right) \tag{B.30}$$

where:

$$\nu_n = \frac{\mu RT}{P_n} \tag{B.31}$$

BIBLIOGRAPHY

1. Shapiro, W. and Colsher, R., "Rotor Whirl in Turbomachinery: Mechanisms, Analysis, and Solution Approaches" Turbomachinery Developments in Steam and Gas Turbines ASME Winter Annual Meeting, 27 Nov.-2 Dec. 77, pp 89-98

2. Ehrich, F.F., "Self Excited Vibration", Shock and Vibration Handbook, Harris, C.M. and Crede, C.E. (editors) Chapter 5, pp 1-14, 2nd edition, McGraw Hill, NY

3. Pollman, E., Schwardfeger, H. and Termuehlen, H., "Flow Excited Vibrations in High Pressure Turbines" ASME Journal of Engineering for Power, vol. 100, Apr. 78, pp 219-228

4. Myrick, S.T. Jr., "Transient and Steady State Response of a Flexible Rotor: Real Hydrodynamic Bearing Systems", PhD Dissertation, University of Texas at Austin, Aug. 73

5. Shatoff, J., "Using Vibration Analysis to Determine the Dynamic Health of Turbine Generators", Power, vol. 120, No. 5, May 76 pp 23-28

6. Sneck, H.J., "Labyrinth Seal Literature Survey", ASME Journal of Lubrication Technology, Oct. 74, pp 579-582

7. Alford, J.S., "Protecting Turbomachinery from Self Excited Rotor Whirl", Journal of Engineering for Power, Oct. 65, pp 333-344

8. Spurk, J.H. and Keiper, R., "Selbsterregt Schwingungen bei Turbomaschien infolge der Labyrinthströmung", Ingenieur-Archiv, vol. 43, 1974, pp 127-135

9. Wright, D.V., "Air Model Tests of Labyrinth Seal Forces on a Whirling Rotor" Turbomachinery Developments in Steam and Gas Turbines ASME Winter Annual Meeting, 27 Nov.-2 Dec. 77, pp 61-73

10. Cameron, A., Basic Lubrication Theory, Ellis Harwood Limited, 1976

11. Kearton, W.J., "The Flow of Air through Radial Labyrinth Glands", Proceedings of the Institute of Mechanical Engineers, vol. 169, no. 30, 1955, pp 539-550

12. Kostyuk, A.G., "A Theoretical Analysis of the Aerodynamic Forces in the Labyrinth Glands of Turbomachines", Teploenergetika, 1972, 19 (11), pp 39-44

13. Beaman, J.J., "Journal Bearing Forces-Short Bearing", Unpublished, University of Texas at Austin, 1980

14. Crandall, S.H., Karnopp, D.C., Kurtz, E.F. Jr., and Pridmore-Brown, D.C., Dynamics of Mechanical and Electromechanical Systems, McGraw Hill, 1968

15. Egli, A., "The Leakage of Steam through Labyrinth Seals", Trans ASME, vol. 57, 1935, pp 115-122

16. Shapiro, A.H., The Dynamics and Thermodynamics of Compressible Fluid Flow, vol. 1, Ronald Press Co., NY, 1953

17. Saarlas, Maido, Steam and Gas Turbines for Marine Propulsion, Naval Institute Press, Anapolis, MD, 1978

18. Meirovitch, Leonard, Analytical Methods in Vibrations, The MacMillan Company, Collier-MacMillan Limited, London, 1967

19. Shultz, D.G. and Melsa, J.L., State Functions and Linear Control Systems, McGraw-Hill, 1967

VITA

Anthony John Pavelko was born in Patuxent River, Maryland, on February 3, 1953, to Anthony J. Pavelko and Mary E. Pavelko. He completed secondary school at the Archbishop John Carroll High School, Radnor, Pennsylvania, in 1971. He then attended and completed course work leading to the degree of Bachelor of Science in Mechanical Engineering at the Pennsylvania State University in 1975. Since then, he has served as an officer in the U.S. Air Force including time spent in The Graduate School of The University of Texas, beginning in September, 1979.

Permanent Address: 2100 Oakmont Avenue
Havertown, Pennsylvania

This thesis was typed by Joan K. Kellogg.


FILMED
8-8